University of Naples "Federico II"

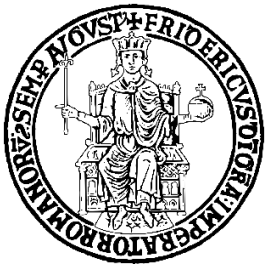

Ph.D. Thesis in

INDUSTRIAL PRODUCT AND PROCESS ENGINEERING

Department of Chemical, Materials and Production Engineering (DICMaPI)

XXXIII cycle

Analysis and control of biomolecular networks by microfluidics

Supervisor:

Prof. Diego di Bernardo

Candidate:

Sara Napolitano

2020/2021

Summary

The process by which the cells respond and adapt to internal and external stimuli, is almost always controlled by a complex network of genes, proteins, small molecules, and their mutual interactions, called signalling network. Over the last years, it has become apparent that quantitative and methodological tools from Biomedical and Control Engineering can be used to understand how these networks work, but also to engineer "synthetic" networks to robustly steer cellular behavior in a prescribed fashion. This possibility will be transformative, enabling myriad applications in biotechnology, chemical industry, health and biomedicine, food, and the environment.

Cybergenetics is a new discipline merging the tools of Synthetic Biology with those of Biomedical and Control Engineering, with the aim of building robust synthetic gene networks to engineer biological processes.

This Thesis is within this research topic, and comprises two different applications, one in yeast cells and one in human cells: (1) closed-loop feedback control to synchronise the cell cycle across a population of yeast cells (*Saccharomyces cerevisiae*); (2) quantitative analysis and model of TFEB nuclear translocation dynamics following mTOR inhibition in human cells (*HeLa*).

In Chapter 1, I introduce the concept of signalling networks, describing how the information coming from extracellular and intracelluar environment is encoded into the dynamical response of the Trascription Factor (TF), i.e. the final effector of the network. Moreover, I present the novel field of Cybergenetics and of the external control paradigm, that is the strategy employed in this Thesis.

In Chapter 2, I describe the microfluidic-based experimental platform used to perform time-lapse experiments on populations of both yeast and mammalian cells. Moreover, I provide details on the image analysis algorithms that I developed.

In Chapter 3, I illustrate how the microfluidics platform, presented in Chapter 2, was used to implement the closed loop control strategies that I designed (the open-loop and the stop&go controllers) to automatically synchronise the cell cycle in a population of yeast cells.

In Chapter 4, I describe a set of experiments performed by means of the microfludics device to probe the dynamics of the nuclear translocation of the transcription factor EB following mTOR inhibition, together with the derivation of a dynamical model and a set of novel hypotheses on the mechanism of action of chemical mTOR inhbitors.

Finally, in Chapter 5, final considerations are drawn on the future research pathways opened up by the results described in this Thesis.

Contents

List of Figures

Chapter 1

Introduction

In this chapter, I will give an overview of the basic concepts and tools explored in this Thesis. Specifically, I will describe the concept of signalling network and how their dynamical response to the stress can encode different information, and the new discipline of cybergenetics, which applies biomedical and control engineering tools to Synthetic Biology.

1.1 Signalling networks

The cell is the minimal unit of life. Despite its simplicity, it has to carry out many processes to maintain cellular homeostasis and to make decisions such as whether to divide, to differentiate, or to die. In each case, the cell responds to external stress and/or stimuli including hormones, neurotransmitters, mechanical stretch and shear, and ion currents. Specifically, receptor proteins sense extracellular and intracellular environment activating a cascade of biochemical modification in downstream proteins, which together form the signalling pathway. Protein receptors can be connected to many different cellular processes, thus combining more signalling pathways into a signalling network. The organization (topology) of the signaling network drives the relationship between inputs and outputs providing the cell with decision-making capabilities.

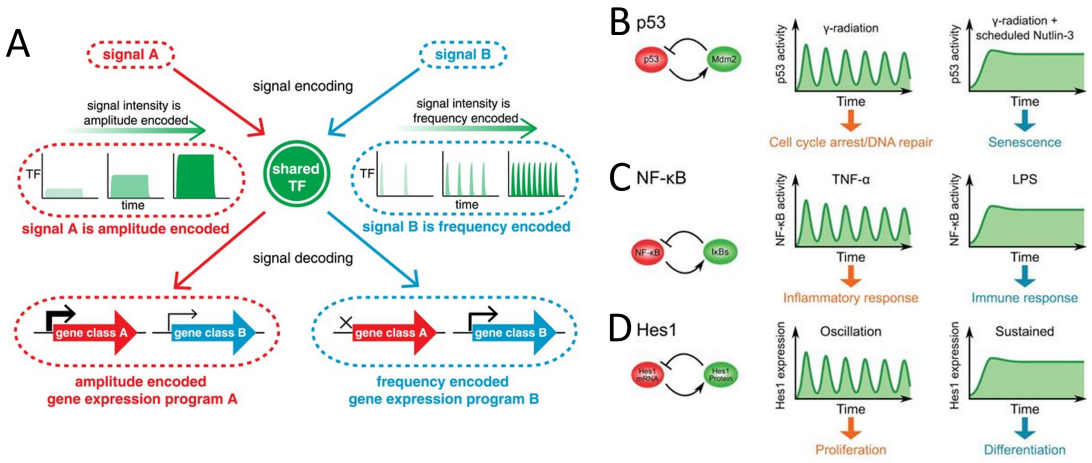

Figure 1.1: **Signals encoding in the dynamics of the transcription factor.** (**A**) Different signals can be encoded in the dynamics of a single Transcription Factor (TF), and, specifically in the type of TF dynamics: a sustained signal (signal A) or an impulse (signal B). Signal intensity is encoded in amplitude for signal A, and in frequency for signal B. From [1]. (**B** - **D**) Three examples of transcription factore whose dynamics decode the information from the protein receptors: p53 (**B**); NF-kB (**C**); and Hes1 (**D**) From [2].

Final effectors of signalling pathways are the Transcription Factors (TFs), which control the expression of thousands of genes steering the cell fate. It is quite common for different receptors of a signalling pathway to converge into the same "master" TF, which can, in response, give rise to different outputs depending on the activating signal, thus regulating the expression of different subsets of target genes [1, 3–5]. Moreover, a single TF can be the final effector of more signalling pathways. This means that genes downstream of a TF can decode the information provided by the TF itself. Recent studies revealed that this encoding activity is carried out by TF dynamical response to the stimulus. Specifically, as shown in Fig. 1.1A, TF can encode the information in the amplitude of the activation or its frequency [1]. Indeed the TF activity over time can be regulated in terms of quasi-periodic oscillations in its concentration and/or nuclear localisation following activation by the stimulus [4–7]. These oscillations are often due to delayed negative feedback loops [5].

These dynamics, however, are difficult to observe and study because of the strong

cell-to-cell variability in TFs activation following the stimulus. To overcome this drawback, cells have been treated with two types of stimuli: (i) a constant input, also known as step input, which gives rise to a transient and unsynchronised TF response [8,9]; and (ii) a periodic stimulus, i.e. a periodic input, whose period is chosen very close to the natural period of the signalling pathway. This second strategy can synchronise the TF response, generating a phase-locked response, thus reducing the cell-to-cell variability [10–13].

Three of the most representative examples of how different dynamics can induce different responses are the transcription factor p53, NF-kB, and Hes1. They all exhibit quasi-periodic oscillations in their activity either in terms of nuclear localisation (p53 and NF-kB) or expression levels (Hes1).

The transcription factor p53 (Fig. 1.1B) is a tumor suppressor that responds to multiple stresses, such as DNA damage, regulating the expression of many genes which final goal is DNA repair and cell cycle arrest, cell senescence or apoptosis [6, 8]. In response to DNA damage, p53 periodically translocates into the nucleus, exhibiting periodic oscillations with a fixed period and amplitude. The number of these oscillations is stimulus-dependent [5] and changes the outcome of the signalling pathway: the presence of oscillations causes resumption of proliferation and permanent arrest if such oscillations persist; while non-oscillatory sustained activation of p53 is associated with permanent cell cycle arrest [8].

The Nuclear Factor kB (NF-kB) (Fig. 1.1C) is a protein complex with transcription factor activity playing a major role in modulating the immune response to infection. NF-κB nuclear oscillations drive the expression of three classes of genes: early, intermediate and late. The expression levels of early genes are relatively constant even with small stimuli, whereas late genes are only expressed at the strongest stimuli, suggesting that the initial NF-κB localization burst is sufficient to express the early genes. Finally, the expression levels of the intermediate and late genes build up slowly after persistent NF-κB oscillations [14].

The Hairy and Enhancer of Split 1 (Hes1) (Fig. 1.1D) is a transcription factor regulated via the Notch signalling pathway and whose exact function is still unclear. Hes1 expression is characterised by periodic oscillation whose period is between 2 or 3 h, mediated by a feedback regulation due to repression activity of Hes1 on its own expression [15–17]. It has been recently demonstrated that these oscillations play a key role in fate-determination steps during embryonic differentiation [18].

1.2 Cybergenetics: where Control Engineering meets Synthetic Biology

For a long time, biology was seen as something to observe and study. Then, the innovative discoveries in genetic engineering have revolutionised biological sciences, biomedicine, and biotechnology, facilitating the manipulation of individual genes. In this context, a new field emerged, *Synthetic Biology*, with the aim of constructing new biological circuits able to control cellular behaviour. Synthetic biology has broad applications in medical, biofuel, chemicals, and biomaterials fields as well as provides a revolutionary tool in the understanding of basic life sciences. However, the noisy nature of biomolecular interactions renders a fine regulation of such circuits necessary for their correct operation [19].

On the other hand, *Control Engineering* aims at improving the stability, robustness, and performance of physical systems in several applications, including mechanical devices, electrical/power networks, space and air systems, and chemical processes [20].

The merging of principles of control engineering with synthetic biology is known as *CyberGenetics* [19]. In this new exciting field, synthetic biology tools are used to replicate the classical feedback scheme of the control theory, building biomolecular controllers (Fig. 1.2). The benefits of this approach are countless. For example, it improves experimental reproducibility thanks to the self-adaptability of the negative

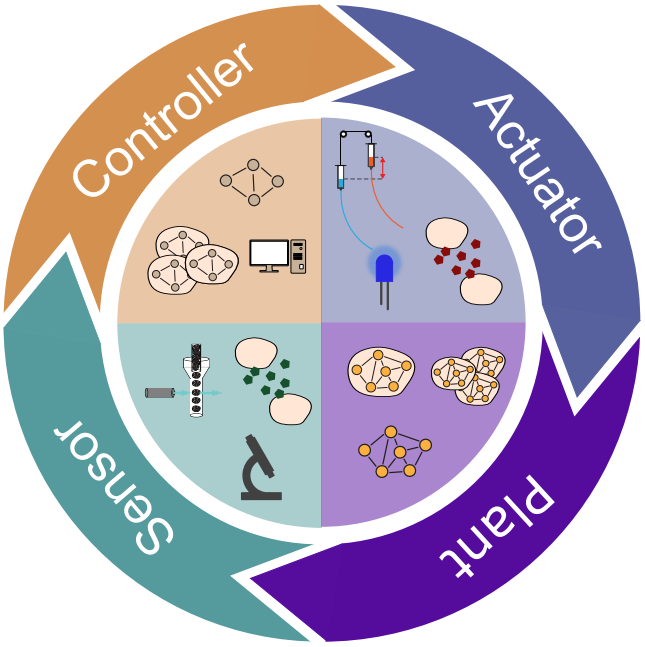

Figure 1.2: **Cybergenetics: the meeting between control engineering and synthetic biology.** Synthetic biology has developed different ways to replicate the classical modules used by control engineering.

feedback system to environmental changes and the reduction of noisy effects [21].

According to control theory, the classical feedback scheme can be summarised in two main components, shown in Fig. 1.3A: the *plant*, i.e. the process to be controlled, and the *controller* that works with a sense and react paradigm to drive the plant to behave as desired. Here, the controller receives measures of the plant output and computes the input to deliver to the plant to decrease the difference between the measured value of the output and its desired value (i.e. the control error). To replicate this scheme to control biological processes, three different strategies have been proposed [19, 21, 22]: (i) the external control, where the controller is implemented as a software in a computer (Fig. 1.3B); (ii) the embedded control, where the controller is implemented as a genetic circuit in the same cell of the process to control (Fig. 1.3C); (iii) the multicellular control, where the controller is realised in a cell population that controls the process carried out by a different cell population (Fig. 1.3D).

Among these three strategies, the external control, described with more details in

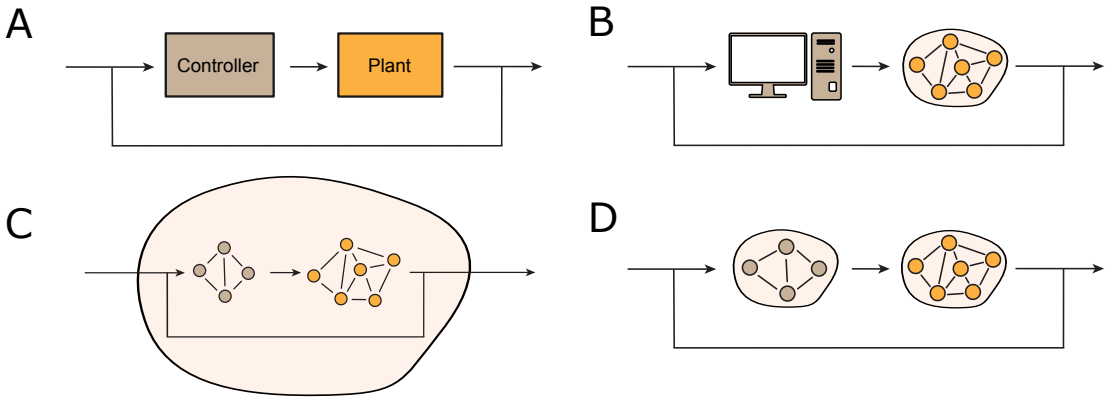

Figure 1.3: **The negative feedback paradigm translated into cybergenetics.** (**A**) General feedback control architecture where a controller steers the behaviour of a plant adapting the control input to the plant response. (**B**) External control: the control algorithm is implemented as a computer software and interfaced with cells by dedicated actuators. (**C**) Multicellular control: two cell populations coexist in a consortium, with one population embedded with a controller driving the second population harbouring the biological process to be controlled. (**D**) Embedded control: both the controller and the process to be controlled are present within the same cell.

Section 1.2.1, is the simplest to implement because it does not require the construction of new genetic circuits. For this reason, it is also adopted as a test-bed for the other two strategies. Indeed, it requires just interfacing the biological process with a computer via a set of sensors to measure the actual output of the plant and actuators to deliver the control input to the cells.

For embedded controllers, systematically reviewed in [19, 21, 23], both the process and the controller are present within the cell. In this case, the controller is implemented by a synthetic gene regulatory network (GRN) encoding new functions into living cells. Despite the great advantage of having a cell population whose bioproduction is robust to perturbations, the embedded control has two main drawbacks: the extra metabolic burden, and the lack of modularity. Indeed, cells have limited resources, and, therefore, producing the needed to implement the controller can be hindered. Moreover, the absence of modularity means that any change of the controller requires a complete redesign of the embedded GRN.

Despite a growing number of researchers are working to solve the extra burden [24–

26] and the modularity [27, 28] problems, one of the most promising approach to overcome the limitations of embedded control, while at the same time preserving its advantages, is the multicellular control strategy [19]. Here, the controller and the process to be controlled reside in two distinct cell populations that co-exist in the same cellular consortium. The interactions between the process and controller happen through diffusible molecules [29–32], the so-called quorum sensing mechanism [33]. A critical requirement for a correct operation of a multicellular control architecture is keeping the ratio between the two populations within an acceptable range, otherwise a population may surpass the other. If the target population becomes predominant, the control population will be no longer able to regulate it. If the contrary happens, the controller population will have nothing to modulate.

1.2.1 External control strategies to steer biological processes

The *External* or, *in silico*, control strategy consists of interfacing the biological process to be regulated with a computer in which the control algorithm is implemented as computer software (Fig. 1.3B). Over the last years, different platforms, summarised in Fig. 1.4, have been developed to implement external control [34–39]. In each of these cases, the regulation of a biological process, i.e. the plant, needs four basic modules (Fig. 1.4A), which can be assembled into different configurations.

In a cybergenetic system, cells can grow either in a microfluidic device or in a turbidostat (Fig. 1.4B). Both of them are useful to grow cells in an optimal environment in which temperature, pH, CO_2, and many others growth conditions are fine regulated. While yeast and bacteria cells can grow both in microfluidic devices [34, 37–39] and turbidostats [36], mammalian cells are, until now, cultured only in microfluidic devices because of their higher sensitivity to growth conditions and the need for most cell types to grow attached to a solid surface [35, 40].

A feedback-based control system needs to measure the actual output of the plant (y)

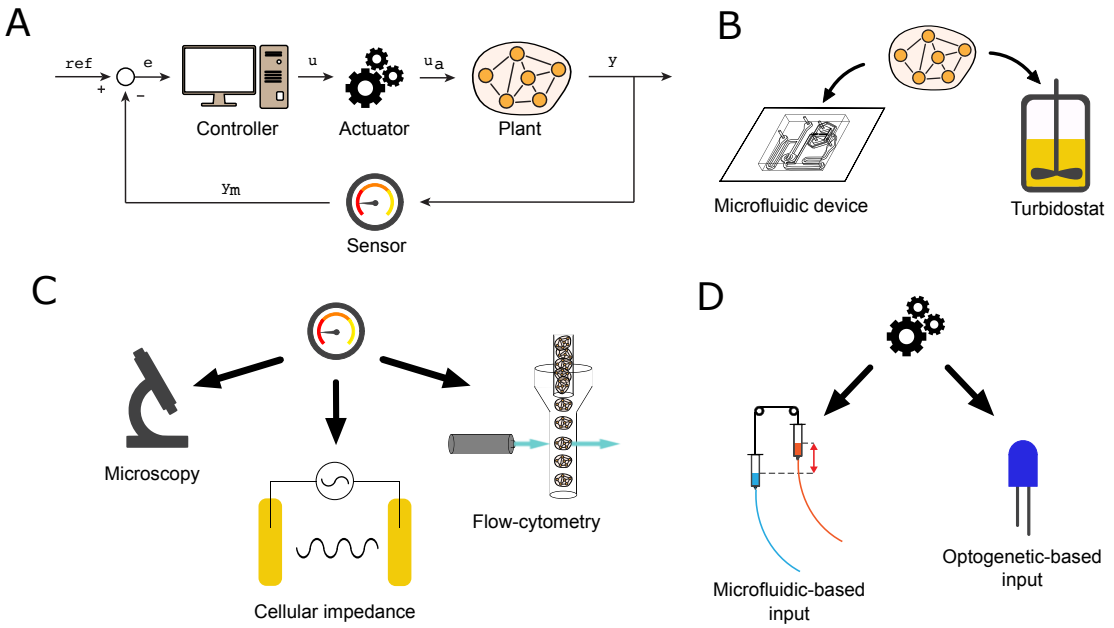

Figure 1.4: **Experimental platforms for the application of external control.** (**A**) External control platforms consist of four basic modules: (i) the controller, i.e. a computer algorithm; (ii) cells, i.e. the plant; (iii) the sensor to measure the output, and (iv) the actuation system to provide the control input. Each module can be implemented in a variety of ways. (**B**) Cells need a suitable environment to grow. Either microfluidic devices or turbidostats have been used for long term culture of cells in control applications. (**C**) A variety sensors can be used to measure the system output, which is usually proportional to a fluorescent reporter protein. To this end, microscopy and flow-cytometers are used in combination respectively with a microfluidic device or turbidostats. Other cellular features can be used as system output. For example, microelectrods can be used to measure the cellular impedance, considered as proxy of colony growth. (**D**) Actuation includes changing the concentration of a specific inducer (microfluidic-based input) or exposing the cells to light of a specific wavelength (optogenetic-based input). While the first strategy can be used only on cells cultured in a microfluidic device, light can be used both in the case of microfluidics and turbidostats.

to compute the input to deliver to the plant. In the case of a cybergenetic system, the output of the process to be controlled is usually proportional to a fluorescent protein. To measure this kind of output, therefore, cells in a microfluidic device are usually imaged through an epifluorescence microscope [34–39] while the fluorescent protein emitted by a suspension of cells in turbidostat is measured employing a flow-cytometer [36] (Fig. 1.4C). Recently, in place of a fluorescent protein, cellular impedance was used as a proxy of bacterial colony growth [41]. Indeed, during bacterial growth, charged ions

are naturally released because of metabolic processes making the surrounding medium more conductive. Thus, Din *et al.* [41] had cells grown in turbidostat or a customised microfluidic device in contact with microelectrodes to measure cellular impedance.

Another fundamental part of an *in silico* control system is the actuator that delivers the input (u_a) to the cells. Major actuation methods are syringes and pumps to change the concentration of a chemical or metabolite (microfluidic-based input) [34, 35, 37], or lasers or LEDs to expose cells, previously engineered, to the light of specific wavelengths (optogenetic-based input) [36, 38, 39] (Fig. 1.4D). Microfluidic-based input has the advantage of being simple to implement and that the control input can be biologically relevant (a drug, a hormone, etc.). Moreover, each cell will receive the same control input. On the other hand, although the requirement of extensive engineering of the cell, optogenetic-based input offers precise spatio-temporal modulation of protein function with low-to-no toxicity. Indeed, making use of a Digital Micromirror Device (DMD) projector, consisting of millions of independently controlled MEMS mirrors, it is possible to deliver a different input to each cell [39]. In bioreactors, i.e. turbidostats, an optogenetic input may be the only option as changing the concentration of a chemical input may be very challenging and expensive. Therefore, a growing effort in developing robust optogenetics circuits is ongoing and it has been systematically reviewed in [42, 43].

Finally, the last module of an external control system is the controller implemented in a computer. Over the years, both model-free and model-based control algorithms have been designed and implemented. Simple model-free controllers, e.g. relay [40, 44, 45] and Proportional Integral Derivative (PID) controllers [34, 36, 37, 44, 46], were the first attempts of strategies used to regulate gene expression in bacteria, yeast, and mammalian cells. More complex controllers include model-based controllers, such as Model Predictive Control (MPC) [34, 36, 38–40, 46–48] and the Zero Average Dynamics (ZAD) control scheme [34], achieving satisfactory results despite the simplicity of the models used. Recently, a reinforcement learning control strategy was proposed,

even if only in simulation, to control microbial co-cultures in bioreactors, optimizing bioproduction despite the resource competition between the two species [49].

The first applications of external control were aimed to demonstrate the feasibility of controlling GRNs. Specifically, the expression of a fluorescent protein was controlled by using different inputs, such as osmotic pressure [47] and carbon source [34, 50] in yeast cells or inducible drugs in different types of mammalian cells, including mouse embryonic stem cells [35, 40, 45], and, obviously, light [36]. Then, the same platforms were used to steer signaling pathways, i.e. endogenous networks, in mammalian cells, such as the Erk [51] and mTORC1 [40] pathways. More recently, these strategies were applied to steer more and more complex cellular mechanisms. For example, Lugagne *et al.* [37] applied the external control platform with an open-loop control strategy to a bistable nonlinear genetic circuit, the toggle-switch in bacterial cells, that exhibits two stable states resulting from two proteins mutually repressing their production. By applying a periodic input in which the two input molecules alternate each other, they were able to maintain the majority of cells close to the unstable equilibrium point. Then, in [46,52], the authors proposed and tested in simulation different control strategies able to keep the toggle switch in its unstable equilibrium point, demonstrating the feasibility of maintaining cells in an undifferentiated state. In a similar fashion, in [53], the authors proposed for the first time a reinforcement learning approach, a model-free strategy very robust to biological stochasticity. With cell-in-the-loop, instead, Perkins *et al.* [54] were able to induce cellular patterning emulating cell-to-cell communication signals calculated *in silico* from real-time measurements using light.

Notwithstanding, the complexity of the platform needed for the application of external control and the necessity to measure in real-time the system output, limit the application of external control in the clinics. Indeed external control is most used in biotechnological applications, i.e. bioproduct production, or in research to study and better understand unknown biological and pathological mechanisms. For example, Harrigan *et al.* [48] applied closed-loop optogenetic compensation (CLOC) to investigate

the dynamics of endogenous cellular feedback loops, replacing them with their synthetic light-inducible version and closing the loop externally with an MPC. With this tool, the authors elucidated the time scales of the yeast pheromone response MAPK pathway, which cannot be fully interrogated by compensation with static genetic alleles. Similarly, a microfluidics-based feedback platform was used to control the α-synuclein in yeast cells to elucidate the mechanisms of the formation of α-synuclein aggregates demonstrating that the mutant form, responsible for Parkinson's Disease, forms inclusions at a concentration that is half of that of the wildtype form [55].

Chapter 2

An automated microfludics platform for yeast and mammalian cells

In this Chapter, I will present the microfluidic-based experimental platform that I used in this Thesis (Fig. 2.1). This platform, already used for controlling gene expression in living cells [34, 35, 40, 50, 56], is based on the closed-loop feedback paradigm performing the following steps: (i) cell culture in a microfluidic device that allows the fine control of the micro-environment; (ii) acquisition of phase-contrast and epifluorescence images in real-time by a microscope; (iii) computer implementation of a controller algorithm that evaluates the system output (through a custom image analysis algorithm) and computes the correct input to deliver to the cells; and (iv) an actuation system comprising a pair of syringes delivering the input to the cells.

2.1 Microfluidic device

Microfluidics allows to grow cells and to precisely change their environmental conditions in real-time. Indeed, microfluidic devices allow to isolate cells from external disturbances as well as to continuously refresh or change their growing medium to avoid the depletion of nutrients due to cell consumption. At the same time, a microfluidic

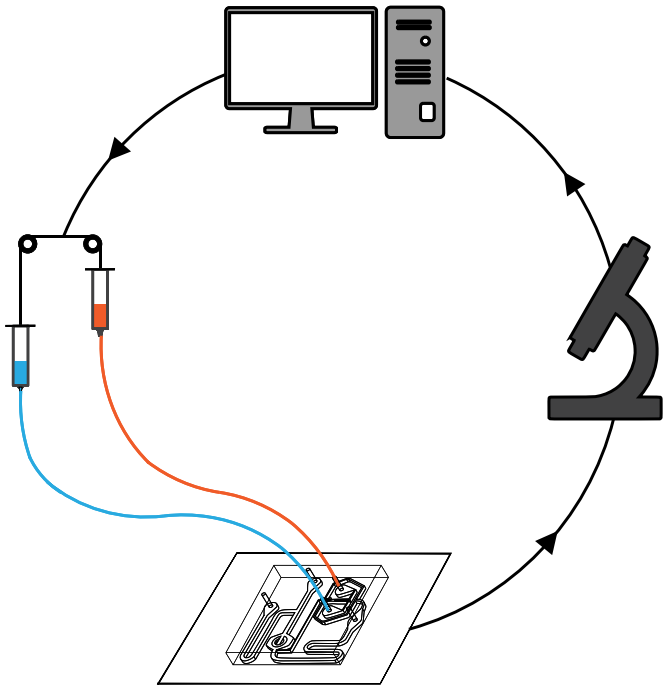

Figure 2.1: **Microfluidic-based experimental platform.** Cells loaded in a microfluidic device were imaged through an epifluorescence microscope. The images are analysed with a custom image analysis algorithm implemented in a computer that controls also the actuation system, i.e. a couple of syringes filled with the inducer or normal medium.

device can be mounted on standard microscope slides allowing the imaging through a microscope to evaluate the effects of the input provided to the system. These devices are, essentially, chips (mostly in PDMS), where fluid dynamics at the microliter scale are exploited. The principle is to have an area where the cells are forced to be in (cell trap), together with a series of channels to provide one or more compounds to the trap to regulate cells environment or to collect cells and fluids wastes.

2.1.1 Microfluidic device for yeast cells culture

For the experiments performed with yeast cells, I chose to use the MFD0005a device, designed by the Biodynamics Laboratory of Prof. Jeff Hasty (UCSD) [57] and shown in Fig. 2.2A. Briefly, this device consists of a micro-chamber (height: 3.5 μm) which "traps" yeast cells, that can only grow in a mono-layer, thus allowing to have cells always in focus and thus enabling automated image analysis. A fluidic mixer network,

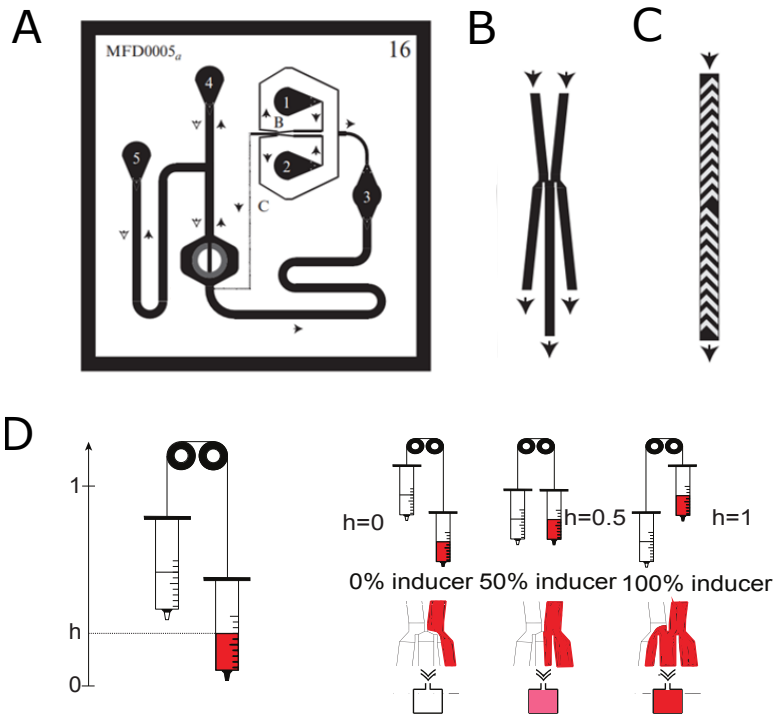

Figure 2.2: **Microfluidic device for yeast cells culture.** (**A**) Overview of the MFD0005a chip's architecture. (**B**) Dial–A–Wave junction. (**C**) Staggered herringbone mixer (SHM). (**D**) DAW working principle. Adapted from [40, 57].

named the Dial-a-Wave (DAW) (Fig. 2.2B), to deliver any desired waveform of biochemical inducer for dynamic stimulation of cells inside the culture chambers. Specifically, fluids from ports 1 and 2 (inlets) arrive at the DAW that precisely combines the two incoming fluid streams in any desired ratio determined by modulating the difference in hydrostatic pressures at the two inlets, as schematised in Fig. 2.2D, increasing the pressure at one inlet while decreasing it at the other by the same amount so that the flow rate out of the junction remains constant. Because of the laminar profile of the fluids into a microfluidic device, the fluid leaving the junction has to be mixed to deliver a uniform inducer concentration in the whole cell chamber. To this end, a staggered herringbone mixer (SHM) (Fig. 2.2C) [58] is present downstream of the DAW.

I produced replicas of the device designed by Ferry *et al.* [57] thanks to the master–mold that Prof. Jeff Hasty kindly provided to us as a blueprint, according to the protocol procedures described in Appendix B.1.1 and published in [57].

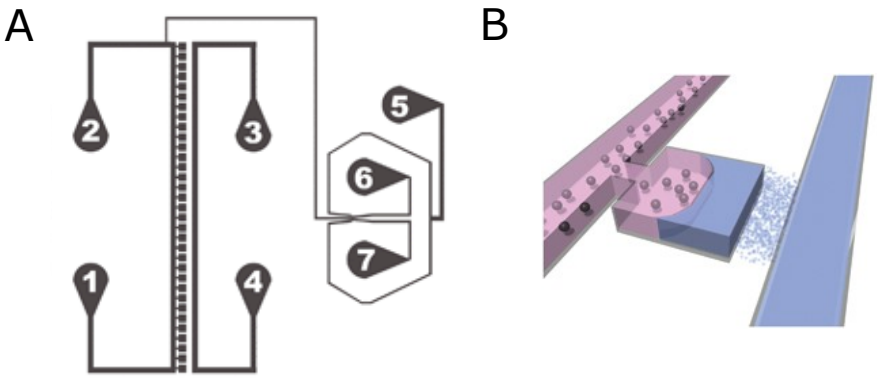

Figure 2.3: **Microfluidic device for mammalian cells culture.** (**A**) Overview of the mammalian chip's architecture. (**B**) Vacuum-assisted loading of cells. Upon application of a vacuum, fluid containing cells is rapidly drawn into the culture chambers and fills the traps. Adapted from [59].

2.1.2 Microfluidic device for mammalian cells culture

Differently from yeasts, mammalian cells are much more sensitive to small changes in pH, osmolarity, shear stress, and other external factors than most microbial model organisms. To overcome these problems, for experiments in which mammalian cells were involved, I chose to use another microfluidic device, always developed in the laboratory of Prof. Jeff Hasty [59]. This device, shown in Fig. 2.3A, consists of 33 individual cuboid culture chambers (each has a 230 μm by 230 μm footprint, 40 μm height), that are isolated from the shear stress. A main perfusion channel of identical height runs adjoining to the chambers and allows delivery of the input to the cell via a 50 μm wide opening on one side of each chamber. A separate channel for the application of a temporary vacuum runs parallel to the column of culture chambers at a distance of 160 μm between the wall of this channel and the closest wall of each cuboid chamber. This channel is used during the cell loading (see Section B.3.3) to draw a fluid containing a cell suspension into the culture chambers upon the application of a temporary vacuum at the gas-permeable PDMS interface, as shown in Fig. 2.3B. Upstream the main perfusion channel, there are the same DAW and SHM previously described (see Section 2.1.1).

Even in this case, I produced replicas of the Kolnic device [57] thanks to the mas-

ter–mold that Prof. Jeff Hasty kindly provided us as a blueprint, according to the protocol procedures described in Appendix B.1.1 and published in [59].

2.2 Actuation system

As mentioned previously, the DAW is designed to combine the inputs from input ports of both microfluidic devices in a precise ratio by changing the relative pressures at the DAW, while keeping the total pressure constant. Thus, the input concentration in cell chambers depends only on the pressure difference at the inlets. To this end, the pressure of one inlet is increased and the other decreased by the same amount.

Theoretically, by controlling the inlet pressures as a function of time, one can generate precise waves of inducer concentration reaching the cell trap. The actuation aim is to establish this pressure difference. Physically, this can be achieved by changing the hydrostatic pressure of the syringes linked to the two inlet ports.

To accomplish this, we used two vertically mounted linear actuators, shown in Fig. 2.4, to physically move the filled syringes up and down, thereby altering their hydrostatic pressures. The syringes in this design have no plunger since they are used simply as tanks to store the media. Namely, each syringe will exert a hydrostatic force over the fluids in the channel that is simply proportional to its height.

The actuation system comprises two linear guides; every linear actuator is designed to move independently from the other; the motion is realised through a stepper motor, while the transmission by using a timing belt and two pulleys. Further details regarding the sizing and the specifications of the actuation system are reported in [60, 61]

2.3 Microscopy and image analysis

Phase-contrast and epifluorescence images were acquired at 2 min (yeast cells) or 15 min (mammalian cells) intervals at 40x magnification (CFI Plan Fluor DLL 40x dry objec-

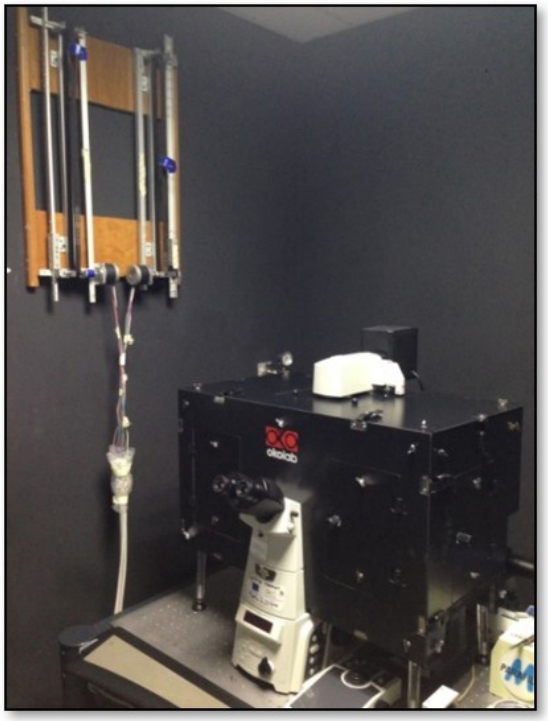

Figure 2.4: **Linear actuators and Nikon Eclipse Ti fluorescence microscope.** The picture shows the fluorescence microscope (Nikon Eclipse TI) and the linear actuator used in this study.

tive, NA 0.75; Nikon Instruments) using a Nikon Eclipse Ti-E inverted microscope (Nikon Instruments) coupled with an EMCCD cooled camera (iXon Ultra 897; Andor Technology) (Fig. 2.4). The microscope stage was surrounded by an opaque cage incubator (Okolab) able to maintain the temperature at either 30 °C (nominal condition) or 27 °C (perturbed condition) for yeast cells and 37 °C for mammalian cells. Time-lapse experiments were conducted with the Perfect Focus System (Nikon Instruments) enabled. Appropriate filter cubes were used to acquire the yellow (FITC; Nikon Instruments), the red (TRITC HYQ; Nikon Instruments), and the green (Piston GFP Bandpass Emission; Nikon Instruments) fluorescence channels. Time-lapse image acquisition was controlled by the NIS-Elements Advanced Research software (Nikon Instruments).

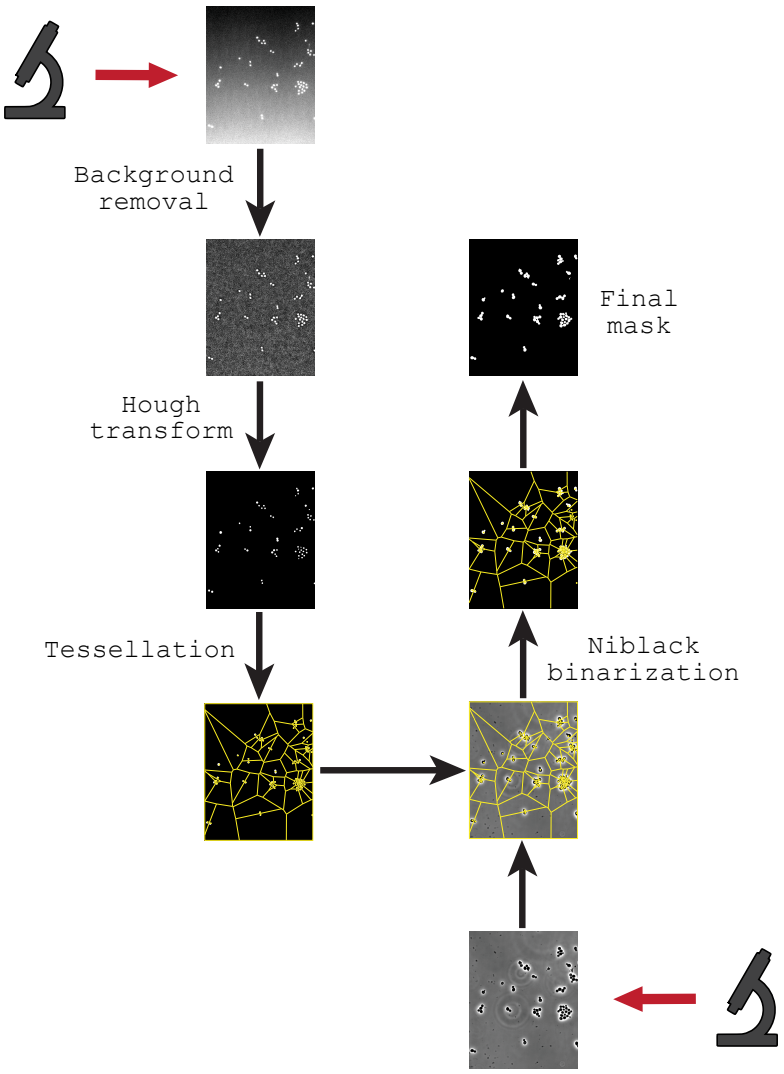

Figure 2.5: **Yeasts segmentation pipeline.** It is based on the tessellation of phase-contrast images, upon nuclei recognition, to better distinguish single cells.

2.3.1 Segmentation of yeast cells

For the experiments that involved yeast cells, I processed raw phase-contrast and epi-fluorescence images using custom scripts implemented in the MATLAB environment and available on *GitHub* (see Appendix B.4). With this algorithm, whose pipeline is shown in Fig. 2.5, I localised yeast cells in real-time, frame-by-frame, by processing the raw images with a custom segmentation and tracking algorithm based on the Htb2-mCheery protein used as a nuclear marker. Then, I quantified single-cell fluorescence by measuring the intensity of the pixels in fluorescence images.

Firstly, raw phase-contrast images were enhanced by using the MATLAB function `imadjust` of the *Image Processing Toolbox*. Then, I used the MATLAB function `fspecial` of the *Image Processing Toolbox* to design a Gaussian low pass filter, which was applied to the enhanced images with the MATLAB function `imfilter` of the *Image Processing Toolbox*. Next, background pixels were detected in both fluorescence images (yellow and red fluorescence channels) by performing a morphological opening using the MATLAB function `imopen` of the *Image Processing Toolbox*, which removes objects that do not completely contain a specific structuring element. I chose a disk-shaped structuring element (radius equals to 5 px) to detect the fluorescence emitted by histone Htb2-mCherry, i.e. the cell nuclei, in the red images acquired. Instead, I chose a disk-shaped structuring element (radius equals to 10 px) to detect the cytosolic fluorescence emitted by YFP expressed from the endogenous promoter P_{CLN2} in the yellow images acquired for the non-cycling strain. Each structuring element was created through the MATLAB function `strel` of the *Image Processing Toolbox*. The selected background was then removed by subtraction from the raw fluorescence image by using the MATLAB function `imsubtract` of the *Image Processing Toolbox*. Next, cell nuclei were detected in the red background-removed images. Specifically, I first binarized each red image using Bradley's method [62] implemented in the MATLAB function `imbinarize` of the *Image Processing Toolbox*. Then, I removed connected components (i.e., objects) that had fewer than 20 px from the resulting binarized images using the MATLAB function `bwareaopen` of the *Image Processing Toolbox*. Assuming a circular shape for each nucleus, I detected the cell nuclei in the red images employing the circular Hough Transform [63] implemented in the MATLAB function `imfindcircles` of the *Image Processing Toolbox*. This function returned a two-column matrix containing the centroids of the nuclei found in the red binarized images. The red binarized images were also used to quantify the nuclei's fluorescence using the MATLAB function `regionprops` of the *Image Processing Toolbox*. Specifically, the function `regionprops` quantified the mean fluorescence signal of every

single connected component identified in the red binarized image. Note that the fluorescence intensities are measured in arbitrary units (a.u.). Single connected components with a mean fluorescence intensity below a threshold value (i.e., 45 a.u. in our setup) were not considered as nuclei, thus the corresponding centroids were discarded from the image processing algorithm. Next, the nuclei centroids were used as seeds for a Voronoi tessellation to generate a single-cell region mask for each Voronoi cell area. The creation of region masks from the Voronoi tessellation was performed through the function `vonoroi2mask` available at the MATLAB *Central File Exchange* [64]. Region masks were then used to define rectangular boundaries that were used to crop the phase-contrast images around each cell. Next, a Gaussian low pass filter was once more applied on the cropped phase-contrast images. Then, I applied a Niblack local thresholding method [65] to the cropped phase-contrast images through the function niblack available at the MATLAB *Central File Exchange* [66]. Finally, a watershed algorithm, implemented through the MATLAB function `watershed` of the *Image Processing Toolbox*, was applied on the resulting phase-contrast images to generate a binary mask defining the region of a single cell.

At this stage, each nucleus detected in the red images should be associated with one single-cell mask. However, two or more cells could be detected in a single Voronoi region. In this case, I identified the centroid and the corresponding radius of each single-cell mask detected in the same Voronoi region using the function `regionprops`. Specifically, the centroid and the corresponding radius were defined as the centroid and the half of the major axis length (measured in px) of the ellipse that has the same normalised second central moments as the region defined by the single-cell binary mask. Then, I evaluated the Euclidean distance between the centroid's nucleus (i.e., the centroid detected in the red binary image) and the centroid detected for each single-cell mask. I associated the cell nucleus to the single-cell mask whose Euclidean distance was less than the associated cell radius. Also, I applied the function `regionprops` to all the single-cell mask to quantify the radius of each cell. The radius was defined

as stated previously, that is the half of the major axis length (measured in px) of the ellipse that has the same normalised second central moments as the region defined by the single-cell binary mask. Correction strategies were employed when the custom algorithm failed in associating a nucleus to a binary mask. In the case that the nucleus was detected for the first time, a circular binary mask was generated using a circular shape centred on the centroid of the detected nucleus and having a radius equals to 3 px (i.e., the measured cell dimension at birth). In the case that the nucleus was already recognised in the previous frame, then the algorithm considered the binary cell mask detected in the previous frame. The same correction was also applied when the Niblack local thresholding method failed. Specifically, the thresholding method failed when the single-cell mask area was less than one and half times the single-cell mask area computed in the previous time frame. The single-cell mask area was computed with the MATLAB function `regionprops`.

Fluorescence intensities were then quantified by processing the yellow fluorescence images with the binary single-cell masks described above. Specifically, the binary mask defines the pixels of the phase-contrast and fluorescence images associated with the single yeast cell. The fluorescence is quantified using the function `regionprops`. Specifically, the fluorescence is quantified as the average fluorescence intensity in the region selected by the binary mask.

Single-cell traces were tracked in real-time using a custom tracking module, which was previously described [56], that searches for the correspondences between the objects (i.e., the centroids of the nuclei) detected in two consecutive red fluorescence images by minimising a cost configuration (i.e., the displacements among the centroids of two consecutive images). To improve the single-cell traces, I devised an offline implementation of the tracking module that performs also reverse tracking of the cell population, which means that the tracking module was run a second time starting however from the last time frame towards the first frame. Thus, I obtained a reverse single-cell traces dataset. Then, the algorithm combines the forward and the reverse datasets to

improve the single-cell traces by performing the following steps: (i) the algorithm extrapolates the first and the last frame of each single-cell trace in both datasets. Note that I mean as first frame the frame in which the cell is tracked for the first time, while as last frame the frame in which the cell appears for the last time in the time-lapse experiment; (ii) identification of forward and backwards traces that have in common the first and the last frame in time. For each set of cell traces that overlap for the full time interval, I first evaluated the Euclidean distance of the centroids between the forward and the reverse single-cell traces over time. The algorithm evaluated the Euclidean norm of the vector composed by the Euclidean distances between each pair of forward and reverse traces. If the Euclidean norm is less than 1 px, then the algorithm combines the forward trace and the reverse trace in a unique single-cell trace. To compute the Euclidean norm, I use the MATLAB function `norm`; (iii) identification of forward and backward traces overlapping only for a partial time interval. The algorithm computes the Euclidean distance between the centroids of the forward and reverse single-cell traces by considering only the overlapping time interval. If the Euclidean norm of the vector containing the Euclidean distances between the forward and the reverse overlapping traces is less than 1 px, then the algorithm merges both traces in a single-cell trace. This step is iteratively repeated until no other matches were found; (iv) correction strategies to reconstruct the final single-cell traces. To this end, the algorithm considers the case in which the tracking algorithm failed in following a single cell between two frames. Specifically, the algorithm searches for consecutive single-cell traces, meaning that the first frame of one trace should be the last frame of the other trace. The algorithm merges the two single-cell traces if the Euclidean distance between the centroids belonging to the two boundary frames (i.e., the last frame of one and the first frame of the other trace) is less than 5 px. This step is iteratively repeated until no other matches are found. A second correction considers the case in which the tracking algorithm failed in following a single cell assuming that the cell could be lost for one frame. In this case, the algorithm applies the same correction strategy illustrated previously. Since every step is iteratively

repeated, duplicates of single-cell traces could appear in the final dataset. Thus, a filtering step is also implemented through the unique identification of each single-cell trace used to perform the merging algorithm. Specifically, each merged single-cell trace is associated with the single-cell label used for the merging. If the same labels are saved in more than one single-cell trace, just the longest trace is conserved by the algorithm.

2.3.2 Segmentation of mammalian cells

In the case of mammalian cells, I quantified single-cell fluorescence by analysing epi-fluorescence images using a custom algorithm, whose pipeline is depicted in Fig. 2.6, implemented by combining a machine-learning based approach and a MATLAB script, available on *GitHub* (see Appendix B.4).

First, I process the raw phase-contrast images by using a machine-learning algorithm, *FastER* [67] (available on the *website*), which gives as output the binary masks used as input for the custom algorithm described below.

Background pixels are removed in both green and red fluorescence images by performing a morphological opening as done for yeast cells images. In the case of mammalian cells, however, I chose a disk-shaped structuring element with a radius equals to 40 px to apply to both images. Then, the nuclear fluorescent protein H2b-mCherry is used to localise the nuclei in the fluorescence images in the red spectrum. To this end, I enhance the contrast in the background-removed red images through the MATLAB function `imadjust` of the *Image Processing Toolbox*. Next, I binarize these images using Otsu's method [68] implemented with the MATLAB function `imbinarize` of the *Image Processing Toolbox*. Two cells may be too close to each other or a single cell may have more than one nucleus. In these cases, the binarised images may incorrectly merge two or more different nuclei in one single object. To avoid this problem, after having filled the holes in the binary images through the MATLAB function `imfill` of the *Image Processing Toolbox*, the algorithm applies a new method to separate touch-

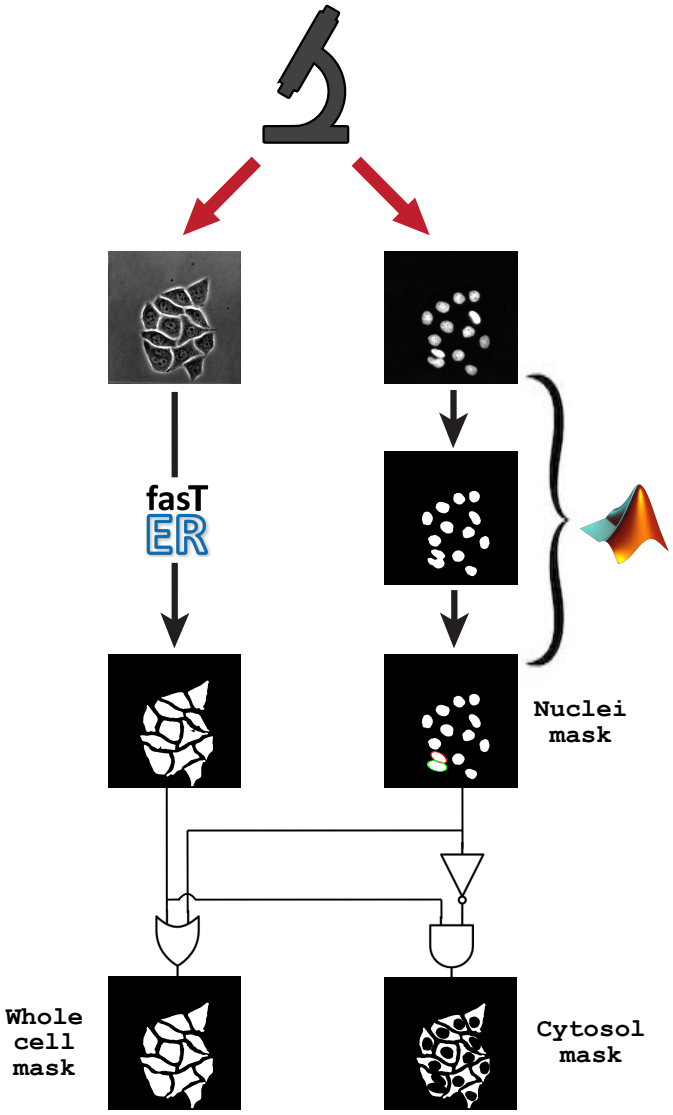

Figure 2.6: **Mammals segmentation pipeline.** It is a combination of a machine-learning based algorithm (*FastER* [67]) for phase-contrast image segmentation and a custom script implemented in MATLAB environment for nuclei segmentation.

ing cells, known as pixel replication [69], that combines the Euclidean distance transform and Gaussian mixture models to better delineate objects with elliptical boundaries. Specifically, this method is applied only to those nuclei whose area, computed with the MATLAB function `regionprops` of the *Image Processing Toolbox*, is a multiple of 1400 px, which is the mean area of the mammalian cells imaged in this Thesis (HeLa).

At this point, for each image, two binary masks are built: (i) the mask for the entire cell obtained with FastER, and (ii) the nuclei mask obtained by the described algo-

rithm. Through logic operations between these two images, I obtain also the mask to measure cytosol fluorescence. Each nucleus in the nuclei mask is then associated to a single cell in the cell mask, by computing, through the MATLAB function `norm`, the Euclidian distance between the centroids of the two masks evaluated by the function `regionprops`. Specifically, the nucleus is associated with the cell whose radius is longer than the Euclidian distance. The cell radius is defined as the half of the minor axis length (measured in px) of the ellipse that has the same normalised second central moments as the region defined by the single-cell binary mask, estimated through the function `regionprops`. Since FastER works on the contrast difference between foreground and background, it may not always be able to detect all the cells in the image or it may partially detect other cells. To improve the quality of FastER masks, I employed some correction strategies. Specifically, I combined the single-cell mask with the single-nucleus mask through the logical operator OR, in case FastER had detected only part of a cell. However, if a nucleus cannot be associated with any cell detected by FastER, the cell mask is recovered from the previous frame. Once that each nucleus is associated to a cell, the cytosol mask can be computed by applying the AND operator between the single-cell mask and the negative of the single-nucleus mask.

Finally, the green fluorescence of both the whole cell and of the individual compartments (nucleus and cytoplasm) can be estimated. Specifically, making use of the function `regionprops`, I evaluate the intensity of each pixel in each mask (whole cell, cytoplasm, and nucleus) and the compartment fluorescence is defined as the sum of the intensity of all pixels formed the compartment.

Also for mammalian cells, single-cell traces are tracked through the tracking module previously described (Section 2.3.1) [55].

During the experiment, cells can divide or can die and these events affect also the single-cell fluorescence traces. During cell division and cell death, a cell loses its normal shape and compartmental division. Therefore, since I was interested in observing the nuclear translocation of a fluorescent protein (see Section 4.3), these phenomena

can interfere with the signal. Moreover, some cells are not fluorescence at all making observing the translocation impossible. To avoid these problems, I performed a cell selection, discarding the non-fluorescent cells and cutting the signals during cell division or death.

Chapter 3

Automatic control of the yeast cell cycle

In this Chapter, I will illustrate the potentiality of cybergenetics. As discussed in Section 1.2, cybergenetics approaches have been used to steer simple biological processes. In this work, for the first time, we applied cybergenetics tools to a very complex biological pathway: the cell cycle. Normally, yeast cells cycle asynchronously, increasing cellular heterogeneity and allowing the survival of the population in unfavourable conditions [70]. However, in several cases, a synchronised population is desirable. For example, a synchronised population can be used to study the mechanisms steering the eukaryotic cell cycle or to optimise cell-cycle modulated production of metabolites and heterologous proteins [71, 72]. Here, I describe the design and implementation of an external control strategy to synchronise the cell-cycle across a population of yeast cells through the experimental platform illustrated in Chapter 2.

The work illustrated in this Chapter was realised in collaboration with Giansimone Perrino, a post-doc previously worked in Prof. Diego di Bernardo's group. Part of these results have been published in a peer-reviewed journal [73].

3.1 The cell-cycle machinery

The cell cycle is the succession of events whereby a cell grows and divides into two daughter cells, each one containing the information and machinery necessary to repeat the process. In unicellular species, such as bacteria and yeast, each cell division produces a completely new organism, while in multicellular species, long and complex sequences of cell divisions are required to produce a functioning organism.

The details of the cell cycle vary from organism to organism, even if certain characteristics are universal. Specifically, some steps of this process are fundamental to pass the genetic information to the daughter cell, which is the main task of the cell division process. To this end, indeed, the DNA has to be accurately replicated and distributed between the two daughter cells. To ensure that this task is properly performed, a complex network of regulatory proteins, known as cell-cycle control system, was evolved in eukaryotic cells. This system monitors the progression through the cell cycle and delays later events until earlier ones have been completed [74, 75].

The cell cycle is traditionally divided into four phases: (i) the Gap1 (G_1) phase; (ii) the Synthesis (S) phase; (iii) the Gap2 (G_2) phase; and (iv) the Mitosis (M). The two gap phases are needed to allow cells to grow and double their mass of proteins and organelles to pass to the daughter cells. The synthesis phase is the set of processes that leads to the DNA synthesis (from which it takes its name); while mitosis is the actual cell division. The combination of the two gap phases with the S phases is also known as interphase. During the gap phases, the cells also monitor internal and external environments to ensure that external conditions are suitable for cell division and that the cell has completed the preparation for the next step. In this context, another cell-cycle phase was identified: the G_0 or gap zero phase. In case of unfavorable conditions, indeed, a cell uses this phase to wait for more suitable circumstances to progress through an irreversible point at the end of the G_1 phase: the Start (in yeast) [76] or the restriction point (in mammalian cells) [74, 75]. After passing this point, cells enter the S phase. In

addition to this transition, there are other points in the cell cycle, called checkpoints, at which the cell cycle can be arrested if the conditions are not ideal to progress towards the cell cycle or if previous events have not been completed. First of all, the entry in mitosis is prevented when DNA replication is not complete (DNA replication checkpoint), and chromosome separation in mitosis is delayed if some chromosomes are not properly attached to the mitotic spindle (spindle-attachment checkpoint). Moreover, progression towards G_1 and G_2 is delayed in case of DNA damages to give the cell the time to repair the DNA [74, 75].

The budding yeast *Saccharomyces cerevisiae* is the model organism most used to study the cell cycle [75]. It is an oval cell that divides by forming a bud, which first appears in the late G_1 phase and grows to become the daughter cell at the end of the mitosis when it separates from the mother cell. The advantages of using this organism as a model to study the cell cycle are that it reproduces quite rapidly (in about 80 min [77]) and can be easily genetically manipulated by deleting, replacing, or altering some genes [75]. Moreover, it is quite simple to identify a cell-cycle arrest by observing the bud, particularly its presence - or absence - and its size [75].

The cell-cycle control system is mainly regulated by the oscillatory activity of a family of proteins known as cyclin-dependent kinases (Cdks), which cyclically phosphorylate intracellular proteins that regulate major cell-cycle events. In budding yeast cells, a single Cdk protein (Cdk1, previously known as Cdc28) exists [78]. The oscillations in Cdk activity are controlled by a complex network of enzymes and proteins, including the cyclins (from which Cdk takes its name) [78]. Indeed, the binding of a cyclin to Cdk activates the phosphorylation activity of Cdk itself. Moreover, cyclins direct Cdk to its specific target proteins, with the result that each cyclin-Cdk complex phosphorylates a different set of proteins. Cyclins are classified based on the phase of the cell cycle during which they bind Cdk: (i) G_1-cyclins, i.e. the Cln3 protein in budding yeast [76], promote the passage through the Start (or restriction point) in late G_1; (ii) G_1/S-cyclins, i.e. Cln1 and Cln2 in yeast [76], bind Cdk at the end of G_1 preparing

the cell for the DNA replication; (iii) S-cyclins, i.e. Clb5 and Clb6 in yeast, bind Cdk during the S phase allowing the DNA replication; (iv) M-cyclins, i.e. Clb1, Clb2, Clb3 and Clb4 in yeast, promote the mitosis [74, 75].

To enable the oscillatory activation of Cdk, the cell-cycle control system depends crucially on proteolysis that inactivates it, through a ubiquitin-dependent mechanism. Two different ubiquitin ligases (enzymes that catalyse the ubiquitin-transfer reaction) are important in the cyclin destruction and act in different cell-cycle stages: the SCF complex that is responsible for the ubiquitylation during the G_1 and S phase; and the anaphase-promoting complex (APC) responsible for the proteolysis of the M-cyclins regulating the spindle-attachment checkpoint [79, 80]. The APC complex activity is stimulated by M-cyclins themselves. This means that it can be rapidly deactivated during the G_1 phase leading to a too fast M-cyclins accumulation, that does not allow the cell growth during gap phases [81]. Thus, most cells employ several mechanisms to ensure that Cdk reactivation is prevented after mitosis. Specifically, Cdk inhibitor proteins (CKIs) suppress the Cdk activity during the G_1 phase. Budding yeast cells, particularly, contain a CKI named Sic1, which binds to and inactivates the M-Cdk in late mitosis [81, 82]. Meanwhile, the accumulation of G_1 cyclins leads to an increase in G_1-Cdk activity allowing the progression towards the S phase. This complex mechanism is, however, regulated at many levels. Particularly, the activity of a cyclin-Cdk complex can be inhibited also by phosphorylation through a protein kinase known as Wee1, while the phosphatase Cdc25 dephosphorylates the complex increasing Cdk activity [83, 84]. Specifically, this de/phosphorylation modulation is fundamental for the regulation of the DNA replication checkpoint and in the activation of the M phase [83, 84].

A simplification of the cell-cycle control system is shown in Fig. 3.1 [85]. The complex network previously described, indeed, can be summarised by considering the interactions between the G_1-cyclins, the M-cyclins, and the APC complex. This simplified version of the cell-cycle control system is formed by: (i) a PFL in the production of G_1 cyclins, which can induce their transcription; (ii) an IFFL that regulate the transcrip-

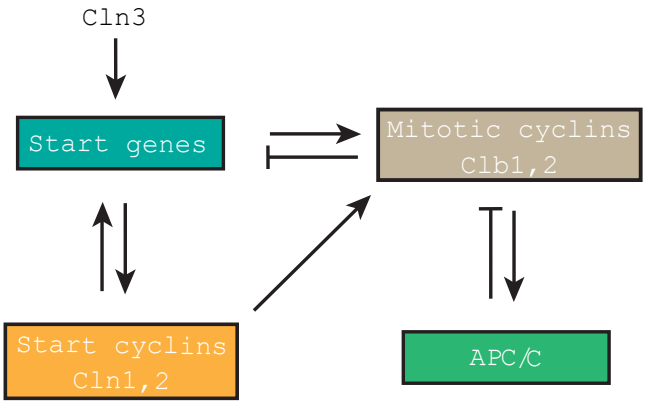

Figure 3.1: **Schematic of Cdk–APC/C cell cycle control system in budding yeast.** Adapted from [85]

tion of G_1 cyclins through the G_1 cyclins themselves and the M cyclins; (iii) two early NFL involving the G_1 cyclins, their genes, and the M cyclins; and (iv) a late NFL based on the M cyclins and the APC complex that controls the exit from the cell cycle [85].

For most cells, the cell cycle is strictly coupled to cell size homeostasis. Indeed, the duration of the cell cycle must match the time it takes for the cell to double in size: if the cycle time is shorter than this, the cells will get smaller with each division; if it is longer, the cell will get bigger after each division. However, the mechanisms that steer this coupling are not completely understood. For a long time, it was assumed that budding yeasts coordinate their growth and cell cycle by monitoring the total amount of Cln3 [78, 86, 87]. Because Cln3 is synthesised in parallel with cell growth, its concentration remains constant while its total amount increases as the cell grows [88, 89]. To monitor the amount of Cln3, probably, cells have a fixed amount of Cln3 inhibitor that can bind to Cln3 and block its activity. When the Cln3 amount exceeds the inhibitor amount, the extra Cln3 triggers G_1-Cdk activation. However, cells in which Cln3 was deleted are still able to trigger cell division and to keep the coordination between cell growth and division [90]. This suggests that other mechanisms are implicated in this coupling enabling the robustness of the cell-cycle machinery. Although cell growth and division are usually coordinated, they can be regulated independently: yeast cells can grow even when cell-cycle progression is blocked by a mutation.

3.1.1 Biological methods to synchronise the cell-cycle

In some situations, a synchronised population (i.e. a population able to replicate in a synchronised manner) is required. To this end, several experimental approaches to synchronise cells have been proposed over more than 20 years of research [91–95]. They can be divided into two classes: physical selection or chemical induction. In the first case, the strong interconnection between the cell-cycle phase and the cell size is exploited. Indeed, with these methods, cells are separated according to their size and then cells of the same size are grown together. In the case of chemical induction, instead, cells are forced to start cycling from the same initial condition. Particularly, cells are blocked in the same cell-cycle phase thanks to the presence, or absence, of one or more chemicals in the growth medium and, then, released all together by changing the growth medium. Moreover, different cell-cycle mutants are used. In this case, the mutants were made to start in response to temperature shift or metabolite concentrations.

These approaches, however, can not synchronise cells for a long time. The synchronisation is, indeed, lost in a few cycles [96], demonstrating the robustness of the cell-cycle machinery. This desynchronisation is due to the coupling between cell size and division. Accordingly, the asymmetry in size between mother (larger) and daughter cells (smaller) is the main reason for the loss of synchronisation [97]. Indeed, cells need to reach a critical volume before entering the cell cycle, thus limiting the duration of synchronisation [72]. Moreover, when cells are grown in secondary carbon sources (e.g. galactose), the cell cycle slows down thus enhancing the difference between mother and daughter cells and causing desynchronisation after only one cycle [72].

Finally, continuous culture systems have also been proposed to keep the synchronisation for longer. With this technique, cells are periodically starved to block cell division and released by exposing them to nutrients. This approach presents numerous drawbacks: it is stressful for the cells and not robust since the frequency and magnitude of starvation pulses need to be known beforehand [92, 98]. To overcome this

issue, a self-cycling fermenter was developed. In this fermenter, the dissolved oxygen is measured and used to detect the nutrient depletion and trigger the removal of half the fermenter content and its replacement with fresh medium [98]. Although this approach allows the scale-up to larger cultures, it is stressful for the cells as it causes the periodic exit from the exponential growth phase reaching the stationary phase and slowing down the cell growth.

3.2 A yeast strain to control the cell-cycle

To tackle the synchronisation task, I made use of a budding yeast strain genetically engineered to start the cell cycle upon the application of an external input, as schematised in Fig. 3.2A. Specifically, I exploited a methionine-repressible system that allows cell division upon removal of the amino acid methionine from the growth medium [99].

This strain, that we named *non-cycling* strain, was engineered by Rahi *et al.* [82]. As shown in Fig. 3.2B, in this strain, endogenous control of cell cycle initiation is disrupted by deletion of the genes encoding for the G1 cyclins Cln1, Cln2, and Cln3 [100]. To enable the cell-cycle progression towards the S phase, an exogenous *CLN2* is placed downstream of the methionine-repressible promoter P_{MET3} to allow its inducible expression [99]. Therefore, cells are blocked in the G1 phase when grown in a methionine-rich medium, as highlighted in Fig. 3.2C. Furthermore, remembering that yeast cells grow in size mainly during the G_1 phase, it is expected that cells grown methionine-rich medium tend to become very huge, as confirmed by phase-contrast images in Fig. 3.2C. These images, indeed, are representative of non-cycling strain behaviour: in methionine-rich medium (upper line), cells do not replicate and continue to grow in size; in methionine-poor medium (lower line), cells replicates and last in their physiological size.

To track the cell-cycle progression in time, a yellow fluorescent protein (YFP) was placed downstream of the endogenous P_{CLN2} promoter. Following the expression of the G_1 cyclins, the YFP has an oscillatory expression peaking in the late G_1 phase, as

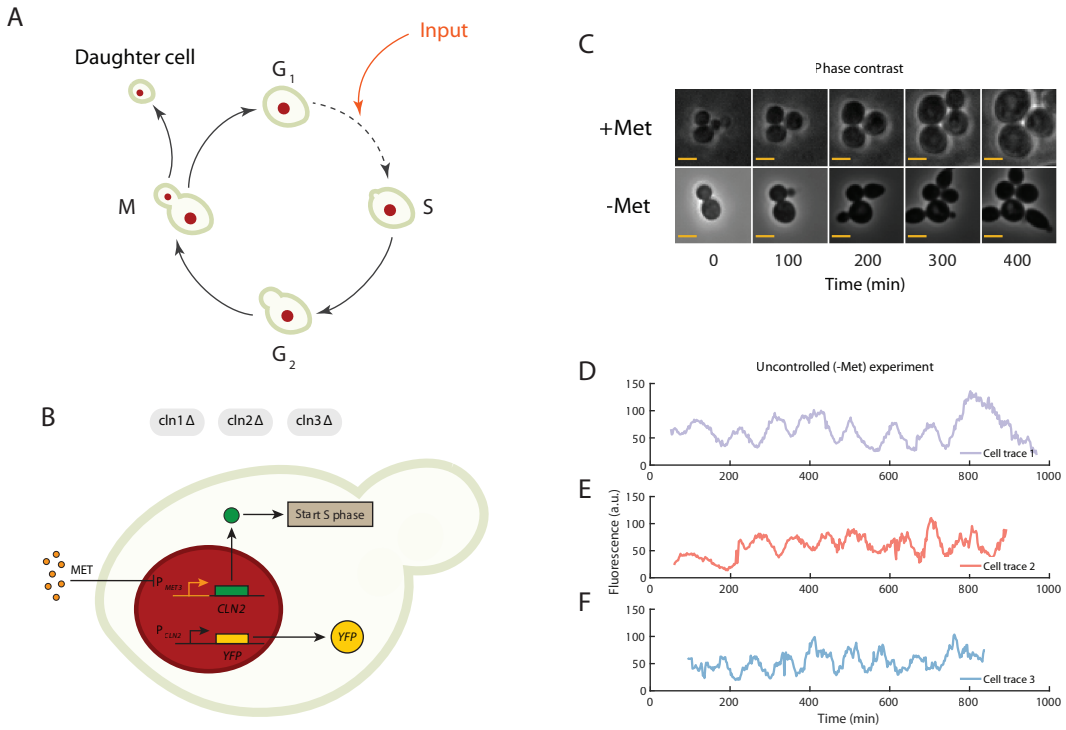

Figure 3.2: **Non-cycling strain: a yeast strain to control the cell-cycle.** (**A**). The yeast strain was manipulated genetically to place Start, the point of irreversible commitment to cell division (i.e., G_1/S transition), under control of an exogenous input. Particularly, in this strain cells can cycle only in the presence of the external input (as highlighted by the dashed line). (**B**). The endogenous genes encoding for the G_1 cycling Cln1-3 are deleted and an exogenous G_1 cycling gene *CLN2* is placed under the control of the methionine-repressible promoter P_{MET3}. A yellow fluorescent protein (YFP) is expressed under the control of the endogenous P_{CLN2} promoter. (**C**). Representative phase contrast images from two independent time-lapse experiments of cells grown in methionine-rich medium (top) and methionine-depleted medium (bottom) at the indicated time points. Scale bar, 5 μm. (**D-F**). YFP fluorescence intensity measured in three representative cells grown in methionine-depleted medium.

shown in Fig. 3.2D-F, where an example of the YFP expression of three different cells is plotted. Finally, a constitutively expressed histone Htb2-mCherry acts as a nuclear fluorescence marker for facilitating image analysis.

3.2.1 Cell-cycle phase estimation from fluorescent data

The cell-cycle phases of individual cells are not directly measurable but they have to be estimated from fluorescent data. To this end, I implemented a custom algorithm, available on *GitHub* (see Appendix B.4), based on the characteristics of the fluorescent signal. Particularly, the cell-cycle phase $\vartheta \in [0, 2\pi]$ was estimated by comparing the single-cell *CLN2-YFP* trace with a periodic reference signal [73].

The periodic reference signal $\mathrm{CLN2}_{ref}$ was constructed according to the expected dynamical expression of the essential G1 cycling gene *CLN2*. Specifically, it is formed by two part. The first part is used to describe the situation in which the cell is halted in the G_1 phase, which means that the cell has a flat fluorescence signal. The second part, instead, models the oscillatory *CLN2-YFP* expression in a cell that is cycling, i.e. when it is fed with the methionine-free medium. Therefore, the reference signal can be written as follows:

$$CLN2_{ref}(t) = \begin{cases} 0 & \text{if } kT \leq t < kT + T_{flat} \\ \frac{1}{2} - \frac{1}{2}\cos(\frac{2\pi}{T_0}t) & \text{if } kT + T_{flat} \leq t < (k+1)T \end{cases}, \tag{3.1}$$

where $T = T_0 + T_{flat}$ is the period of the reference signal T_{flat}, set equal to the length of the compared fluorescence signal, is a fake time interval in which the cell is assumed to be halted in the G_1 phase, and $T_0 = 75\,\mathrm{min}$ is the nominal cell cycle period [85].

At each sampling time t, the measured fluorescence signal was cross-correlated with the periodic reference signal by evaluating the Pearson's correlation coefficient r through the MATLAB function `corr`. Specifically, the last part of the measured fluorescence signal of duration $T_{flat} = 30\,\mathrm{min}$, *CLN2-YFP*$(t - T_{flat}, t)$, was cross-correlated with the periodic reference signal using a shifting time window in the interval $[\tau - T_{flat}, \tau]$, where $\tau \in [T_{flat}, T]$. The time point τ at which the correlation r assumed its maximum value was used as time reference to estimate the cell-cycle phase $\hat{\vartheta}$ as fol-

lows:

$$\hat{\vartheta} = \frac{2\pi}{T_0}(\tau - T_{flat}) + \frac{\pi}{2}. \tag{3.2}$$

At the M/G_1 transition, the cell-cycle phase was set $\hat{\vartheta} = 0$, while the length of the G_1 phase was set to 25% of the nominal cell-cycle period [101].

The cell-cycle phase estimation enables to compute the Budding Index (*B.I.*), that is the percentage of cells in budding phase (i.e. S-G_2-M phases):

$$B.I.(t) = \frac{N_{\text{S-G2-M}}(t)}{N(t)}\,100, \tag{3.3}$$

where $N(t)$ is the total number of cells at time t and $N_{\text{S-G2-M}}(t)$ is the number of budded cells at time t. The *B.I.* can be, in fact, used as a synchronisation measure: if the cells were synchronized, they should simultaneously in the budded or unbudded phase. Thus, in a synchronised population, the budding index should switch between 0% and 100% in a periodic manner.

3.2.2 Experimental characterization of the non-cycling strain

I carried out an experimental characterisation of the non-cycling strain to check its behaviour in nominal conditions: in methionine-rich and -depleted medium. To this end, yeast cells from non-cycling strain were let to grow into the microfluidic device delivering them either a medium enriched or depleted in methionine for 1000 min. The results of these experiments are shown in Fig. 3.3.

In a methionine-rich medium, cells grow in volume (Fig. 3.2C) but fail to divide for at least 6 h, as shown in Fig. 3.3A-C. Indeed, some cells were able to replicate after this time, albeit very slowly, possibly because of the accumulation of *CLN2* caused by the promoter's leakiness. Because of the stop in the G_1 phase and the abnormal cellular growth, cells started to have not physiological shapes, size, and protein production, making image segmentation and tracking (see Section 2.3.1) difficult and, then, failing

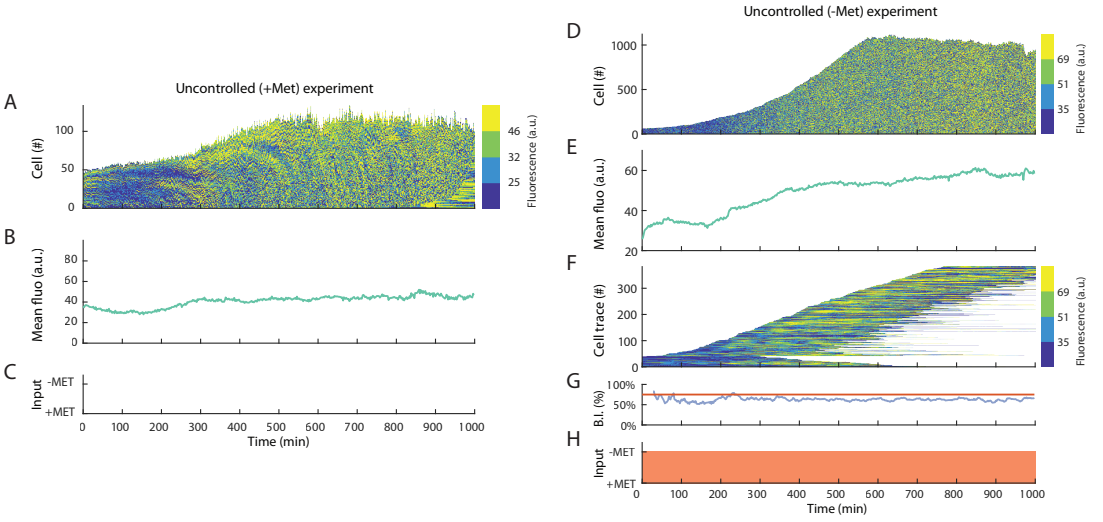

Figure 3.3: **Experimental characterisation of the non-cycling yeast strain.** Yeast cells were let to grow in the microfluidic device in methionine-rich (**A**-**C**) or -depleted medium (**D**-**H**) for 1000 min. (**A**, **D**) Distribution of the YFP fluorescence signals measured across the cell population over time. Fluorescence values are binned into 4 colours, corresponding to the quartiles, for clarity of visualisation. (**B**, **E**) Time-series of the mean YFP fluorescence signal measured across the cell population. (**F**) Single-cell fluorescence traces over time. Each horizontal line corresponds to one cell. (**G**) Time-series of the budding index (blue) signal. The red line denotes the expected value of the budding index in the case of a totally desynchronised cell population. (**C**, **H**) Growth medium delivered to the cells as a function of time. +MET: methionine-rich medium, -MET: methionine-depleted medium.

in the fluorescence quantification and, consequently, in estimating cell-cycle phase. Indeed, as shown in Fig. A.1, going on with the experiment, the nuclei became darker and darker getting worse the segmentation.

In a methionine-depleted medium, instead, cells can cycle, exponentially increasing their number over time (Fig. 3.3D), as shown also by representative phase-contrast images in Fig. 3.2C. Despite the cyclic expression of the YFP reporter in individual cells (Fig. 3.2D, Fig. 3.3F), the YFP fluorescence intensity averaged across the population shows a flat profile (Fig. 3.3E). This is because the individual oscillations in fluorescence were deleted when averaged. Indeed, the average of oscillatory signals, such as those of single-cell fluorescence, is an oscillatory signal itself only if most of the oscilla-

tors are in phase and the amplitude of these oscillations are strictly correlated with how many oscillators are in phase with each other. Finally, the desynchronisation is attested also from the $B.I.$ (Eq. 3.3)(Fig. 3.3G). As expected, as the average YFP fluorescence, it shows a flat profile over time.

This experimental characterisation of the non-cycling strain thus confirmed that it behaves as originally described [82].

3.3 Dynamical model of yeast cell-cycle

The molecular machinery of eukaryotic cell-cycle control is known in more detail for budding yeast *S. cerevisiae* than for any other organism. Hundreds of models have been published with always increasing complexity. Indeed, while early models (and a few more recent ones) were mainly based on a small number of ordinary differential equations relating a few time-dependent variables to each other and to a few time-independent kinetic parameters [102, 103], the last models consist of dozens of variables and regulatory processes [104]. These models are built by using different approaches: ordinary differential equations (ODE) modelling [102–106]; boolean modelling [106–108]; and stochastic modelling [109, 110]. The ODE-based one is what most researchers have focused on since it gets at the basic solution of cell-cycle regulation biochemistry. An almost complete model of yeast cell-cycle, born from the collaboration of three research groups and able to explain most of the possible cell-cycle mutants, is presented on *Prof. Tyson's website* [111].

Since the abundance of details of these models, they are too complex for the aims of this Thesis. Therefore, we explored the phase reduction method [112,113], as explained in [55, 73, 114, 115]. Briefly, as schematised in Fig. 3.4, the cell cycle was modelled as a phase oscillator, which can be depicted as a clock with a single moving arm whose position indicates the phase of the cell and whose length is proportional to the cell volume. Specifically, we derived a deterministic agent-based mathematical model. In

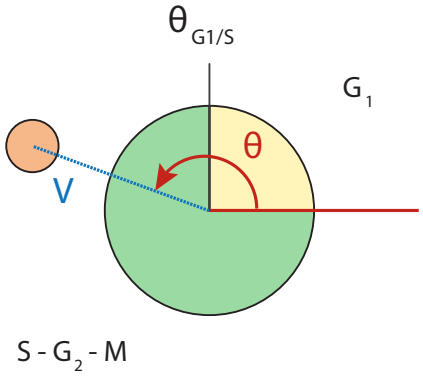

Figure 3.4: **Graphical representation of the mathematical model of the non-cycling strain.** A cycling cell can be represented as circle, where the cell-cycle phase ϑ corresponds to the angle between the red line and the dashed blue line. The length of the dashed blue line represents the cell volume. The yellow shaded sector corresponds to the G1 phase, while the green shaded sector corresponds to the S–G2–M phases. The cell cycle phase evolves counter-clockwise.

this agent-based model, each agent represents a cell in the population. The model of a single agent i is based on a set of two ordinary differential equations (ODEs), that describe the dynamics of the cell cycle phase ϑ_i and cell volume V_i in the i-th cell:

$$\dot{\vartheta}_i = \begin{cases} 0 & \text{if } 0 \leq V < V_C \\ f(\vartheta) + z(\vartheta)\, u & \text{if } V \geq V_C \end{cases}, \tag{3.4}$$

$$\dot{V}_i = g(\vartheta_i)\,, \tag{3.5}$$

where $\theta_i \in \mathbb{S}^1$ is the 2π-periodic cell cycle phase on the unit circle, $V_i \in \mathbb{R}_{>0}$ is the cell volume, $V_c \in \mathbb{R}_{>0}$ is the critical volume, and $u \in \{0,1\}$ is the external trigger input, where $u = 1$ corresponds to methionine-depleted (-MET) medium and $u = 0$ to methionine-supplemented medium (+MET). The critical volume defines the minimum volume required to start the cell-cycle, and it is also used to discern between mother ($V_i \geq V_c$) and daughter ($0 \leq V_i < V_c$) cells. The switching function $f : \mathbb{R}_{>0} \to \mathbb{S}$ models the phase oscillator dynamics taking into account that the cell will stop in the G1 phase

as long as methionine is present in the medium:

$$f(\vartheta) = \begin{cases} 0 & \text{if } 0 \leq \vartheta < \vartheta_{G_1/S} \\ \omega & \text{if } \vartheta_{G_1/S} \leq \vartheta < 2\pi \end{cases}, \tag{3.6}$$

where $\omega = \frac{2\pi}{T} \in \mathbb{R}_+$ is the angular velocity depending from the cell cycle period $T \in \mathbb{R}_{>0}$. The phase-dependent switching function $g : \mathbb{S} \to \mathbb{R}_+$ defines the cell volume growth rate. To simplify the model, we assumed that volume growth in the mother cell occurs only during the G_1 phase, whereas the bud grows in volume only during the S-G_2-M phases [90]:

$$g(\vartheta) = \begin{cases} \beta\, V & \text{if } 0 \leq \vartheta < \vartheta_{G_1/S} \\ 0 & \text{if } \vartheta_{G_1/S} \leq \vartheta < 2\pi \end{cases}, \tag{3.7}$$

where $\beta \in \mathbb{R}_{>0}$ is the volume growth rate, and $\vartheta_{G_1/S}$ is the cell cycle phase value at the G_1 to S transition. Finally, we used the following phase response curve $z : \mathbb{S}^1 \to \mathbb{R}_+$ to model the effect of the control input on the cell cycle phase evolution:

$$z(\vartheta) = \begin{cases} \omega_z & \text{if } 0 \leq \vartheta < \vartheta_{G_1/S} \\ 0 & \text{if } \vartheta_{G_1/S} \leq \vartheta < 2\pi \end{cases}, \tag{3.8}$$

where $\omega_z \in \mathbb{R}_+$ is the angular velocity added to the cell cycle phase dynamics when the cell is fed with methionine-free medium.

To simulate a growing population of yeast cells, the agent-based model also considers cell division events. Indeed, when a cell passes through the M to G_1 transition (i.e., $\vartheta_{M/G_1} = 2\pi$) then a new cell (i.e., a new agent) is added to the model. The initial condition of the daughter cell depends on the state of the mother cell. Specifically, the

initial condition is set to

$$\vartheta_0 = 0\,, \tag{3.9}$$

$$V_0 = \gamma\, V_{M/G_1}\,. \tag{3.10}$$

where V_{M/G_1} is the volume of the mother cell at the division time (i.e., at the M/G_1 transition) and γ is a constant parameter depicting the linear relationship between the size of the mother cell at the division and the size of the newborn daughter cell. Therefore, the number of cells in the agent-based model is an increasing value.

We took the nominal values used to simulate the agent-based model from the literature and are: $V_c = 1$ (critical volume), $\beta = 0.0083\,\mathrm{min}^{-1}$ (volume growth rate) [90], $T = 75\,\mathrm{min}$ (nominal cell cycle period) [85], $\omega_z = \frac{\pi}{T}$ (angular velocity in methionine-free medium), $\vartheta_{G_1/S} = \frac{\pi}{2}$ (phase value at G_1/S transition) [101], and $\gamma = 0.61$ [90].

3.4 Open-loop control

Inspired by the work of Charvin *et al.* [90], I applied an open-loop control strategy to synchronise a population of the non-cycling yeast strain. To this end, the expression of *CLN2* was periodically induced through methionine starvation (-MET) pulses whose period (T_u) and duration (D_{-Met}) have been changed to explore different situations. Specifically, I varied T_u between 60 min and 150 min, while D_{-Met} was set to 20 or 30 min.

Firstly, I stimulated cells in the microfluidic device at their nominal cell cycle period (75 min) with a stimulus duration equal to 30 min. Experimental results, shown in Fig. 3.5A-E, demonstrate that this strategy is effective to synchronise the cell cycle. Indeed, the fluorescence intensities of cells over time, in Fig. 3.5A, show a clear vertical pattern, indicating that cells are mostly in the same cell cycle phase; additionally, the number of cells increases in a stepwise fashion, rather than exponentially, as most of the

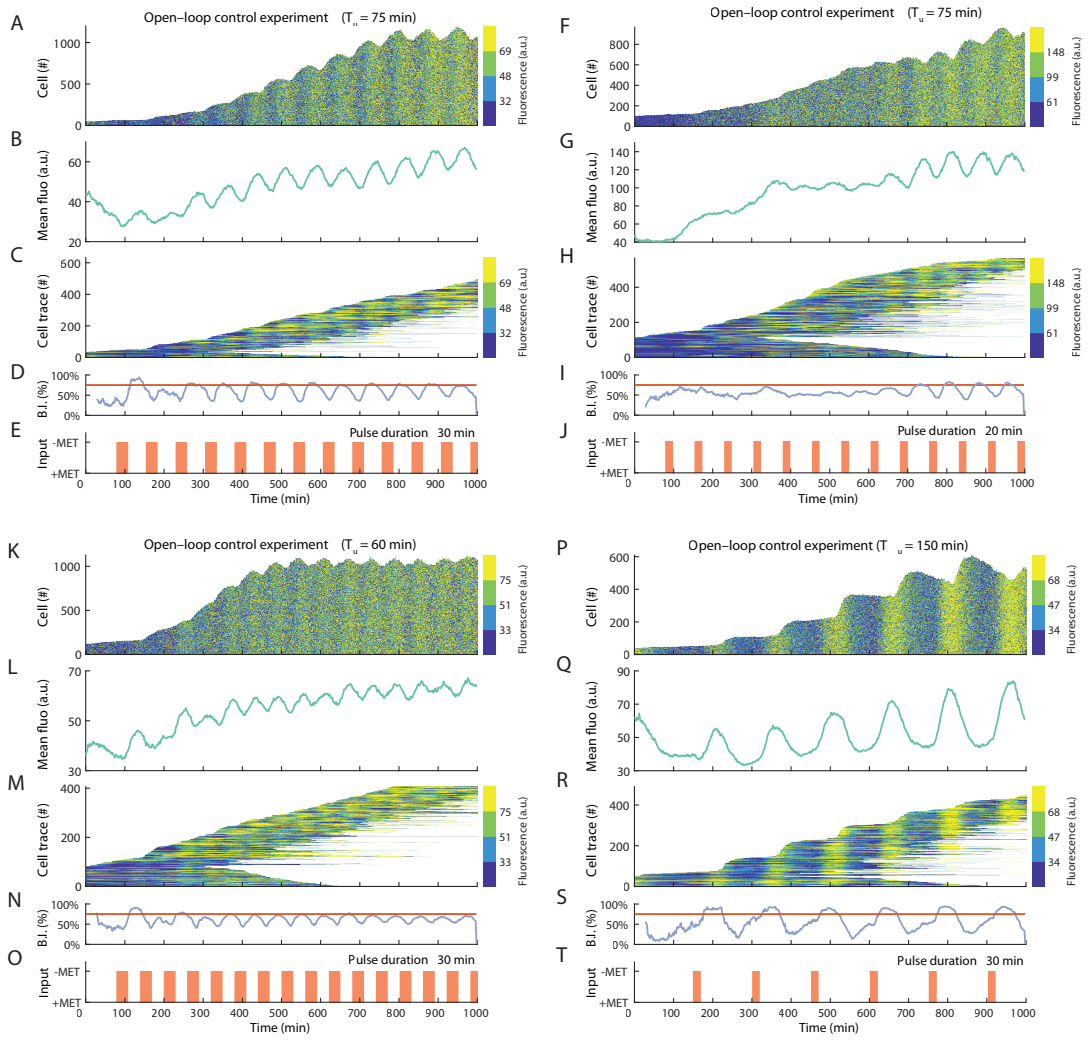

Figure 3.5: **Open-loop control of non-cycling strain.** Experimental validation of the open-loop control of non-cycling yeast strain cells with four different period-duration combination: $T_u = 75\,\text{min}$, $D_{-\text{Met}} = 30\,\text{min}$ (**A**-**E**); $T_u = 75\,\text{min}$, $D_{-\text{Met}} = 20\,\text{min}$ (**F**-**J**); $T_u = 60\,\text{min}$, $D_{-\text{Met}} = 30\,\text{min}$ (**K**-**O**); $T_u = 150\,\text{min}$, $D_{-\text{Met}} = 30\,\text{min}$ (**P**-**T**). (**A**, **F**, **K**, **P**) Distribution of the YFP fluorescence signals measured across the cell population over time. Fluorescence values are binned into 4 colours, corresponding to the quartiles, for clarity of visualisation. (**B**, **G**, **L**, **Q**) Time-series of the mean YFP fluorescence signal measured across the cell population. (**C**, **H**, **M**, **R**) Single-cell fluorescence traces over time. Each horizontal line corresponds to one cell. (**D**, **I**, **N**, **S**) Time-series of the budding index (blue) signal. The red line denotes the expected value of the budding index in the case of a totally desynchronised cell population. (**E**, **J**, **O**, **T**) Growth medium delivered to the cells as a function of time. +MET: methionine-rich medium, -MET: methionine-depleted medium.

cells bud together. Furthermore, the population-averaged YFP fluorescence intensity (Fig. 3.5B) displays an oscillatory behaviour, as cells become synchronised. A similar result was obtained by computing the budding index (Fig. 3.5D) from single-cell traces (Fig. 3.5C). However, just a shorter stimulation period ($T_u = 60\,\text{min}$) (Fig. 3.5K-O) or a shorter pulse duration ($D_{-Met} = 20\,\text{min}$) (Fig. 3.5F-J) causes a decrease in synchronisation. Indeed, in the first case ($D_{-Met} = 30\,\text{min}$ and $T_u = 60\,\text{min}$), cells' synchronisation is less effective as highlighted by the smaller oscillations in both population-averaged YFP fluorescence and $B.I.$. In the second case ($D_{-Met} = 20\,\text{min}$ and $T_u = 75\,\text{min}$), instead, the synchronisation takes considerably longer (700 min) as compared to longer pulses ($D_{-Met} = 30\,\text{min}$ and $T_u = 75\,\text{min}$). Note that, in this experiment, fluorescence values are much higher than in all the others. This is because this experiment was performed starting from cells in a plate and not from frozen cells (see Section B.2.4). This could be also the reason for the delay in the entrainment between the cell cycle and the external input, which starts at the fourth pulse to become effective at 700 min.

Finally, since this strain is halted in the G_1 phase in the absence of the external trigger, waiting for a longer time allows achieving a stronger synchronisation, as demonstrated by administering an input with $T_u = 150\,\text{min}$ with $D_{-Met} = 30\,\text{min}$ (Fig. 3.5P-T). However, the cost of this higher degree of synchronisation is the excessive growth in cell size.

3.5 Feedback control: the stop&go strategy

To overcome the drawbacks of open-loop control (e.g. the need to know beforehand the period and duration of stimulation), I implemented a control strategy based on the closed feedback loop paradigm. As illustrated in Fig. 3.6A, closed-loop feedback control relies on a sense and react paradigm, adapting the input to deliver in response to real-time measurements of the quantity to regulate. Specifically, yeast cells from a non-cycling strain population are grown in the microfluidics device while a microscope

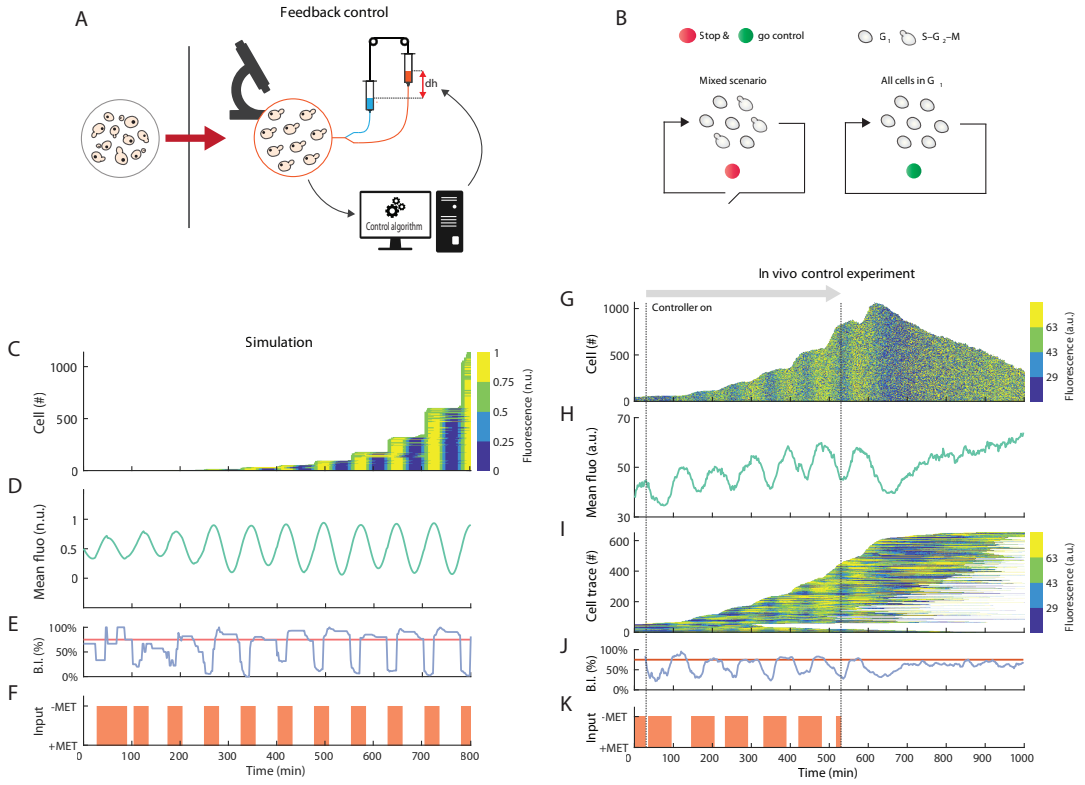

Figure 3.6: **Automatic feedback control of the non-cycling strain: the stop&go strategy.** (**A**) Automatic feedback control enables the synchronisation of the cell-cycle across a non-cycling strain population. (**B**) Schematisation of the stop&go strategy. The controller waits for cells to stop in the G1 phase and then restarts their cell cycle by removing methionine from the medium. (**C**-**F**) Numerical simulation of the stop&go control strategy. (**G**-**K**) Experimental implementation of the stop&go control strategy. An initial calibration phase of 30 min was required to set up the phase estimation algorithm. Dashed lines indicate the start and the end of the control experiment, after which cells are grown in methionine-rich medium. (**C**, **G**) Distribution of the YFP fluorescence signals measured across the cell population over time. Fluorescence values are binned into 4 colours, corresponding to the quartiles, for clarity of visualisation. (**D**, **H**) Time-series of the mean YFP fluorescence signal measured across the cell population. (**I**) Single-cell fluorescence traces over time. Each horizontal line corresponds to one cell. (**E**, **J**) Time-series of the budding index (blue) signal. The red line denotes the expected value of the budding index in the case of a totally desynchronised cell population. (**F**, **K**) Growth medium delivered to the cells as a function of time. +MET: methionine-rich medium, -MET: methionine-depleted medium.

acquires in real-time phase contrast and fluorescence images. A control algorithm, implemented in a computer, estimates the cell-cycle phase of each cell from fluorescent

data and decides the duration and the timing of the methionine starvation pulses to achieve the control objective (e.g. synchronisation of cell cycle across cells). Finally, a pair of syringes (Section 2.2) delivers the control input to the cells.

To design a closed-loop feedback control strategy to synchronise the cell cycle across the non-cycling yeast cells, I exploited the characteristics of this strain of being blocked in the G1 phase in methionine-rich medium (+MET) and to cycle upon its depletion ($-$MET). Specifically, at each sampling time the controller, which we named *stop&go*, evaluates the percentage of cells in the G_1 phase. If this percentage is higher than a fixed threshold, then the controller delivers an exogenous pulse of $-$MET of duration $D_{-Met} = 30\,\text{min}$, thus enabling the cell cycle to start in all G_1 phase cells, as depicted in Fig. 3.6B. The threshold value has to be chosen as a trade-off between the synchronisation level to achieve and the constrain on the cell growth.

To test the feasibility of the stop&go control strategy in achieving the synchronisation task, we used the dynamical model presented in Section 3.3 to carry out a numerical simulation with a threshold value set to 50%, whose results are shown in Fig. 3.6C-F. We performed the simulation starting with an initial population of $N_0 = 3$ homogeneous cells. The initial phases $\vartheta_{i,0}$ of individual cells were uniformly spaced in the interval $[0, 2\pi[$, while the initial volumes $V_{i,0}$ were set equal to the critical volume V_c, that is all the initial cells are assumed to be mother cells. The agent-based system was solved using the MATLAB `ode15s` solver. The total simulation lasts $t_f = 800$ min. Since we considered the same numerical parameters for each cell agent, the cell-to-cell variability across the cell population inherently arose from the cell division events. To mimic the dynamical behaviour of the experimental output, we transformed the single-cell phases ϑ_i in a fluorescent signal according to the CLN2_{ref} signal in Eq. 3.1. The code used to perform this simulation, developed by Giansimone Perrino, is available on *GitHub* (see Appendix B.4). Numerical results show that the stop&go controller can in principle synchronise the cell cycle across a population of cells, without any prior knowledge of the cell cycle duration and growth conditions. As expected for a synchronised popula-

tion, the simulated fluorescence signal in individual cells over time in Fig. 3.6C presents a clear vertical pattern and a step-wise increase in cell number. Equally, the population-averaged YFP fluorescence intensity in Fig. 3.6D and the *B.I.* in Fig. 3.6E present an oscillatory behaviour.

Encouraged by the numerical results, I performed a series of microfluidic experiments implementing the stop&go feedback control strategy with a threshold set to 50%. Specifically, cells were grown overnight in a methionine-depleted medium and thus were desynchronised at the beginning of the experiment. Moreover, an initial calibration phase of 30 min was required to set up the phase estimation algorithm; after that, the stop&go controller was activated for 500 min and then deactivated. The closed-loop stop&go control strategy was able to automatically synchronise the cell population as corroborated by the vertical pattern arising at both population (Fig. 3.6G; Fig. A.2A,F) and single-cell traces (Fig. 3.6I; Fig. A.2C,H) and by the step-wise population growth (Fig. 3.6G; Fig. A.2A,F). The synchronisation is also confirmed by the oscillating behaviour of the population-averaged YFP fluorescence (Fig. 3.6H; Fig. A.2B,G) and *B.I.* (Fig. 3.6J; Fig. A.2D,I) signals. Moreover, they also show how the synchronization is lost in one cell cycle when the controller is deactivated, in both methionine-rich (Fig. 3.6G-K; Fig. A.2F-J) and methionine-depleted (Fig. A.2A-E) conditions. Interestingly, when cells are left in a methionine-depleted medium, the cell number remains constant (Fig. A.2A) at a value dependent on the chamber size. Instead, when cells are left in the methionine-rich medium the cell number decrease (Fig. 3.6G; Fig. A.2F). This is because the cells are halted in the G_1 phase and continue to grow in volume throwing some of the cells out of the chamber.

The codes used to control the platform and to perform the feedback control experiments are available on *GitHub* (see Appendix B.4).

3.6 Robustness of stop&go control in perturbed conditions

One of the main advantages of the closed-loop feedback control strategy is that it can steer systems behaviour with robustness to perturbations and uncertainties. With the open-loop control, indeed, one needs to know beforehand the period and the duration of pulsatile input; however, changes in carbon source, temperature, or any other perturbation that alters the metabolic rate of the cell, will cause changes to the cell cycle duration, so that the chosen open-loop control input may no longer able to synchronise the cell population. To demonstrate the robustness of the simple stop&go control strategy, I performed a series of experiments perturbing cells by changing either the growth temperature or the carbon source.

When the cell growth temperature was set to 27 °C, cells slightly slow down their cell cycle period [116]. In this condition (Fig. 3.7), the closed-loop controller was still able to synchronise the cell population (Fig. 3.7F-J) with a similar performance as in the unperturbed case. Instead, the open-loop control ($D_{-Met} = 30$ min and $T_u = 75$ min) (Fig. 3.7A-E), although able to achieve synchronisation across the population, exhibits worse performances compared with the correspondent open-loop in nominal conditions ($T = 30$ °C, $D_{-Met} = 30$ min and $T_u = 75$ min) (Fig. 3.5A-E), as attested by the smaller oscillation in both population-averaged YFP fluorescence (Fig. 3.7B vs. Fig. 3.5B) and in $B.I.$ (Fig. 3.7D vs. Fig. 3.5D). Moreover, in temperature-perturbed condition, the open-loop controller needed more time to reach a stable synchronisation: while in nominal condition, it is achieved since the third input pulse; in perturbed condition, cells are stably synchronised and entrained with the external input only after the fifth pulse.

Next, I applied a stronger perturbation, growing cells in galactose (Fig. 3.8), which is known to slow down the cell cycle [117]. Particularly, cells were grown overnight in nominal condition, i.e. glucose (@2% w/v), and then switched in galactose (@2% w/v)

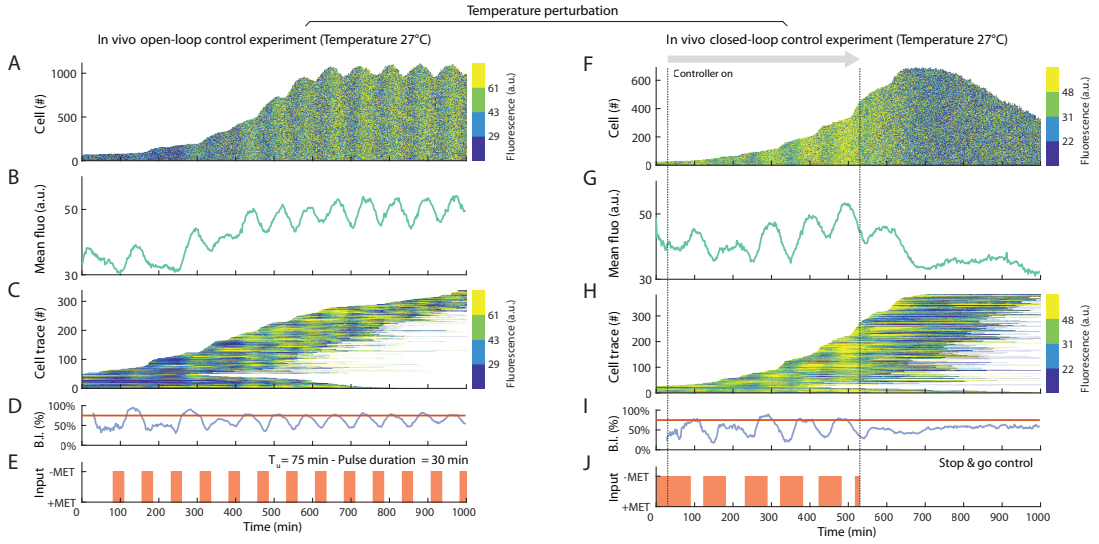

Figure 3.7: **Stop&go control is robust to temperature perturbation.** Temperature was set to 27 °C, rather than the nominal 30 °C, to assess the robustness of the open-loop (**A**-**E**) and closed-loop control (**F**-**J**) strategies in perturbed environmental conditions. (**A**, **F**) Distribution of the YFP fluorescence signals measured across the cell population over time. Fluorescence values are binned into 4 colours, corresponding to the quartiles, for clarity of visualisation. (**B**, **G**) Time-series of the mean YFP fluorescence signal measured across the cell population. (**C**, **H**) Single-cell fluorescence traces over time. Each horizontal line corresponds to one cell. (**D**, **I**) Time-series of the budding index (blue) signal. The red line denotes the expected value of the budding index in the case of a totally desynchronised cell population. (**E**, **J**) Growth medium delivered to the cells as a function of time. +MET: methionine-rich medium, -MET: methionine-depleted medium.

when loaded into the microfluidic device. In these conditions, the open-loop control (Fig. 3.8A-E) completely fails to achieve the synchronisation task; while the stop&go control (Fig. 3.8F-J) is still able to synchronise the population with comparable performances to the case of nominal conditions (Fig. 3.6G-K). Interestingly, cells grown in galactose failed to cycle for the first 300 min. This is in line with the results Nguyen-Huu *et al.* [117], who demonstrate that this delay is due to the diauxic shift.

Finally, the extent of synchronisation was quantified for each experiment and reported in Fig. 3.9. Specifically, I measured two different indices: (i) the time-average of the mean phase coherence (R); and (ii) the time-average of the mean cell radius. Both of them are computed between 330 and 530 min (the last 200 min of controller function-

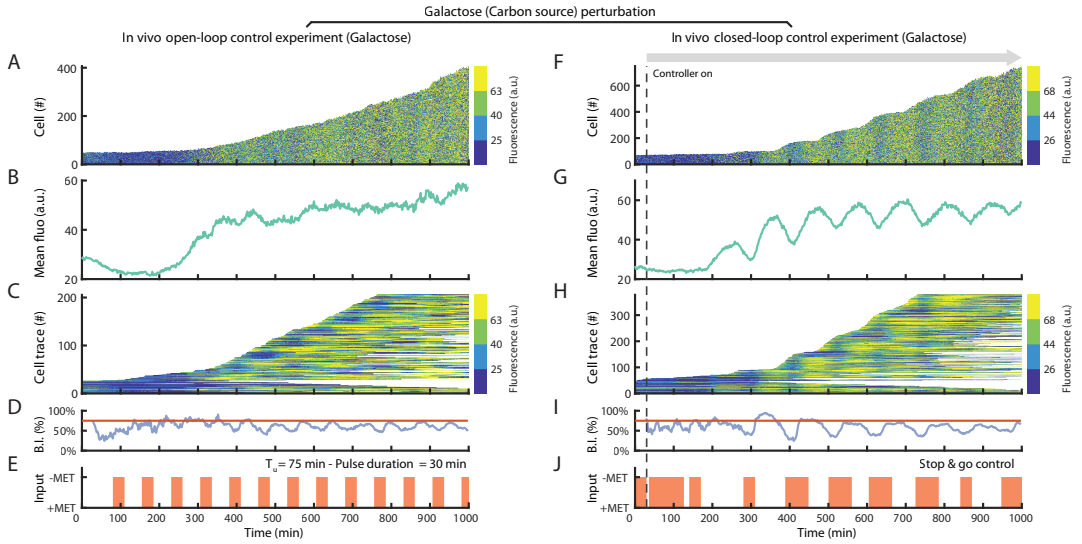

Figure 3.8: **Stop&go control is robust to carbon source perturbation.** Cells were grown in galactose (@2% w/v), rather than in glucose (@2% w/v), to assess the robustness of the open-loop (**A**-**E**) and closed-loop control (**F**-**J**) strategies in perturbed environmental conditions. (**A**, **F**) Distribution of the YFP fluorescence signals measured across the cell population over time. Fluorescence values are binned into 4 colours, corresponding to the quartiles, for clarity of visualisation. (**B**, **G**) Time-series of the mean YFP fluorescence signal measured across the cell population. (**C**, **H**) Single-cell fluorescence traces over time. Each horizontal line corresponds to one cell. (**D**, **I**) Time-series of the budding index (blue) signal. The red line denotes the expected value of the budding index in the case of a totally desynchronised cell population. (**E**, **J**) Growth medium delivered to the cells as a function of time. +MET: methionine-rich medium, -MET: methionine-depleted medium.

ing). The mean phase coherence $R \in [0,1]$ is defined as the magnitude of the Kuramoto order parameter [112]:

$$R(t) = \left| \frac{1}{N(t)} \sum_{i=1}^{N(t)} e^{j\vartheta_i(t)} \right|, \tag{3.11}$$

where $N(t)$ is the time-varying number of cells, while ϑ_i is the phase of the i-th cell, both evaluated at time t. When R is equal to 1, all cells are synchronised. Conversely, when R is equal to 0, cells are desynchronised. The time-average of the mean cell radius, estimated as explained in Section 2.3.1, was evaluated to consider that a perfect synchronisation can be achieved waiting enough time but at the cost of excessive volume growth. This quantitative analysis (Fig. 3.9) confirmed that the closed-loop feed-

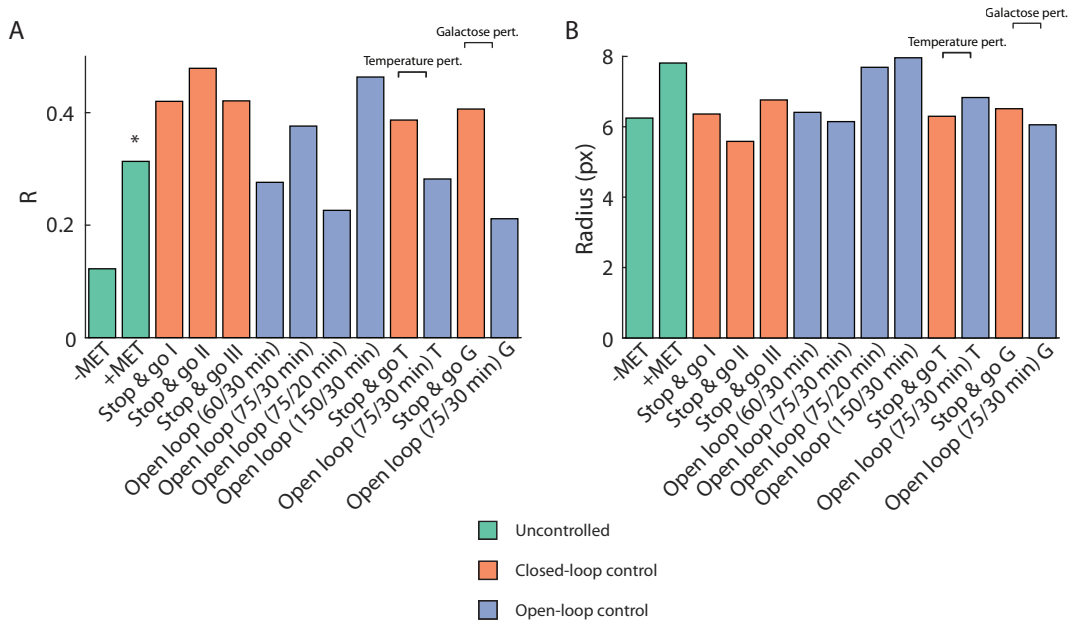

Figure 3.9: **Quantification of cell cycle synchronisation and cell size** (**A**) Time-average of the mean phase coherence R for all the experiments performed. The time-average was computed between 330 and 530 min. (**B**) Time-average of the mean cell radius. T: temperature shifted to 27 °C. G: cells grown in Galactose. *: not reliable, because of the difficulties in image analysis and phase estimation in +MET experiment.

back strategy, even if very simple, is more effective in achieving the synchronisation keeping the cell volume in physiological conditions, particularly in the face of new and unexpected environmental perturbations. Note that the synchronisation index for the uncontrolled experiment performed in presence of methionine is higher than expected (even higher than some open-loop control experiments). This is because the phase estimation algorithm failed for the bad conditions of these cells. This is confirmed by looking at the population-averaged YFP fluorescence in Fig. 3.3B, which exhibits a flat profile.

The codes to perform the quantitative analysis here described are available on *GitHub* (see Appendix B.4).

Chapter 4

Quantitative characterization and modelling of the nuclear shuttling dynamics of the Transcription Factor EB (TFEB).

In this Chapter, I will describe how microfluidics can be used to investigate and model the dynamics of regulatory and signalling networks in the cell by presenting the mTOR pathway as a study case. mTOR signalling is one of the most studied pathways in mammalian cells as it is involved in cell metabolism, growth, proliferation, and survival in the presence of nutrients. It involves a large number of proteins and organelles through both protein-protein interactions and transcriptional regulation. Despite the importance of this pathway in cellular homeostasis, very little is known about its dynamics. By means of a microfluidic-based experimental platform to grow and probe mammalian cells, I have quantitatively measured the nuclear shuttling dynamics of the transcription factor (TFEB), whose nuclear localisation is controlled by the mTOR complex 1 (mTORC1) activity in single-cells. The observed dynamics are very complex and I put forward a set of possible mechanisms controlling this behaviour.

The experiments and the model presented in this Chapter were designed and implemented in collaboration with Iacopo Ruolo, a Ph.D. student of XXXV cycle of the Ph.D. program in Industrial Product and Process Engineering.

4.1 TFEB and the mTOR pathway

Cell metabolism is controlled by complex networks of genes, proteins, and metabolites that sense the cellular environment and regulate the appropriate responses. The mammalian target of rapamycin (mTOR) lies at the heart of many major signalling pathways and plays a key role as a central regulator of cell metabolism, growth, proliferation, and survival [118–120]. The mTOR pathway integrates both intra- and extracellular signals about the availability of energy and nutrients to coordinate the synthesis or breakdown of new cellular components. Since this pathway is deregulated in a number of common human diseases, such as cancer, obesity, and type 2 diabetes [120], studies about mTOR mechanisms of action are attracting an increasing number of scientists and the mTOR inhibitors are being investigated in a growing number of pathological settings, first of all for treatment of solid tumors [121].

Among others, mTOR regulates autophagy, which is a self-degradative process important for organelle degradation and protein turnover. During nutrient deficiency, autophagy is used by the cell to recycle cytoplasmic components, damaged proteins, and entire organelles to provide biological material to sustain anabolic processes [119].

The mTOR pathway

The mTOR protein is a 289 kDa serine-threonine kinase that belongs to the phosphoinositide 3-kinase (PI3K)-related kinase family. The mTOR domain structure, shown in Fig. 4.1A, consists of six functional areas: (i) the HEAT motifs, involved in protein-protein interaction; (ii) the focal adhesion targeting (FAT) domain and (iii) the C-terminal focal adhesion targeting (FATC) domain, needed to form a spatial structure

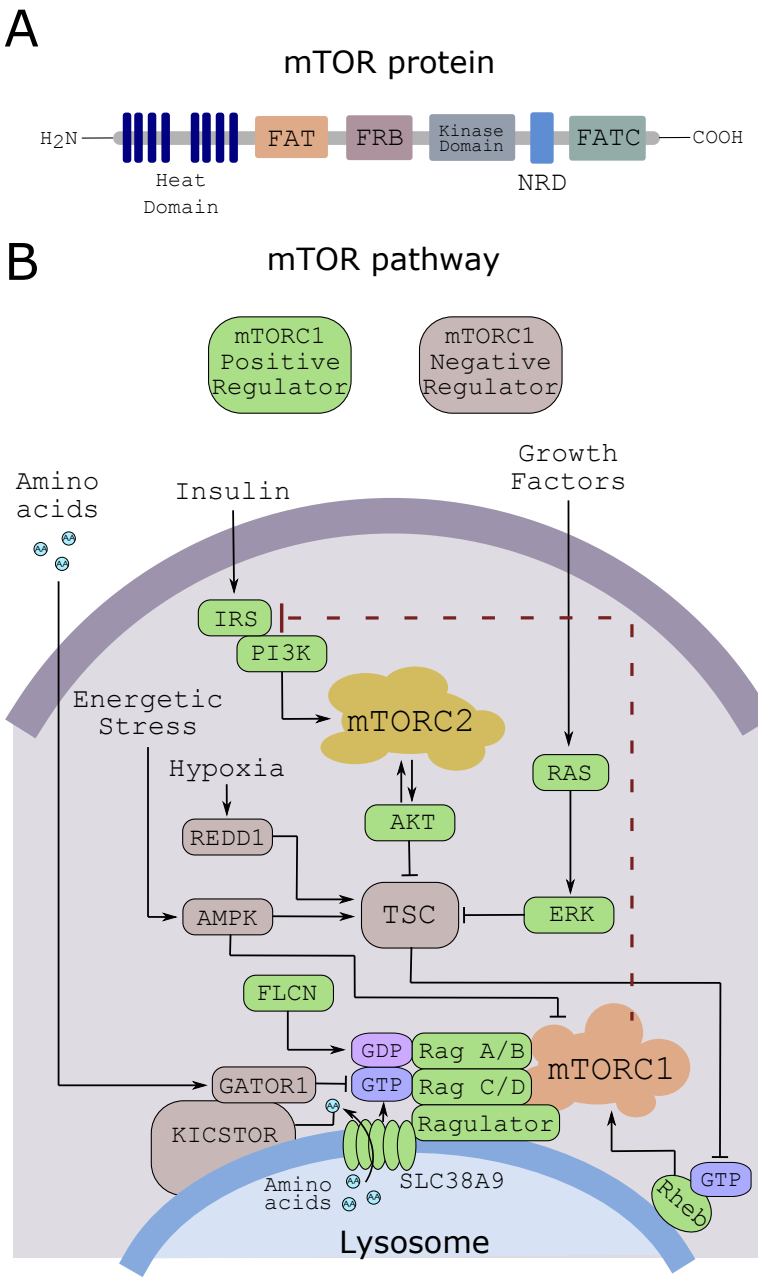

Figure 4.1: **The mTOR pathway.** (**A**) Schematic structure of the mTOR protein. (**B**) A simplified version of the mTOR pathway. Adapted from [122]

which can expose the mTOR catalytic domain; (iv) the FKBP12 rapamycin binding (FRB) domain; (v) the kinase (KIN) domain, that is the mTOR's catalytic domain where ATP and the substrates to be phosphorylated bind; and (vi) the NRD domain, contained in the KIN domain [120]. In mammals, it constitutes the catalytic subunit of two distinct complexes known as mTOR complex 1 (mTORC1) and mTORC2. They

are distinguished from each other by the other proteins that form the complexes and by their unique substrates and functions. Particularly, mTORC1 primarily controls cell growth and proliferation by promoting biosynthesis of proteins, lipids, and organelles, and by limiting autophagy. Instead, mTORC2 participates in the control of cell survival and proliferation [118, 120].

While little is known about mTORC2 signalling, mTORC1 activity is toggled by the cell in response to nutrient oscillation and it is switched on when energy, growth factors, and macromolecular building blocks - amino acids and nucleotides - are plentiful [118–120]. To monitor and respond to these stimuli, a mTORC1 recruitment complex and a mTORC1 activator colocalise acting as an "AND" gate, so that the mTORC1 can only be activated when it is recruited on the lysosomal surface where it interacts with its activator [119]. The input of the first side of the AND gate are growth factors and cellular stress signals that activate the small GTPase Rheb (RAS homologous enriched in the brain) which directly stimulates mTOR kinase activity when it is bound to GTP [123]. Instead, the other side of the AND gate is regulated by nutrients through the heterodimeric Rag GTPases that localise mTORC1 on the lysosomal membrane allowing its interaction with Rheb (Fig. 4.1B) [124, 125].

The main Rheb regulator is the tuberous sclerosis complex (TSC), which is a heterodimer that comprises TSC1 and TSC2. It acts as a GTPase-activating protein (GAP) for Rheb and therefore serves as a negative regulator of mTORC1 signalling [126]. Several patterns converge on TSC. Upon insulin stimulation, insulin and/or insulin-like growth factor-1 (IGF-1) stimulate PI3K signalling, which, through mTORC2, recruits and activates AKT that phosphorylates at multiple sites to dissociate TSC from the lysosomal surface and relieve inhibition of Rheb and mTORC1 [127]. To tune the extent and duration of mTORC1 activation and restore TSC regulation after this stimulus, the mTORC1 substrate S6K1 directly phosphorylates insulin receptor substrate 1 (IRS-1) as part of a negative feedback loop, blocking further insulin-mediated activation of the PI3K–Akt pathway [128]. In addition, TSC is subject to inhibitory phosphorylation

from ERK, a downstream substrate of the Ras receptor tyrosine kinase signalling pathway [129]. Because mutations that activate the Ras and PI3K–Akt pathways occur in many cancers, TSC regulation of mTORC1 is often lost in oncogenic contexts, resulting in constitutive mTORC1 activity even in the absence of appropriate growth factor signals [120]. The TSC axis is activated also under other kinds of stress conditions. Under energetic stress, the cell can consume the ATP storage, triggering the AMP-activated protein kinase (AMPK) complex that inhibits mTORC1 both indirectly, by activating the TSC axis, and directly, by phosphorylating Raptor, one of the main component of mTORC1 [130, 131]. Finally, also hypoxia can activate the TCS complex through REDD1 (regulated in development and DNA damage responses 1), a small protein with a very short half-life [132, 133].

The other components of the AND gate in mTORC1 regulation are the RAGs. They are obligate heterodimers, configured such that RagA or RagB is bound to RagC or RagD. Recruitment of mTORC1 to the lysosomal surface depends on the Rag nucleotide-loading state, which is tightly regulated by numerous mechanisms, including interactions within the Rag heterodimers themselves [134]. Particularly, the Rags can be found in one of two stable conformations: an "on" state, in which RagA/B is bound to GTP and RagC/D to GDP; and an "off" state, in which the reverse is true. These stable nucleotide-loading states are maintained by intersubunit crosstalk between the Rags, but they can be modulated by the amino acid and nutrient status through a series of upstream factors [120]. First of all, Ragulator, a pentameric complex containing Lamtor1–Lamtor5, affects the nucleotide loading of RagC or RagD through a noncanonical guanine nucleotide exchange factor (GEF) mechanism, in which GTP release is accelerated. Moreover, Ragulator anchors the Rags on the lysosome surface [135]. Another complex acting on the Rags is GAP activity towards the Rags (GATOR1). When cytosolic amino acid levels fall, GATOR1 hydrolyses the GTP bound to RagA/B and inhibits the mTORC1 pathway [136]. In turn, GATOR1 is itself regulated by other upstream factors. Among them, the large KICSTOR complex localise GATOR1 on the

lysosome and is required for cellular sensitivity to amino acid deprivation [137]. Two additional complexes regulate the Rags. The first is the folliculin complex (FLCN with FNIP1 or FNIP2) that has GAP activity for RagC and/or RagD. Amino acids regulate the localization of the Folliculin complex to the lysosome [138]. The second is an arginine sensor, SLC38A9, that monitors amino acid levels inside the lysosomal lumen and defines the lysosomal branch of the nutrient-sensing machinery. SLC38A9 resides on the lysosomal membrane and transports neutral amino acids out of the organelle in an arginine-gated fashion. This efflux activity may enable the products of autophagic protein degradation to reactivate the mTORC1 pathway after prolonged starvation. Specifically, lysosomal arginine frees the N terminus domain of SLC38A9 that collaborates with Ragulator to push the Rags into the active state activating mTORC1 [139].

In response to these signals, mTORC1 phosphorylates its substrates to balance cellular resources by regulating the protein production and autophagic breakdown of cellular components. Specifically, in full growth condition, mTORC1 promotes protein synthesis by phosphorylating the eukaryotic initiation factor 4E-binding proteins (4E-BPs) and p70 S6 kinase 1 (S6K1) [140]. In its unphosphorylated state, 4E-BP1 suppresses translation by binding and sequestering eukaryotic translation initiation factor 4E (eIF4E), an essential component of the eIF4F cap-binding complex. Upon phosphorylation by mTORC1, 4E-BP1 releases eIF4E and enhances $5'$ cap-dependent translation of mRNAs. At the same time, mTORC1 phosphorylates S6K1 which subsequently phosphorylates the ribosomal protein S6, a component of the 40S subunit. More directly, S6K1 and mTORC1 upregulate transcription of rRNA, the dominant component of newly-assembled ribosomes [141]. On the other hand, mTORC1 controls the autophagic flux through the inhibition by direct phosphorylation of proteins required for the initiation of autophagosome formation such as Unc-51 like autophagy activating kinase (ULK) 1 and ULK2, and ATG13 [142], and of the Transcription Factor EB (TFEB) and the related transcription factor E3 (TFE3), master regulators of a transcriptional program promoting lysosomal biogenesis and autophagic flux. Therefore, when mTORC1

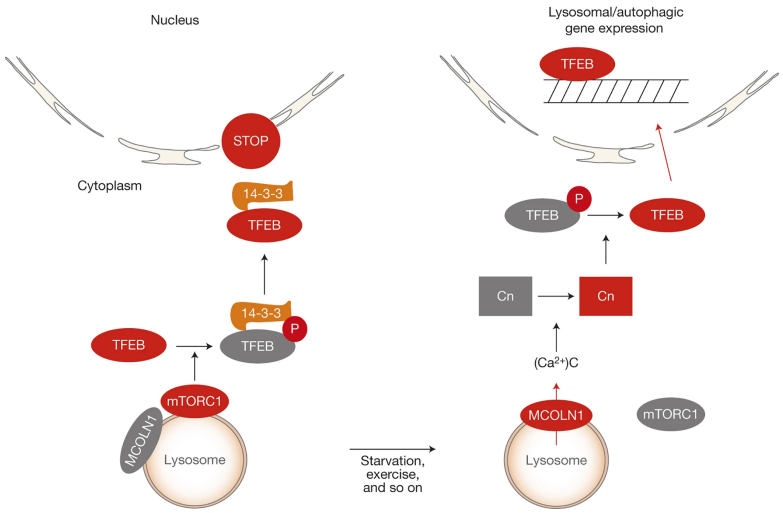

Figure 4.2: **TFEB activation in response to stress.** Under normal fed conditions, TFEB is phosphorylated by mTORC1 and is sequestered in the cytoplasm through binding with 14-3-3. In stress conditions, TFEB is dephosphorylated by calcineurin and can freely translocate to the nucleus where it transcriptionally activates the lysosomal/autophagic pathway. From [145]

is inhibited by nutrient deprivation, autophagosome initiation is restored and TFEB and TFE3 translocate to the nucleus to active their transcriptiona programs [143, 144].

TFEB regulation

The activity of TFEB is strictly regulated through post-translational modifications, protein-protein interactions, and spatial organization, as shown in Fig. 4.2. In resting cells, under nutrient-rich conditions, TFEB is directly phosphorylated by mTORC1 and localised in the cytoplasm and thus inactive. Upon starvation or under conditions of lysosomal dysfunction, TFEB rapidly translocates into the nucleus and activates the transcription of its target genes.

TFEB localisation and, consequently, its activity are regulated via protein phosphorylation. Despite the presence of at least ten different phosphorylation sites [146], three of them have been found to be essential for TFEB localisation. Serine residues S142 and S138 are located adjacent to the TFEB nuclear export signal (NES) and are, then, implicated in TFEB nuclear export, probably by regulating the access of the ex-

portin chromosomal maintenance 1 (CRM1) to the hydrophobic export signal, or by affecting the retention of TFEB to a nuclear anchor [122, 147]. Instead, S211 serves as a recognition site for TFEB binding to the chaperon 14–3–3 and cytosolic retention, probably by masking its nuclear localization signal (NLS). Nutrient availability regulates TFEB nucleo-cytoplasmic shuttling through hierarchical phosphorylation of these serine residues mainly by mTORC1 [147]. This mechanism ensures that only a fully phosphorylated TFEB is completely cytosolic and inactive, indicating that nutrient levels finely control TFEB subcellular localization via modulation of its shuttling kinetics. mTORC1 and extracellular signal-regulated kinase 2 (ERK2, also known as MAPK1) are the main protein kinases known to phosphorylate TFEB under nutrient-rich conditions in most cell types. Despite S142 is a site for both ERK- and mTOR-mediated phosphorylation, whereas S138 has been proposed as a GSK3β-phosphorylated site [122], it has been shown that phosphorylation on both S142 and S138 entirely depends on mTOR activity [147], suggesting that mTOR-mediated phosphorylation is the predominant mechanism regulating TFEB subcellular localization. Indeed, the phosphorylation of TFEB is strictly dependent on the amino acid-mediated activation of Rags but is insensitive to Rheb activity induced by growth factors [148, 149].

In response to amino acid limitation, mTORC1 is released from the lysosomal membrane and becomes inactive preventing *de novo* phosphorylation of TFEB (Fig. 4.2.). Interestingly, nutrient deprivation concomitantly induces the release of lysosomal Ca^{2+} through the Ca^{2+} channel mucolipin 1 (MCOLN1); this activates the phosphatase calcineurin, which in turn dephosphorylates TFEB and promotes its nuclear translocation (Fig. 4.2) [145].

TFEB has been shown to directly bind to DNA regulatory sites named "coordinated lysosomal expression and regulation" (CLEAR) motifis, thereby promoting the expression of a set of genes that contains the CLEAR regulatory motif in their proximal promoter. Consistent with its role as a modulator of the CLEAR network genes, TFEB positively regulates the expression of lysosomal genes and induces an increase

in the number of lysosomes, thus promoting the ability of cells to degrade lysosomal substrates [150]. Moreover, TFEB orchestrates the expression of a other genes participating to increase lysosomal exocytosis and the autophagic flux [151, 152].

By modulating the processes of lysosomal biogenesis, autophagy, and lysosomal exocytosis, TFEB coordinates a transcriptional program able to control the main cellular degradative pathways and to promote intracellular clearance. Intriguingly, many factors that regulate TFEB activity (i.e. the Ca^{2+} channel MCOLN1, the lysosomal 'platform' itself, and RagD) are themselves transcriptionally regulated by TFEB, providing evidence that lysosomal adaptation to environmental changes is a self-sustaining response that is regulated by multiple feedback loops [148, 153]. In addition, TFEB activation also promotes its own transcription, which represents an additional feedback loop that further sustains lysosomal signalling and function [153].

In addition to promoting lysosome biogenesis in response to amino acid limitation, TFEB can also enhance the integrated stress response (ISR) and acts as a nexus for nutrient sensing and resolution of any supply-demand disequilibrium. Indeed, amino acid starvation leads to repression of cap-dependent translation through the ISR pathway, thus decreasing global protein synthesis in the cell. However, as a transcription factor, to regulate the autophagic flux, TFEB requires protein synthesis, thus conflicting with the repression of general translation. To this end, TFEB fine-tunes protein synthesis during starvation by transcriptionally regulating GADD34 allowing translation of the starvation-induced transcriptional program to occur [154].

4.2 Pharmacological mTOR inhibition

Since the mTOR pathway is deregulated in many pathological conditions, including cancer and neurodegeneative disease, several pharmacological inhibitors of its activity are being developed. The chemical inhibitors of mTOR can be divided into three generations [156]: the first generation, also known as allosteric inhibitors, is formed by

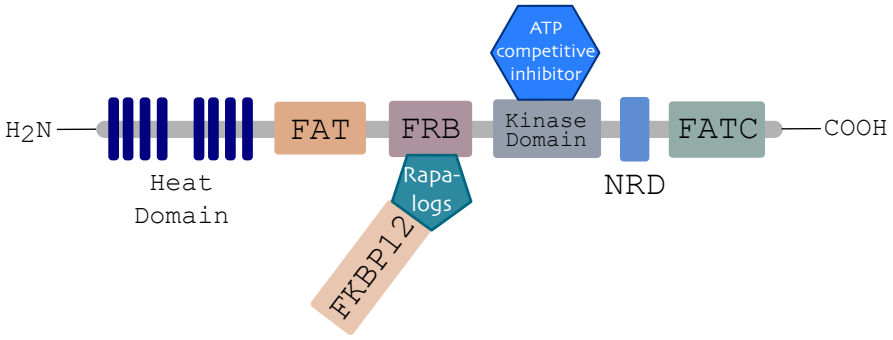

Figure 4.3: **mTOR inhibitors.** Adapted from [155]

naturally occuring compounds such as Rapamycin and other rapalogs; the second generation, known as ATP-competitive inhibitors, consists of synthetic small molecules that targets the catalytic site of the enzyme; while the third generation, known as rapalink, have a dual mechanism of action comprising acting both as rapalogs and inhibitors of the catalytic site [156] (Fig. 4.3).

The first generation of mTOR inhibitors: the rapalogs

Rapamycin is the prototype of the first generation of mTOR inhibitors [121]. It is a macrocyclic polyketide discovered as an antifungal agent. It functions as a molecular glue by binding FK506-binding protein-12 (FKBP12), a small cytosolic protein, allowing it to interact with mTOR to form a ternary complex [157]. The rapamycin-FKBP12 dimer binds to mTOR in the FRB region that is outside of the KIN domain [121]. As such, the binding itself does not inhibit the kinase activity of mTOR, but probably interferes with the association of the kinase with its substrates.

The rapalogs, as suggested by the name, are rapamycin analogs. Indeed, rapamycin bioavailability is affected by its poorly water solubility, which has led to a non exploitation of the drug in cancer therapy, despite its anti-cancer activity was well documented [121]. Because the drug requires two binding sites for FKBP12 and mTOR, it is poorly modifiable. Thus all the rapalogs are created by replacing the hydrogen at C-40-O position with different moieties [121].

Originally, mTORC2 was defined rapamycin insensitive, since acute exposure to the drug did not affect its activity. However, it was shown that rapalogs can to suppress mTOR activity in both mTORC1 and mTORC2, but at very different concentrations [158]. Moreover, low doses of rapalogs, inhibiting mTORC1, trigger a feedback mechanism that lead to an IGF1-dependent mTORC2 activation through PI3K, increasing also the Akt phosphorylation [158, 159]. This is likely one of the reason why rapalogs activity as monotherapies in cancer treatment did not appear as promising as initially expected.

Since rapamycin and rapalogs do not interfere with mTOR kinase domain, their inhibition is not entirely effective. Indeed, different mTOR targets not responding to rapamycin treatments were identified, and among them there is TFEB [151]. Therefore, since, in this study, TFEB localisation was used as a proxy of mTOR activity, the first generation of mTOR inhibitors were not analysed.

The second generation of mTOR inhibitors: the ATP-competitive inhibitors

The problems linked with rapamycin and rapalogs use have led to the development of new drugs able to inhibit mTOR by a different mechanism of action. Particularly, small molecules that compete for the binding pocket with ATP (from which the name of this class) should be able to inhibit mTOR both in mTORC1 and mTORC2 and, consequently, block the mTORC2 dependent activation of Akt [155].

Because of the sequence similarity of mTOR with PI3K, many ATP competitive PI3K inhibitors were found to display various degrees of mTOR inhibitory activity. These inhibitors were often used as prototype compounds for the PI3K/mTOR dual inhibitors [155]. These dual PI3K/mTOR modulators contain "classical hinge kinase binders" and docking studies performed with homology modelling suggest that the interactions mediated by the core scaffold are similar to the ones described for other ATP-competitive modulators (e.g., canonical H-bond interactions with residues in the hinge region of the lipid kinase) [160]. These dual PI3K/mTOR modulators have

demonstrated significant, concentration-dependent cell growth inhibition and induction of apoptosis in a variety of tumor cancer cells. However, while simultaneously targeting PI3K and mTOR circumvents the limitation of rapalogs in blocking PI3K/AKT signalling, the potential toxicity associated with this type of inhibitors presents a big concern, owing to the diverse functions of different isoforms of PI3K. It is generally believed that inhibitors more selective for mTOR may be better tolerated than the dual inhibitors [121].

Torin1 is a pyridinone-quinoline compound [161] that utilizes a pharmacophore space to achieve specificity [155]. This space consists in a channel that runs from the bottom surface of mTOR inward toward the ATP and substrate pockets. The longitudinal axis of ATP is perpendicular to the axis of this channel. Torin1 has a ring roughly perpendicular to this axis. Torin1 inhibits both mTOR-containing complexes with IC_{50} values between 2 and 10 nM [161] and shows an 800-fold selectivity versus PI3K [162].

The AstraZeneca AZD8055 has been one of the first optimized ATP-competitive mTOR inhibitors to enter clinical trials [160]. It belongs to the pyrido[2,3-*d*]pyrimidines class. It displays a good selectivity for mTOR ($IC_{50} = 0.8$ nM) inhibiting the rapamycin-resistant phosphorylations [155] and shows excellent selectivity ($\sim 1,000$-fold) against PI3K [163].

4.3 Probing and modelling of TFEB nuclear translocation dynamics by microfluidics

Despite the growing number of studies regarding the mTOR pathway and TFEB translocation, very little is known about their dynamics. Therefore, we set to quantitatively measure and model TFEB translocation dynamics to the nucleus following mTOR inhibition and activation.

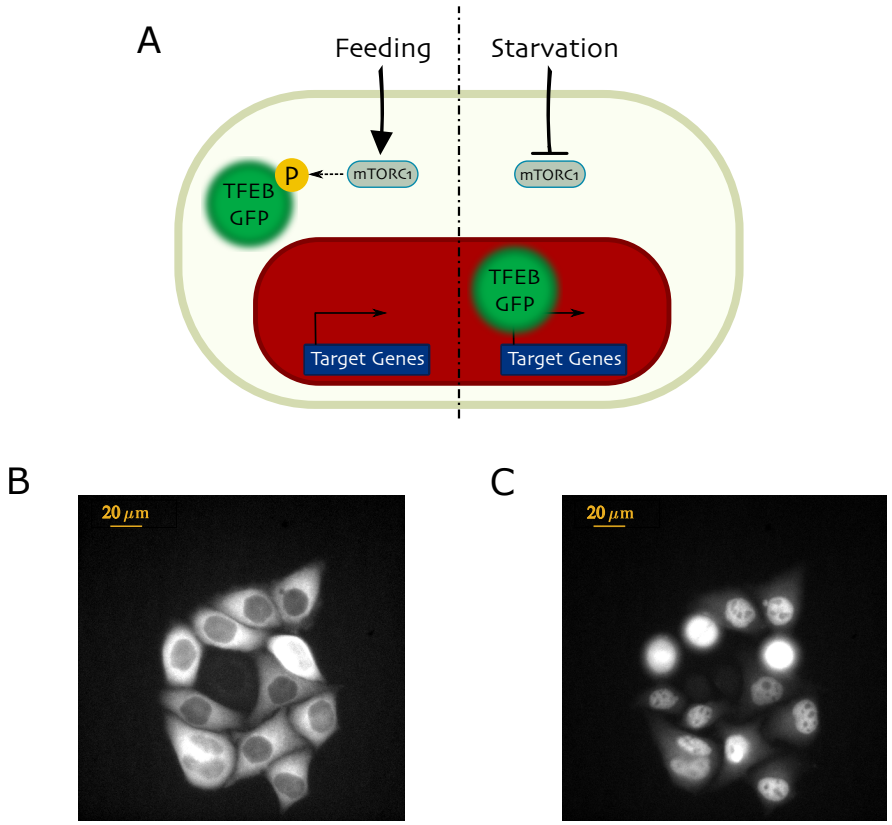

Figure 4.4: **Experimental model: HeLa TFEB-GFP monoclonal cell line.** (**A**) Schematic representation of TFEB nuclear translocation. In fed conditions, the fusion protein TFEB-GFP is phosphorylated by mTORC1 and trapped in the cytoplasm. In starvation condition, mTORC1 is inhibited, TFEB-GFP is no longer phosphorylated and it is able to translocate into the nucleus. (**B**, **C**) Representative fluorescent images in fed (**B**) or starvation (**C**) conditions.

4.3.1 TFEB nuclear shuttling in starvation conditions

To study the dynamics of TFEB nuclear shuttling, I decided to use a human HeLa cell line overexpressing the fusion protein TFEB-GFP, already used in our experimental set-up with which we controlled TFEB subcellular localisation [40]. This cell line is schematically represented in Fig. 4.4A, and it was firstly developed in Settembre *et al.* [143] and, then, modified in our lab by adding a nuclear mCherry protein to facilitate image processing [40]. The fusion protein TFEB-GFP enables to follow the protein localisation of TFEB in response to the external stimulus. Indeed, in nutrient-rich conditions, mTORC1 phosphorylates TFEB thus trapping it into the cytosol, as shown in

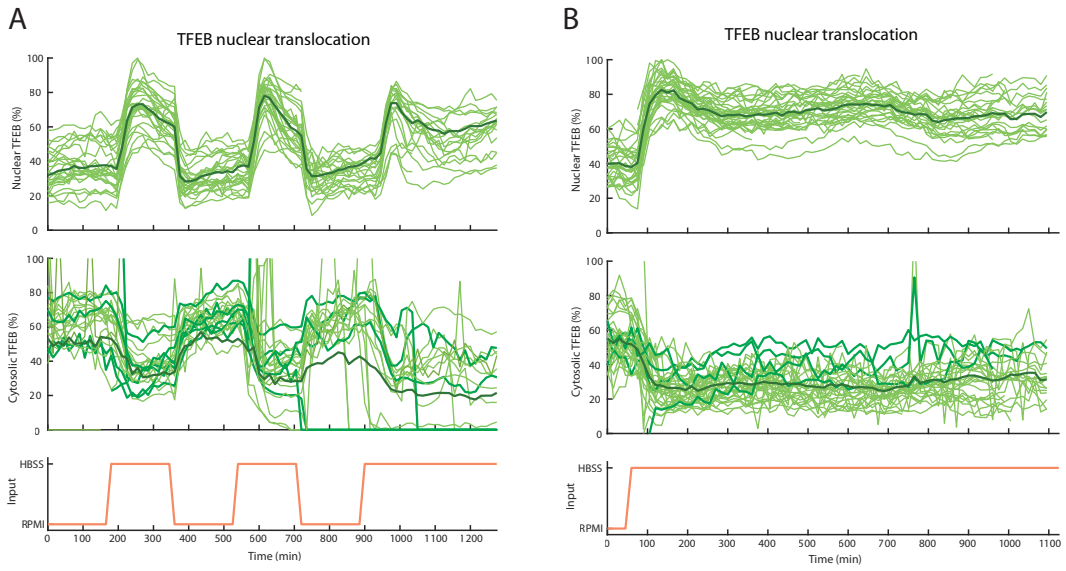

Figure 4.5: **Experimental measurements of TFEB translocation in starvation conditions.** Each figure shows single cell traces of nuclear TFEB fluorescence (shown in the upper plot) measured in the microfluidics platform following the correspondent input (shown in the lower plot): a train of starvation pulses (**A**) or a single starvation stimulus (**B**). The average of the single-cell traces is highlighted with a solid line in the upper plot. In the middle plot, instead, traces of cytosolic TFEB fluorescence are shown. The darkest and bold line is the average of the single-cell traces, while the bold traces are single cells in which the cytosolic relocalisation is visible.

Fig. 4.4B. In the absence of amino-acids (starvation), mTORC1 is inhibited and TFEB is free to translocate into the nucleus as shown in Fig. 4.4C.

To characterise this cells line, I performed a series of preliminary experiments by taking advantages of the experimental platform described in Chapter 2. Cells were grown in the mammalian microfluidic device allowing the precise regulation of their micro-environment, while fluorescence microscopy followed by image analysis enable quantitative measurement of TFEB cytoplasmic and nuclear localisation. Cells were exposed to a train of alternating pulses of nutrient-rich medium (RPMI) and amino-acid starvation (HBSS), as shown in Fig. 4.5A. Single-cell nuclear and total fluorescence was measured with an off-line image analysis algorithm described in Section 2.3.2. Then, the total fluorescence was filtered with a moving average filter with a window

of 20 samples (that corresponds to 300 min). Finally, the nuclear fluorescence was normalized with respect to the filtered version of the total fluorescence to obtain the percentage of nuclear TFEB over time. In the upper plot of Fig. 4.5A, single-cell signals are shown with thin green lines while their average is shown with a bold green one. These results indicate that cells were able to respond to each pulse exhibiting always the same dynamics. Interestingly, after a very fast nuclear translocation in response to starvation, a slower and smaller cytoplasmic relocalisation occurs, which we termed an "overshoot"; a similar but much smaller effect is present also when switching from starvation to nutrient-rich medium. When treated with a single starvation pulse, as shown in Fig. 4.5B, cells exhibit the same behaviour: a slower relocalisation that follows the fast translocation in response to starvation, followed by constant level (about the 70% of nuclear TFEB in the average signal), which is maintained over time, despite the stress being still present. The appearence of the overshoot was quite unexpected, although a subsequent analysis of the literature revealed that a similar phenomenon was observed by Zapata *et al.* [164]. The authors suggested that the rapid rheostatic response, mediated by mTOR, allows the cell to quickly adapt to metabolic changes, while the long-term, mTOR-independent homeostatic response controls the magnitude and duration of TFEB activation, and presumably limits excessive autophagy. However no mechanism was put forward to explain the origin of this dynamic behaviour.

4.3.2 A dynamical model for TFEB nuclear translocation

To analyse and better understand the mechanisms that cause the overshoot observed in experimental data, we derived a dynamical model based on the current literature. Specifically, we considered a multi-compartmental model [165] shown in Fig. 4.6A. The model has two distinct compartments, nucleus and cytoplasm, within which de/phosphorylation reactions occur. To consider the transport between compartments, two irreversible reactions were added. We considered four species for TFEB, according to lo-

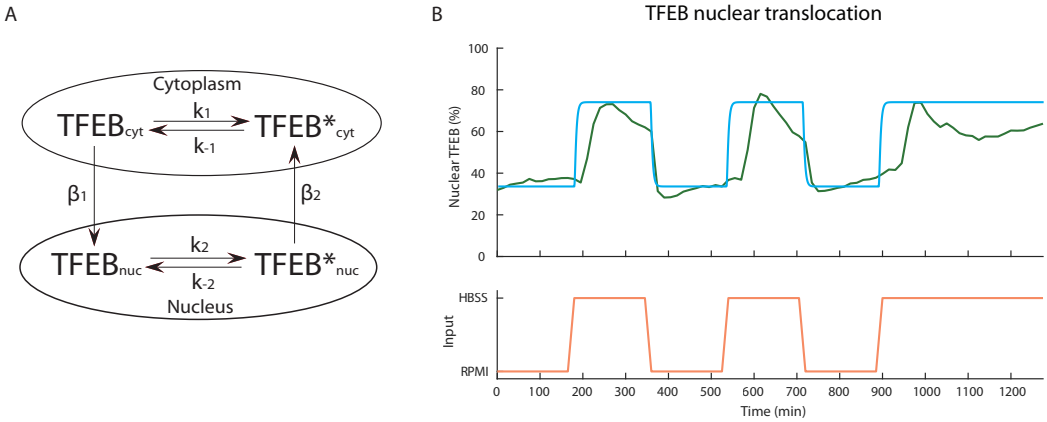

Figure 4.6: **A bicompartimental model for TFEB nuclear translocation.** (**A**) Schematic representation of reactions involved in TFEB post-translational regulation. In this scheme, TFEB_{cyt} represents cytoplasmatic TFEB; TFEB_{nuc} the nuclear one; $\text{TFEB}^*_{\text{cyt}}$ and $\text{TFEB}^*_{\text{nuc}}$ are the respective phosphorylated species; k_i are the phosphorylation rates; k_{-i} the dephosphorylation ones; β_i the transport rates. (**B**) Comparison of experimental measurements and numerical simulations of TFEB translocation in the presence of a train of starvation pulses. Numerical simulation of nuclear TFEB fluorescence following a simulated train of starvation pulses is shown with a blue line. The average signal across the experimental single-cell traces is shown with a green line.

calisation and phosphorylation status: (i) phosphorylated cytoplasmic TFEB ($\text{TFEB}^*_{\text{cyt}}$), (ii) dephosphorylated cytoplasmic TFEB (TFEB_{cyt}), (iii) phosphorylated nuclear TFEB ($\text{TFEB}^*_{\text{nuc}}$), and (iv) dephosphorylated nuclear TFEB (TFEB_{nuc}). The external input $u \in [0,1]$ represents either nutrient-rich medium (0) or starvation (1). Its effect it is to drive the direction of the reactions by promoting the phosphorylation, in presence of nutrients, or the dephosphorylation, otherwise.

Following the assumption in [166], we assumed that each de/phosphorylation reaction follows a first order kinetics:

$$\dot{X}^* = K(u)\,X\,, \tag{4.1}$$

where X^* is the phosphorylated form of X and $K(u)$ is the phosphorylation rate that depends on the external input u. We modelled the described effect of input on de/phospho-

rylation rates as follows:

$$K(u) = \begin{cases} k(1-u) & \text{for phosphorylation rates} \\ ku & \text{for dephosphorylation rates} \end{cases} \tag{4.2}$$

where k is a constant.

Let x_1, x_2, x_3 and x_4 be respectively TFEB_{cyt}, $\text{TFEB}^*_{\text{cyt}}$, TFEB_{nuc} and $\text{TFEB}^*_{\text{nuc}}$. Combining Eqs. 4.1 and 4.2 and adding the transport reactions, TFEB model can be described as follow:

$$\dot{x}_1 = k_{-1}ux_2 - k_1(1-u)x_1 - \beta_1 x_1 \tag{4.3a}$$

$$\dot{x}_2 = k_1(1-u)x_1 - k_{-1}ux_2 + \beta_2 x_4 \tag{4.3b}$$

$$\dot{x}_3 = k_{-2}ux_4 - k_2(1-u)x_3 + \beta_1 x_1 \tag{4.3c}$$

$$\dot{x}_4 = k_2(1-u)x_3 - k_{-2}ux_4 - \beta_2 x_4 \tag{4.3d}$$

where k_1 and k_2 are the phosphorylation rates in cytoplasm and in nucleus, k_{-1} and k_{-2} are the dephosphorylation rates in cytoplasm and in nucleus, β_1 is the cytoplasm-nuclear transport rate and β_2 is the nuclear-cytoplasm transport rate.

Since de/phosphorilation reactions and transport are much faster than protein production and degradation, we further assumed that the total concentration of TFEB is conserved inside the cell. Therefore, we added to the model the following concentration rule:

$$x_1 + x_2 + x_3 + x_4 = 1 \tag{4.4}$$

where the overall concentration of TFEB is assumed to be equal to 1. Hence, we can reduce the number of equations by considering, for example, $x_1 = 1 - x_2 - x_3 - x_4$. To further simplify the model, we considered symmetric the transports and the reactions, thus reducing the system parameters to two: (i) $k = k_1 = k_{-1} = k_2 = k_{-2}$, that is the reaction rate, and (ii) $\beta = \beta_1 = \beta_2$, that is the transport rate. This simplification is

justified by the observation that nuclear import of dephosphorylated TFEB and nuclear export of phosphorylated TFEB have similar kinetics [147]. In the end, the following final three dimensional dynamical model is obtained:

$$\dot{x}_2 = k(1-u)(1-x_2-x_3-x_4) - kux_2 + \beta x_4\,, \tag{4.5a}$$

$$\dot{x}_3 = kux_4 - k(1-u)x_3 + \beta(1-x_2-x_3-x_4)\,, \tag{4.5b}$$

$$\dot{x}_4 = k(1-u)x_3 - kux_4 - \beta x_4\,. \tag{4.5c}$$

Despite the model being non-linear, it becomes a piece-wise linear system if the input is switched between two fixed values [167]. This allows to study the system with the simplified techniques developed for linear systems. In our setting, starvation ($u = 1$) and fed conditions ($u = 0$) are the most relevant cases. The equilibrium points of the system described by Eqs. 4.5 for a constant input u are:

$$\bar{x} = \begin{bmatrix} \bar{x}_2 \\ \bar{x}_3 \\ \bar{x}_4 \end{bmatrix} = \begin{bmatrix} 1-u-\frac{k}{\beta+k}u(1-u) \\ u-\frac{k}{\beta+k}u(1-u) \\ \frac{k}{\beta+k}u(1-u) \end{bmatrix}. \tag{4.6}$$

Computing the equilibrium points in the two most interesting cases ($u = 0$ and $u = 1$), it is possible to appreciate that the model is able to recapitulate what is biologically expected. Indeed, during starvation ($u = 1$), TFEB is completely nuclear and dephosphorylated: $\bar{x} = [0 \quad 1 \quad 0]^T$. Instead, during refeeding, TFEB is completely cytosolic and phosphorylated: $\bar{x} = [1 \quad 0 \quad 0]^T$.

Using Matlab *Symbolic Toolbox*, we computed the *Jacobian* matrix and its eigenvalues (depending on a generic constant u) at the equilibrium point:

$$\lambda = \begin{bmatrix} -k \\ -\beta \\ -k-\beta \end{bmatrix}. \tag{4.7}$$

Interestingly, the eigenvalues are strictly negative and independent on input u, meaning that the equilibrium points are always stable nodes.

Model parameter were estimated from the literature [147]. Specifically, Napolitano *et al.* [147] demonstrated that TFEB nuclear translocation dynamics in both starvation and refeeding can be described as a linear combination of two exponentials driven by two fixed time constants ($\tau_{\text{slow}} = 216\,\text{s}$ and $\tau_{\text{fast}} = 70\,\text{s}$). Since the experiments performed in [147] were performed in a constant environment (i.e. u is constant), the model in Eqs. 4.5 will be linear and its simulated dynamics will be driven by exponential modes with the eigenvalues in Eq. 4.7, which are independent of the exact value of u. Therefore, the trajectories of the model when close to the equilibrium points will be governed by three time constants that are independent of the value of u ($\tau_1 = \frac{1}{k}$, $\tau_2 = \frac{1}{\beta}$ and $\tau_3 = \frac{1}{k+\beta}$). Considering that transport reaction rates (β) are at least an order of magnitude smaller than de/phosphorylation rates (i.e. $k \gg \beta$) [166], it can be assumed $\tau_3 \approx \tau_1$. Hence, trajectories will be a combination of two exponentials driven by two time constants (τ_1 and τ_2), in perfect agreement with the experimental results of Napolitano *et al.* [147]. Hence, we set $k = \frac{1}{70}\,\text{s}^{-1}$ and $\beta = \frac{1}{216}\,\text{s}^{-1}$.

To check whether the model could recapitulate the observed experimental data, we performed a numerical simulation by applying the same experimental input to the model. The simulation was performed in MATLAB enviroment by using the `ode45` solver. Actually, for a better comparison between the experimental and numerical data, the simulation was performed by considering an input $u = 0.3$ for the fed condition and $u = 0.7$ for the starvation and adapting the initial conditions to the experimental data ($x_0 = [0.7 \quad 0.3 \quad 0]^T$). The result is shown in Fig. 4.6B. It is possible to appreciate that the model can replicate the fast dynamics observed in the experiments during medium switches, but it cannot replicate the slower overshoot dynamics. It is important to note that, in the experiment, the overshoot dynamics are slower than the initial rise. In particular, TFEB enters the nucleus in about 20 min, while the overshoot takes about 110 min. Accordingly, it is reasonable to think that the overshoot is due to a different

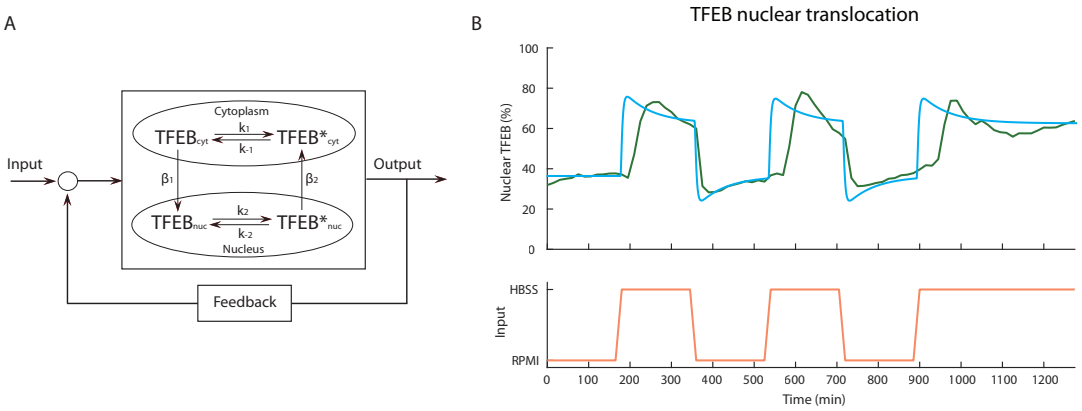

Figure 4.7: **Closed-loop model of TFEB nuclear translocation.** (**A**) Schematic representation of the feedback regulation hypothesised for the overshoot dynamics. (**B**) Comparison of experimental measurements and numerical simulations of TFEB translocation in the presence of a train of starvation pulses. Numerical simulation of nuclear TFEB fluorescence following a simulated train of starvation pulses is shown with a blue line. The average signal across the experimental single-cell traces is shown with a green line.

(and slower) biological mechanism.

Considering the biological role of TFEB, it is plausible to hypothesize that it can regulate its activity through a negative feedback loop. Indeed, as a transcription factor, the final aim of its activity is the production of its targets whose aim is to counteract the starvation to allow the cell survival. This contrasting action could have the effect of limiting also TFEB activity, as shown in Fig. 4.7A.

In order to model this feedback action, we added to the model another species that represent the TFEB targets and whose dynamics are modelled as follows:

$$\dot{x_5} = -ax_5 + b(x_3 + x_4) \tag{4.8}$$

where x_5 is the new state variable, modelling the possible feedback species, $x_3 + x_4$ is the total nuclear TFEB concentration, a and b are respectively the degradation and the production rates. In particular, a and b are assumed to be constant. To set these parameters, we considered that the overshoot lasts approximately 110 minutes (as shown in

Fig. 4.5). Therefore, we chose the parameter a to respect this constrain ($a = 0.00015\,\mathrm{s}^{-1}$). We chose the parameter $b = 0.000088\,\mathrm{s}^{-1}$, instead, to best fit the concentration of nuclear TFEB at the equilibrium point in the closed loop with the experimental data.

Finally, since the effect of this new species is counteracting the starvation, its concentration is subtracted to the external input:

$$\hat{u} = u - x_5\,. \tag{4.9}$$

This new input $\hat{u}$ is then provided to the system thus closing the loop.

The simulation performed with this complete model is shown in Fig. 4.7B. As done in the previous simulation, to have a better comparison between the experimental and numerical data, we adapted the input and the initial condition used for the simulation. We thus set $u = 0.5$ for the feeding condition, $u = 1$ for starvation, and $x_0 = [x_{0,2} \quad x_{0,3} \quad x_{0,4} \quad x_{0,5}]^T = [0.65 \quad 0.35 \quad 0 \quad 0.18]^T$ as initial condition. The simulation indicates that the closed-loop model is now able to recapitulate the TFEB overshoot dynamics, despite the real dynamics being slower; it is possible to infer the "correct" parameters to best fit the model to the data, however I did not pursue this as I was interested only in understanding whether the qualitative overshoot dynamics could be captured by this new model. At each pulse, the simulation shows clearly the fast rise, the slower overshoot, the new equilibrium, and the fast decrease. This suggests that the hypothesis formulated could be plausible, revealing a novel feedback loop biological mechanism. A delay in TFEB response to the input in experimental data is present if compared with the simulation. This delay is probably due to the fact that the microfluidic device takes 10 min to complete the media changing in the cell chamber. Furthermore, since RPMI is a medium enriched in nutrients, cells could need extra time to sense the starvation medium and to adapt to the lacking of nutrients.

The code to run all the simulations shown in this Section was developed in collaboration with Iacopo Ruolo, and it is available on *GitHub* (see Appendix B.4).

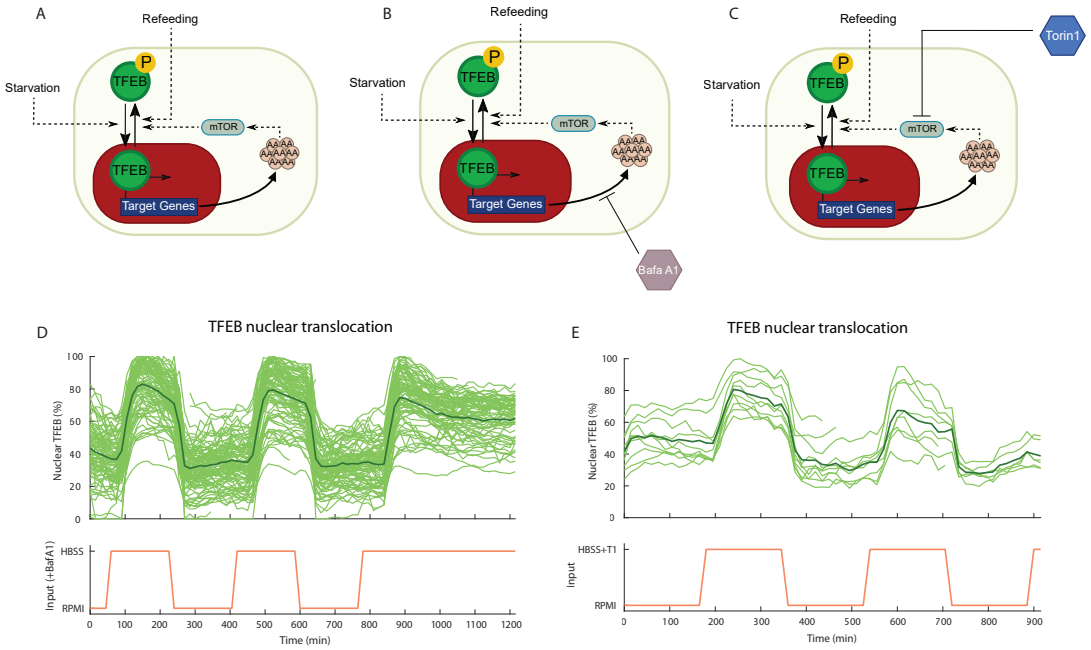

Figure 4.8: **Hypothesis on an autophagy-related feedback.** (**A**) During starvation, TFEB is dephosphorylated and translocates into the nucleus activating the transcription of its target genes whose final product is a pull of amino acids. The amino acid sensor mTOR is consequently reactivated and can phosphorylate TFEB again. (**B**) Treating cells with Bafilomycin A1, an autophagy inhibitor, prevents amino acid formation, breaking the loop. (**C**) Treating cells with Torin1, an mTOR inhibitor, keeps mTOR not active. (**D**-**E**) Each figure shows single cell traces of nuclear TFEB fluorescence (shown in the upper plot) measured in the microfluidics platform following a train of starvation pulses (shown in the lower plot). The average of the single-cell traces is highlighted with a solid line in the upper plot. In panel (**D**), the cells were treated with Bafilomycin A1 (@100 nM), an autophagy inhibitor, for the entire experimental timespan. In panel (**E**), the cells were treated with Torin1 (@300 nM), an mTOR inhibitor, during the starvation pulses.

4.3.3 Testing the hypothesis on an autophagy-related feedback

As discussed in Section 4.1, under starvation, TFEB is dephosphorylated and translocates into the nucleus activating its target genes and, in particular, autophagic genes. Autophagy promotes the generation of a pool of amino acids used by the cell to survive in this situation of stress. The cell amino acid sensor is mTOR that is the kinase that mainly phosphorylates TFEB. Therefore, it is conceivable that mTOR can sense, probably through SLC38A9 (the lysosomal sensor of amino acids), the pool of amino

acids produced with autophagy reactivating itself and thus phosphorylating TFEB again trapping it into the cytosol, as schematised in Fig. 4.8A. However, in this hypothesis, mTOR activity will be proportional to the nutrient amount, and therefore it is not able to completely re-phosphorylate TFEB that, as a consequence, can not complete its full relocalisation, giving rise to the overshoot.

To test this hypothesis, we performed two kinds of experiments schematised in Fig. 4.8B-C and whose results are shown in Fig. 4.8D-E.

In the first experiment, we inhibited autophagy through Bafilomycin A1, a potent and selective inhibitor of vacuolar-type H+ ATPase (V-ATPase). It suppresses macroautophagy by preventing the acidification of lysosomes [168]. As shown in Fig. 4.8B, the effect of Bafilomycin A1 on the hypothesised feedback loop should be to prevent the production of the extra pool of amino acids and thus prevent mTOR reactivation. However, as shown in Fig. 4.8D, Bafilomycin A1 treatment is not able to remove the overshoot, neither in starvation nor in refeeding conditions.

The second experiment is schematised in Fig. 4.8C. In this case, Torin1, which, as discussed in Section 4.2, is a potent mTOR inhibitor, counteracts the mTOR reactivation in response to amino acid. Since Torin1 by itself can induce TFEB translocation by inhibiting mTORC1, I used it only during starvation. As shown in Fig. 4.8E, Torin1 can not remove the overshoot, as also observed following Bafilomycin A1 treatment.

Taken together, these experiments indicate that the overshoot present in TFEB translocation dynamics is nor due to autophagy not mTOR reactivation. This leads to alteranative explanations: there is another kinase, not yet known, that can phosphorylate TFEB blocking it into the cytosol and that is produced following mTOR inhibition; or some unknown mechanism of TFEB nuclear export is implicated in this long-term regulation, or still nuclear TFEB is partailly degraded giving rise to the overshoot. This latter hyopothesis is the least plausible as we can clearly observe in some cells in the experiments that when nuclear TFEB decreases during the overshoot, cytoplasmic TFEB increases (Fig. 4.5A-B, middle plots), thus pointing to a relocation to the cytoplasm

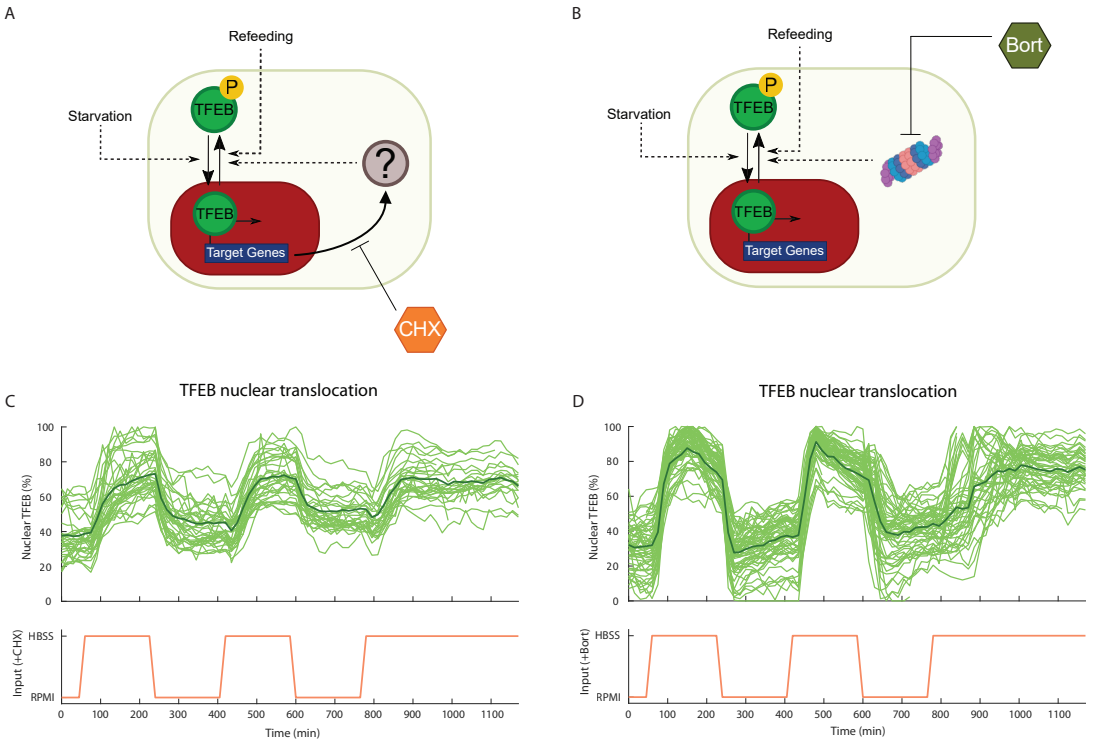

Figure 4.9: **Hypothesis on an on a protein synthesis-related feedback or a protein degradation-related feedback.** (**A**) Treating cells with Cycloheximide, a translation inhibitor, prevents the translation of TFEB target genes, breaking the loop. (**B**) Treating cells with Bortezomib, a proteasome inhibitor, blocks the likely action of the proteasome on TFEB localisation. (**C**-**D**) Each figure shows single cell traces of nuclear TFEB fluorescence (shown in the upper plot) measured in the microfluidics platform following a train of starvation pulses (shown in the lower plot). The average of the single-cell traces is highlighted with a solid line in the upper plot. During the experiments the cells were treated either with Cycloheximide (@$50\,\mu$g/ml), a translation inhibitor, (**C**) or with Bortezomib (@100nM), a proteasome inhibitor (**D**), for the entire experimental time-span.

rather than a degradation.

4.3.4 Testing the hypothesis on a protein synthesis-related feedback or a protein degradation-related overshoot

The CLEAR network is a very large set of genes whose expression is activated by TFEB. Theoretically, one or more of the 557 genes identified by Gambardella *et al.* [154]

can be implicated in TFEB negative feedback regulation highlighted by the model. As schematised in Fig. 4.9A, once in the nucleus, TFEB activates the transcription of its target genes leading to the production of different proteins, that can, in some way, promote TFEB relocalisation. To test this hypothesis, I performed an experiment by treating the cells with Cycloheximide, an antifungal antibiotic that inhibits protein synthesis in eukaryotes. Particularly, it interferes with translation initiation by inhibiting the binding of initiator tRNA to ribosomes or binding of the ribosome 60S subunits to form an initiation complex [169]. The results of this experiment are shown in Fig. 4.9C. In this case, TFEB exhibits a strikingly different dynamics, as the overshoot disappears, and TFEB reaches a 70% nuclear ratio with slower dynamics. Although this experiment seems to have been successful, it gave very little information about the mechanisms leading to the overshoot. Indeed, since it completely blocks protein synthesis, its interference in cell metabolism is too strong. Therefore, these new dynamics could be not directly related to a TFEB target and these results need to be further investigated.

To degrade proteins the cell makes use of the ubiquitin-proteasome system (UPS). The UPS degrades mostly short-lived proteins through a multistep process that requires the tagging activity of a sophisticated system. The tagging molecule is a small protein, ubiquitin, that once covalently linked to proteins, earmarks them for destruction by the 26S proteasome, a highly conserved multicatalytic ATP-dependent protease complex [170]. The UPS and autophagy have long been considered independent and parallel degradation systems. They were once thought to target different types of proteins; that is, the proteasome system degraded short-lived proteins, while the autophagy pathway degraded long-lived, large protein complexes and damaged organelles. One of the most important manifestations of the association between the UPS and autophagy is the upregulated functions of autophagy caused by UPS damage, which is often considered a compensatory mechanism that enables cells to prevent the accumulation of UPS substrates [171]. Moreover, autophagy and UPS share certain ubiquitin recognition molecules or shuttling factors. Indeed, ubiquitin binds to other protein lysine

residues and labels them with degradation signals as a substrate that can be hydrolyzed by the proteasome or lysosome [171]. Driven by this strong correlation between these pathways and by the results of Zapata *et al.* [164], I decided to test if UPS is someway related to TFEB dynamics by causing its degradation in the nucleus. To this end, I pharmacologically inhibited the proteasome through Bortezomib, a highly selective, reversible inhibitor of the 26S proteasome [172], as schematised in Fig. 4.9B. The results of this experiment are shown in Fig. 4.9D. Bortezomib treatment alters the dynamics of TFEB but the overshoot in TFEB translocation dynamics is still present, thus suggesting that degradation is not involved in the overshoot dynamics. These results confirm the presence of a regulatory mechanism involved in TFEB nuclear translocation, even if the biological mechanism connected with this feedback has to be further investigated.

4.4 TFEB nuclear translocation dynamics upon mTOR inhibitors treatments

During starvation, cells activate a lot of compensatory mechanisms to survive the stress. The mTOR pathway, thus, is not the only one that responds to this kind of stimulus. Consequently, the results presented in Section 4.3 could be due to additive or synergistic effects of different pathways. Therefore, I performed a validation of previous results by using an mTOR inhibitor.

Since Rapamycin and rapalogs are not able to induce TFEB translocation [151], I used two different ATP-competitive inhibitors: Torin1, which is the most used mTOR inhibitor, and AZD8055, which was used to confirm the results obtained with Torin1.

Recapitulating what was done with starvation, I first treated cells with a train of Torin1 (@300 nM) pulses or with a single long Torin1 (@300 nM) treatment. The results of these experiments are shown in Fig. 4.10A-B. TFEB dynamics exhibits a similar behaviour to what was observed in starvation conditions (Fig. 4.5): a fast nuclear accu-

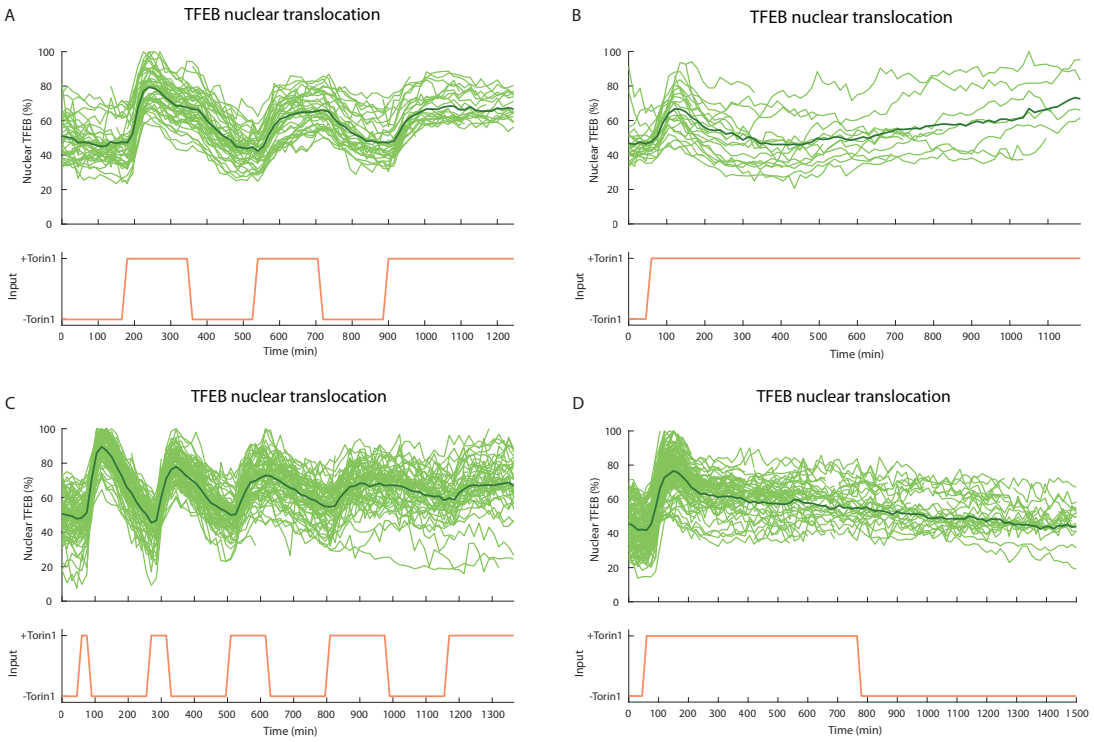

Figure 4.10: **Experimental measurements of TFEB translocation during pharmaceutical mTORC1 inhibition.** Each figure shows single cell traces of nuclear TFEB fluorescence (shown in the upper plot) measured in the microfluidics platform following the correspondent input (shown in the lower plot): a train of Torin1 (@300 nM) pulses (**A**), a single Torin1 (@300 nM) stimulus (**B**), a train of Torin1 (@1 μM) pulses of increasing duration (**C**), or a single Torin1 (@1 μM) pulse of 12 h (**D**). The average of the single-cell traces is highlighted with a solid line in the upper plot.

mulation followed by the "overshoot", that is a slower relocalisation to the cytoplasm. In this case, however, upon Torin1 removal, TFEB cytosolic localisation is much slower than in refeeding, after the starvation stress. As for the case of starvation, these results are in line with what was observed by Zapata *et al.* [164]. Indeed, upon Torin1 treatment, they observed a total TFEB activation within 0.5 h, even if for a limited duration of 1.5 h.

These effects were confirmed by other experiments in which the Torin1 concentration was changed, as shown in Fig. A.3. Indeed, both by decreasing Torin1 concentration at 50 nM (Fig. A.3A) or by increasing it at 1 μM (Fig. A.3B), TFEB response does

not change: it translocates into the nucleus with fast dynamics followed by an overshoot of slower cytosolic relocalisation. This behaviour is corroborated by the other mTOR inhibitor AZD8055, as shown in Fig. 4.12A. Also with this treatment, indeed, TFEB dynamics manifest the two usual responses: a fast rise and a slower overshoot. AZD8055, however, seems better imitating starvation conditions. Indeed, upon drug removal, TFEB relocalises to the cytosol with dynamics comparable with those manifested during refeeding.

Interestingly, in the experiments with a pulsatile Torin1 treatment (Fig. 4.10 and Fig. A.3), it is possible to observe that TFEB presented different dynamics in response to the second and third pulses. Indeed, TFEB translocates into the nucleus with slower dynamics reaching the steady-state with no overshoot (as happened in response to the co-treatment of starvation and Cycloheximide). Similar behaviour is also present in the AZD8055 pulsatile experiment, even if, in this case, TFEB was not able to respond to the second treatment (Fig. 4.12).

These alterations of TFEB dynamics during the second and third pulses could be due either to cell memory or to drug degradation in the microfludics device. To test these hypotheses, I performed an experiment in which the first pulse of Torin1 (@300 nM) was skipped, as shown in Fig. A.4. If TFEB dynamics in this experiment had recapitulated the ones exhibited during the first pulse of Torin1 treatment in Fig. 4.10A, then the difference in dynamics could be attributed to some sort of cell memory. However, results are more similar to the ones of the second pulse of Torin1 treatment in Fig. 4.10A, indicating that drug degradation in the microfluidics device is the likely cause of the observed behaviour.

Finally, I investigated the mechanisms driving the slower dynamics in TFEB nuclear export upon Torin1 removal. Interestingly, these dynamics are not present following AZD8055 treatment. Therefore, I first investigated if this behaviour were due to the timing of Torin1 treatment. To this end, I performed a first experiment in which cells were treated with a train of Torin1 (@1 μM) pulses of increasing duration (0.5 h –

1 h − 2 h − 3 h). Interestingly, as shown in Fig. 4.10C, TFEB responds very fast and very effectivly at each Torin1 pulse but then it localises with much slower dynamics into the cytosol upon Torin1 removal. These dynamics became slower and slower at each Torin1 pulse, until TFEB was not able to relocalise into the cytosol anymore. This experiment suggests that Torin1 accumulates over time in the cells. To confirm the hypothesis, I performed an experiment, shown in Fig. 4.10D, by treating the cells with 12 h of Torin1 (@1 μM). Also in this case, upon Torin1 removal, TFEB was no longer able to relocalise in the cytosol, thus confirming the hypothesis of the time-dependent drug accumulation.

4.4.1 Synergistic effect of mTOR inhibitors with other compounds

Considering the promising results obtained by inhibiting protein synthesis or degradation in starvation experiments, I decided to see whether they affect TFEB dynamics also during Torin1 treatments. The results of these experiments are shown in Fig. 4.11. Specifically, I performed both fixed duration and variable duration pulses experiments for both drugs.

Surprisingly, as shown in Fig. 4.11A-B, both treatments have a dramatic effect on TFEB localisation. In both cases upon Torin1 removal, TFEB gets trapped in the nucleus. Moreover, this behaviour is time-dependent. As matter of fact, as shown in Fig. 4.11C-D, when Torin1 treatments lasted for 0.5 h or 1 h and, in the case of Cycloheximide, also 2 h, TFEB was still able to exit from the nucleus, even if less and less after each treatment.

Furthermore, I performed a similar experiment this time by combining Bortezomib with another ATP-competitive mTOR inhibitor (AZD8055), as shown in Fig. 4.12B. Also with this other drug, the co-inhibition of mTOR and proteasome blocks TFEB in the nucleus, even if this effect is much more effective after the second treatment. Interestingly, in Baumann *et al.* [173], the authors tested a different dual PI3K-mTOR in-

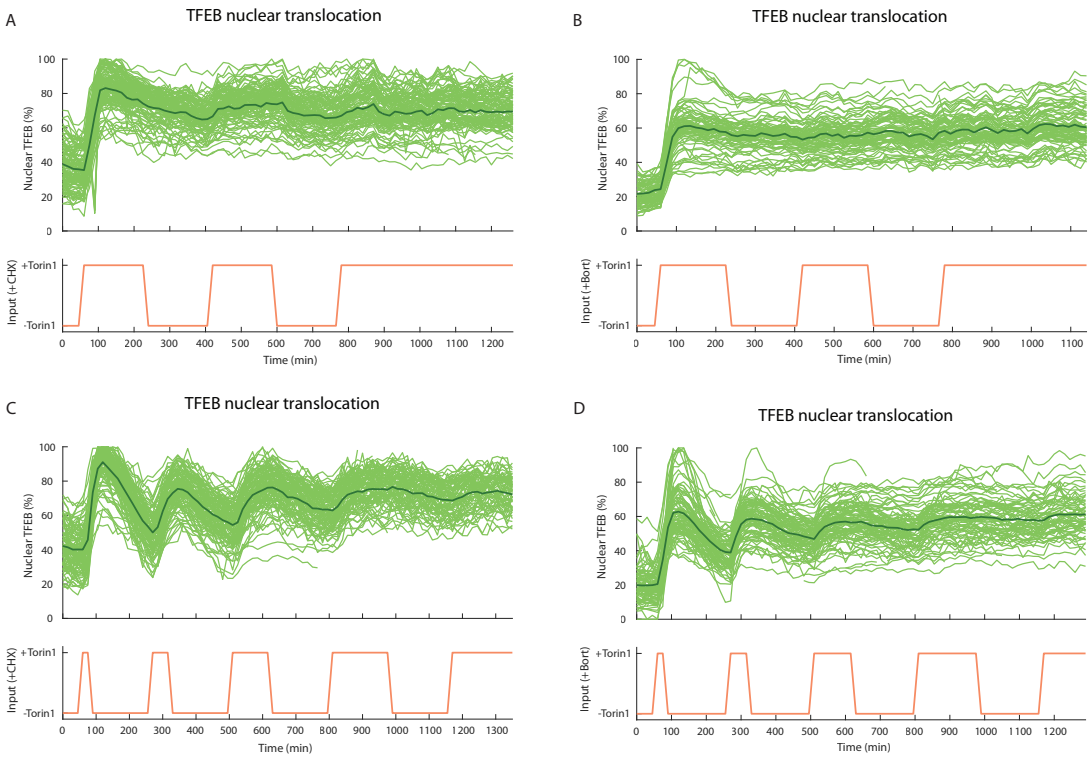

Figure 4.11: **Experimental measurements of TFEB translocation during pharmaceutical mTORC1 inhibition combined with synthesis or degradation inhibition.** Each figure shows single cell traces of nuclear TFEB fluorescence (shown in the upper plot) measured in the microfluidics platform following a train of Torin1 (@1 μM) pulses (shown in the lower plot). The average of the single-cell traces is highlighted with a solid line in the upper plot. During the experiments the cells were treated either with Cycloheximide (@50 μg/ml), a translation inhibitor, (**A**, **C**) or with Bortezomib (@100 nM), a proteasome inhibitor (**B**, **D**), for the entire experimental time-span.

hibitor NVP-BEZ235 as a chemotherapeutic agent in three different multiple myeloma cell lines. They observed a synergistic effect in reducing cell vitality when NVP-BEZ235 was used in combination with Bortezomib, although they did not put forward any mechanistic explanation for this behaviour.

It is important to observe that inhibition of mTOR by starvation combined with Bortezomib treatment does not have the same effect, as TFEB is able to translocate to the nucleus once cells are switched to full medium, even in the presence of Bortezomib (Fig. 4.9D). Therefore, the effect is specific for chemical inhibitors of mTOR such as Torin1.

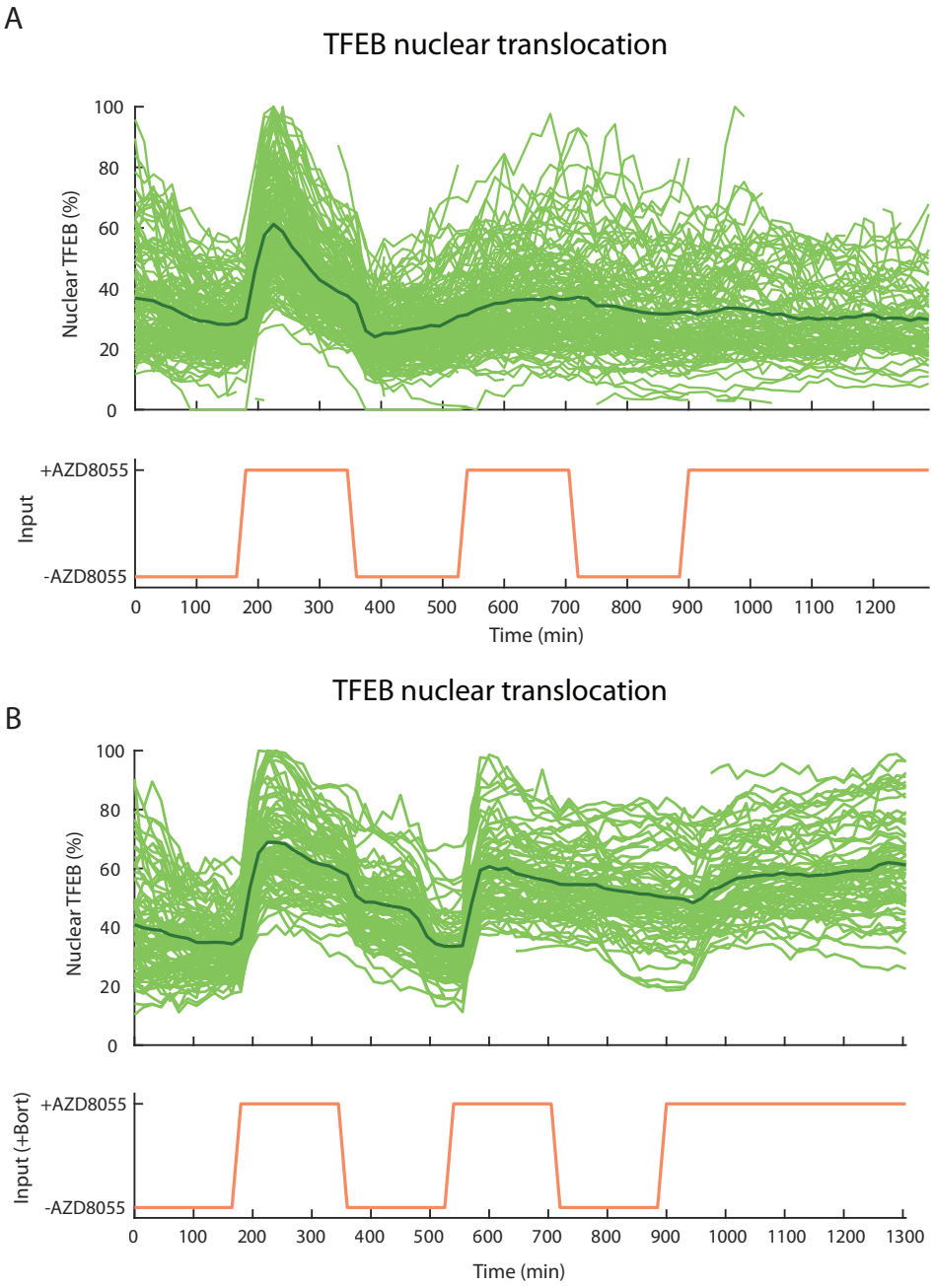

Figure 4.12: **Experimental measurements of TFEB translocation in pharmaceutical mTORC1 inhibition.** Each figure shows single cell traces of nuclear TFEB fluorescence (shown in the upper plot) measured in the microfluidics platform following a train of AZD8055 (@300 nM) pulses (shown in the lower plot). The average of the single-cell traces is highlighted with a solid line in the upper plot. During the experiments the cells were treated either with only AZD8055 (**A**) or with AZD8055 in presence of Bortezomib (@100 nM), a proteasome inhibitor (**B**), for the entire experimental time-span.

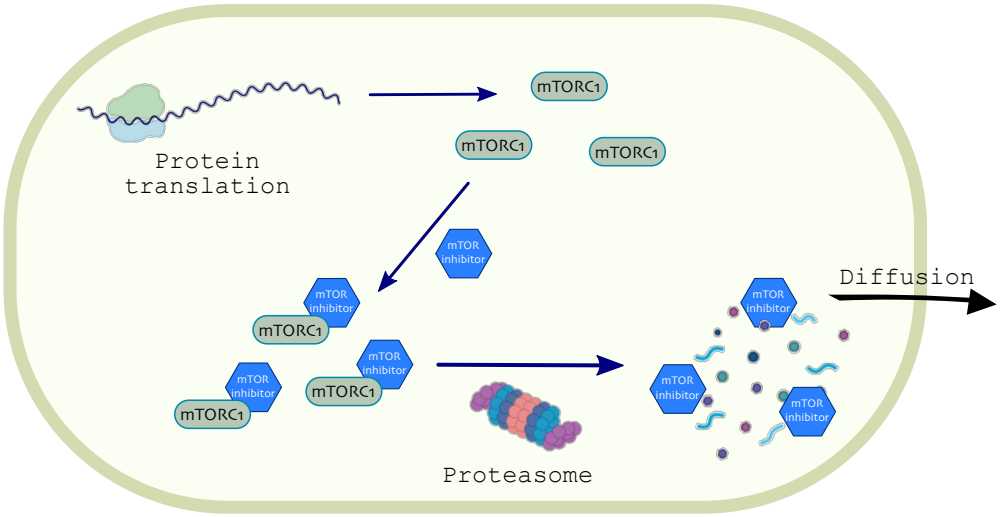

Figure 4.13: **Biological hypothesis on synergistic effect.** In presence of an mTOR inhibitor, mTORC1 is bound to it and inhibited by preventing the interaction with its targets. This mTORC1-inhibitor complex is targeted by the proteasome that degrades mTORC1 and recycles the mTOR inhibitor. The recycled mTOR inhibitor can either leave the cell through diffusion, if the drug concentration in the external medium is lower than in the cell, or target the new synthesised mTORC1.

Biological hypothesis on synergistic effect.

A possible explanation for this synergistic effect could be the one shown in Fig. 4.13. According to this hypothesis, the protein synthesis machinery produces mTOR, which is the main component of the mTORC1 complex. When an mTOR inhibitor is present in the growth medium, it enters into the cell through diffusion and binds mTOR thus inhibiting it. However, the complex formed by mTORC1 and the inhibitor is targeted by the proteasome that degrades the protein and thus the inhibitor is released and free to diffuse across the cell membrane. In the presence of Bortezomib (the proteasome inhibitor), the cell is no longer able to degrade the mTORC1-inhibitor complex thus maintaining mTORC1 inhibited and the chemical inhibitor trapped inside of the cell, as it is not able to diffuse across the membrane. In the case of Cycloheximide (the protein translation inhibitor), the explanation could be that the cell is not able to produce new mTOR able to replace the degraded one. Consequently, there is no new Torin1-free mTORC1 in the cell able to phosphorylate TFEB, which thus remains trapped in the

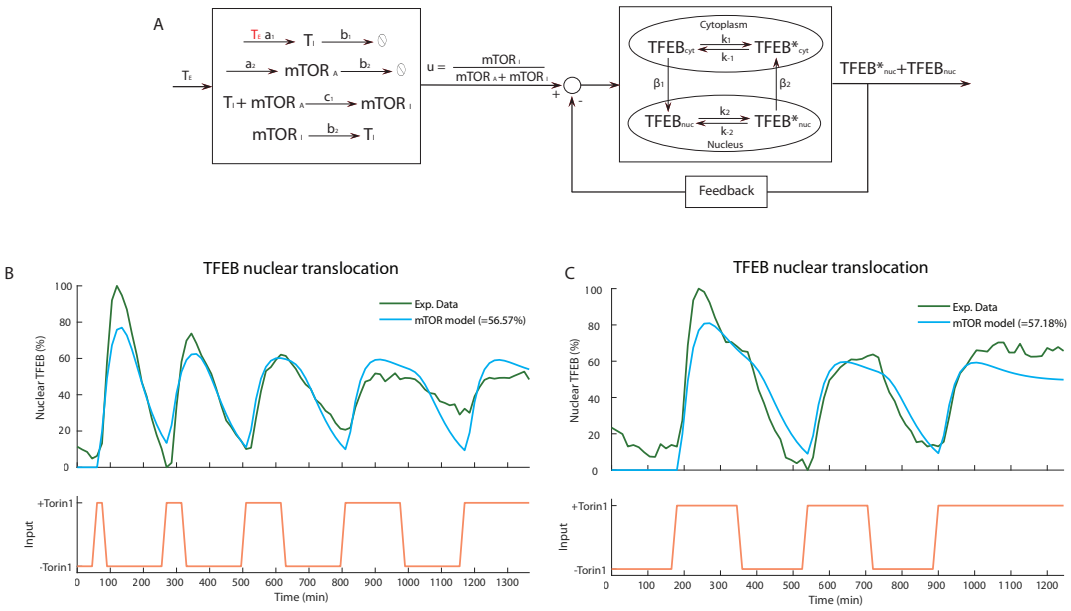

Figure 4.14: **Dynamical model of biological hypothesis on the synergistic effect.** (**A**) Schematic representation of the feedback regulation hypothesised for the overshoot dynamics. (**B**) Comparison of experimental measurements and numerical simulations of TFEB translocation in the presence of a train of Torin1 (@1 μM) pulses. Numerical simulation of nuclear TFEB fluorescence following a simulated train of starvation pulses is shown with a blue line. The average signal across the experimental single-cell traces is shown with a green line. The fitting percentage between the estimated model and the experimental data is 56.57 %. (**C**) Comparison of experimental measurements and numerical simulations of TFEB translocation in the presence of a train of Torin1 (@1 μM) pulses. Numerical simulation of nuclear TFEB fluorescence following a simulated train of starvation pulses is shown with a blue line. The average signal across the experimental single-cell traces is shown with a green line.The fitting percentage between the estimated model and the experimental data is 57.18 %.

nucleus.

To test this hypothesis, I derived a dynamical model to describe the effect of Torin1 treatment on mTOR inhibition and, specifically, the hypothesis described in Fig. 4.13. I considered the reactions showed in Fig. 4.14A (left box): (i) the diffusion of Torin1 (T_I) through the cellular membrane both in input, in presence of Torin1 in the external medium (T_E), and in output; (ii) the production and the degradation of the mTOR active form ($mTOR_A$); (iii) the inhibition of mTOR when it reacts with T_I producing the mTOR inactive form ($mTOR_I$); and (iv) the degradation of $mTOR_I$ that releases T_I. Finally,

the inhibited mTOR can induce TFEB nuclear translocation behaving as input for the closed-loop model showed in Fig. 4.14A (right box).

Let x_6 be the concentration of intracellular Torin1, and x_7 and x_8 the concentrations of active and inactive mTOR, respectively. I added to the dynamical model described by Eqs. 4.5 and 4.8 the following ODEs:

$$\dot{x}_6 = a_1 u_E - b_1 x_6 + b_2 x_7 - c_1 x_6 x_7 \,, \tag{4.10a}$$

$$\dot{x}_7 = a_2 - b_2 x_7 - c_1 x_6 x_7 \,, \tag{4.10b}$$

$$\dot{x}_8 = c_1 x_6 x_7 - b_2 x_8 \,, \tag{4.10c}$$

where a_1 is the diffusion rate through the cellular membrane in input, b_1 is the diffusion rate for the cellular export, a_2 is the production rate due to the protein synthesis machinery, b_2 is the degradation rate due to the proteasome, c_1 is the reaction rate for the inhibition of mTOR by Torin1, and $u_E \in \{0,1\}$ represents the absence or the presence of Torin1 in the growth medium. As I said, $mTOR_I$ is the species able to induce TFEB nuclear translocation, thus x_8 should be the input for the closed loop model. However, that model was derived considering an input limited between 0 and 1. Therefore, I decided to use as input the percentage of inactive mTOR out of the total mTOR. Hence, the $\hat{u}$ in Eq. 4.9 becomes:

$$\hat{u} = \frac{x_8}{x_7 + x_8} - x_5 \,. \tag{4.11}$$

To obtain the values of the parameters for the mTOR inhibition model, I performed the classical system identification procedure by starting from the input-output data taken from the experiments depicted in Fig. 4.10A,C where the system input is represented by pulses of Torin1 rich medium and standard medium (i.e. u_E in Eq. 4.10-1) and the system output is the average signal representing the TFEB nuclear percentage (i.e. $x_2 + x_3$ in Eqs. 4.5), renormalized between its minimum and maximum value. Since I already had the equations describing the process to identify, I performed a grey-box

Parameter	Description	Value
a_1 $[s^{-1}]$	Torin1 diffusion rate in input	29.57
b_1 $[s^{-1}]$	Torin1 diffusion rate in export	0.0021
c_1 $[s^{-1}]$	mTOR inhibition rate	$2.16 \cdot 10^{-4}$
a_2 $[s^{-1}]$	mTOR traslation rate	$2 \cdot 10^{-4}$
b_2 $[s^{-1}]$	mTOR degradation rate	$0.97 \cdot 10^{-4}$
k $[s^{-1}]$	TFEB phosphorilation rate	0.0027
β $[s^{-1}]$	TFEB transport rate	$5.6 \cdot 10^{-4}$
a $[s^{-1}]$	feedback species consumption	$0.86 \cdot 10^{-4}$
b $[s^{-1}]$	feedback species production	$0.89 \cdot 10^{-4}$

Table 4.1: **Parameters of mTOR inhibition model identified by the grey box identification approach.**

identification using the MATLAB function `nlgreyest` of the *System Identification Toolbox* [174] on the selected data set. The estimated model parameters are reported in Table 4.1, while the response of the identified model to the input signals are shown in Fig. 4.14B,C where they are also compared to the experimental output. The code used for this identification is available on *GitHub* (see Appendix B.4).

Using this final model, I simulated TFEB translocation when mTOR is inhibited in combination with either protein synthesis or proteasome inhibitions. Specifically, to simulate the effect of Cycloheximide (the protein synthesis inhibitor), I imposed the mTOR translation rate (i.e. a_2 in Eq. 4.10-2) equal to 0. While to simulate the effect of Bortezomib (the proteasome inhibitor), the mTOR degradation rate (i.e. b_2 in Eqs. 4.10). The simulations (Fig. 4.15) show that the biological hypothesis formulated is able to explain TFEB nuclear accumulation even upon the end of the Torin1 treatment in presence of Cycloheximide (Fig. 4.15A) or Bortezomib (Fig. 4.15B), but it can not explain the overshoot disappearing suggesting that two different biological processes are involved.

The code to run all the simulations shown in this Section is available on *GitHub* (see Appendix B.4).

Beyond the biological explanation for the phenomena that I have observed, the data shown in this Chapter could be of great interest for clinical research. Indeed, as I said,

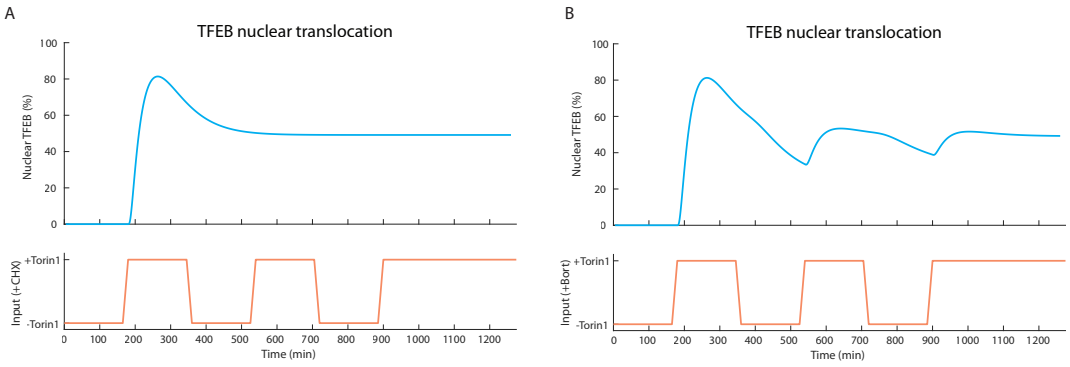

Figure 4.15: **Dynamical model of mTOR inhibition upon Torin1 treatment.** (**A**) Numerical simulation of TFEB translocation in the presence of a train of Torin1 treatments in combination with a constant protein synthesis inhibition. (**B**) Numerical simulation of TFEB translocation in the presence of a train of Torin1 treatments in combinantion with a constant proteasome inhibition.

both mTOR inhibitors and Bortezomib are both being investigated as cancer treatment, even if not in combination. However, following our results, their combination could be tested in cancer therapy to increase the greatly potentiate the effect of mTOR inhibition.

Chapter 5

Conclusions

In this Thesis, I combined experimental approaches from Molecular and Cell Biology with Biomedical Engineering methodologies for quantitative investigation and control of gene regulatory networks. Specifically, I focused on two different biological processes: the cell cycle in yeast and the mTORC1 pathway in human cells. To achieve this aim, I took advantage of the tools of Cybergenetics, a novel discipline at the edge between Synthetic Biology and Biomedical and Control engineering. Cybergenetics, indeed, provides quantitative and methodological tools to understand how gene networks work and to robustly steer their behavior in a prescribed fashion. My research has been focused on an external control strategy, as reviewed in Chapter 1, using an automated microfluidic-based experimental platform described in Chapter 2, already implemented in the lab and that I have refined with custom segmentation algorithms.

In Chapter 3, I used the microfluidics platform with yeast cells to implement control strategies that I designed (the open-loop and the stop&go controllers) to automatically synchronise the cell cycle in a population of yeast cells. Both control strategies successfully achieved the control task, as demonstrated by all the synchronisation indices I evaluated. However, while the open-loop strategy has to be finely tuned to set the right conditions for the synchronisation, the closed-loop stop&go control strategy is much more robust to environmental disturbances, e.g. the changes in temperature and carbon

source. Indeed, the stop&go strategy is able to self-adapt to alternation in the cell cycle, which is an intrinsic characteristic of feedback loop control strategies.

In Chapter 4, I used a similar platform but in human cells and for a different purpose, that is to quantitatively measure and model the dynamics of TFEB nuclear translocation, and to understand the underlying biological mechanisms driving it. The results I obtained allowed me to observe complex and rich dynamics following amino-acid starvation and chemical inhibition of mTOR, which were previously unreported; I then developed a dynamical mathematical model describing TFEB nuclear shuttling and mTORC1 activity. Moreover, I was able to propose a new mechanism of action for how drugs that inhibit mTORC1 work. Indeed, experimental data highlighted the presence of a novel mechanism never observed before. I speculated that the particular behaviour observed was due to negative feedback regulation, but I was not able to identify the involved pathway. Nevertheless, the experiments done to identify the feedback regulation have shown that a combination of mTOR inhibitors with other pharmacological agents inhibiting the proteasome or protein synthesis have a synergistic effect, as demonstrated by the TFEB nuclear accumulation upon mTOR inhibitor removal, leading to new possible therapies for those diseases where mTORC1 inhibition is beneficial, such as cancer and neurodegenerative diseases.

5.1 Future perspectives

5.1.1 Self-synchronised yeast population

The results shown in Chapter 3 open the way for the construction of the first ever self-synchronised yeast population. Such a strain will present all the advantages highlighted in Chapter 3, allowing to study the cell-cycle phases and to increase production of biomolecules, without the drawbacks of an external controller, e.g. the need for real-time measurements of cell-cycle phase.

The theoretical work presented in [175] shows the feasibility of creating such a yeast strain by implementing in the cell the stop&go control strategy through a quorum sensing mechanism. In brief, such controller could be achieved by engineering a strain where the cell cycle stops in G_1 if the quorum sensing molecule does not reach a predefined threshold, and by having the cells produce the quorum sensing molecule only in the G1 phase. Hence, if enough cells are in the G1 phase, then the quorum sensing molecule will accumulate and start the cell cycle in all the cells synchronously; during the cell cycle the quorum sensing is not produced and thus will decrease below the threshold, and thus stopping cells in G1 again. Such a strain is now being engineering in our lab.

5.1.2 mTORC1 inhibitors in cancer treatment

As described in Chapter 4, the mTOR pathway is deregulated in different pathological conditions, including cancer and neurodegenerative disorders. Therefore, mTOR inhibitors are often used for the treatment of these conditions. I showed that combining mTOR inhibitors with other compounds, such as protein synthesis and degradation inhibitors, can prolong the effect of the treatment. Furthermore, in [173], the authors demonstrated a synergistic effect in reducing cell vitality by combining an mTOR inhibitor with a proteasome inhibitor in three different multiple myeloma cell lines, confirming the data I have obtained.

It would be interesting to understand the biological mechanism steering this behaviour and to test the hypothesis presented in Chapter 4 regarding the cellular accumulation of the inhibitor. To this end, we are performing an experiment in which we will take advantage of the nature of these drugs. Briefly, these compounds compete with the ATP in the binding with mTOR. Thus, by providing enough ATP to the cell, it should be possible to prevent drug binding to mTOR. Therefore, if the hypothesis on the Torin1 persistence in the cell is correct, then by treating with ATP the cell should

recover its wild-type phenotype, i.e. TFEB should become again cytosolic, even in the presence of protein synthesis and degradation inhibitors.

Finally, these data may have great relevance in clinics. Therefore, it would be important to test if cancer cell lines are sensitive to co-treatment of mTOR inhibiton with Bortezomib, a proteasome inhibitor currently in clinical trial for melanoma. If these experiments confirm this synergistic effect, these combinations could be tested in clinical trials to improve the treatment in some forms of cancer.

Appendix A

Supplementary Data

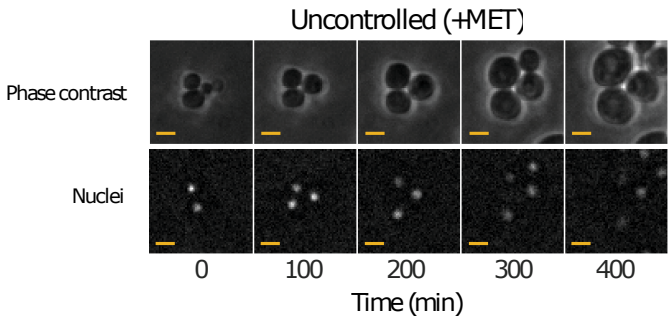

Figure A.1: **Htb2-mCherry expression in methionine-rich medium.** Representative phase contrast (top) and fluorescence (bottom) images from a time-lapse experiments of cells grown in methionine-rich medium at the indicated time points. Scale bar, 5 μm.

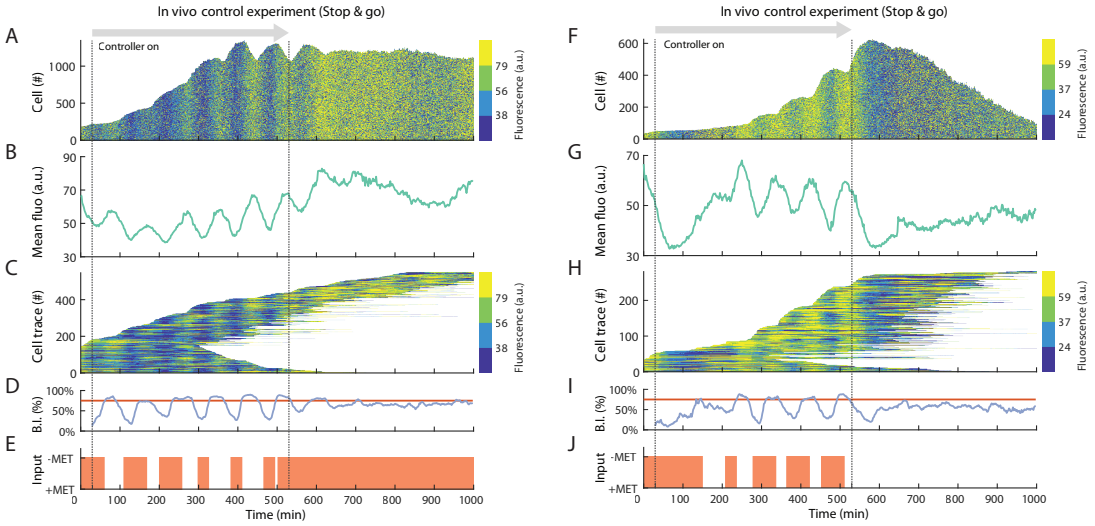

Figure A.2: **Closed-loop stop&go control experiments in the non-cycling yeast strain.** Experimental implementation of the stop&go control strategy. An initial calibration phase of 30 min was required to set up the phase estimation algorithm. Dashed lines indicate the start and the end of the control experiment, after which cells are grown in methionine-depleted (**A**-**E**) or methionine-rich medium (**F**-**J**). (**A**, **F**) Distribution of the YFP fluorescence signals measured across the cell population over time. Fluorescence values are binned into 4 colours, corresponding to the quartiles, for clarity of visualisation. (**B**, **G**) Time-series of the mean YFP fluorescence signal measured across the cell population. (**C**, **H**) Single-cell fluorescence traces over time. Each horizontal line corresponds to one cell. (**D**, **I**) Time-series of the budding index (blue) signal. The red line denotes the expected value of the budding index in the case of a totally desynchronised cell population. (**E**, **J**) Growth medium delivered to the cells as a function of time. +MET: methionine-rich medium, -MET: methionine-depleted medium.

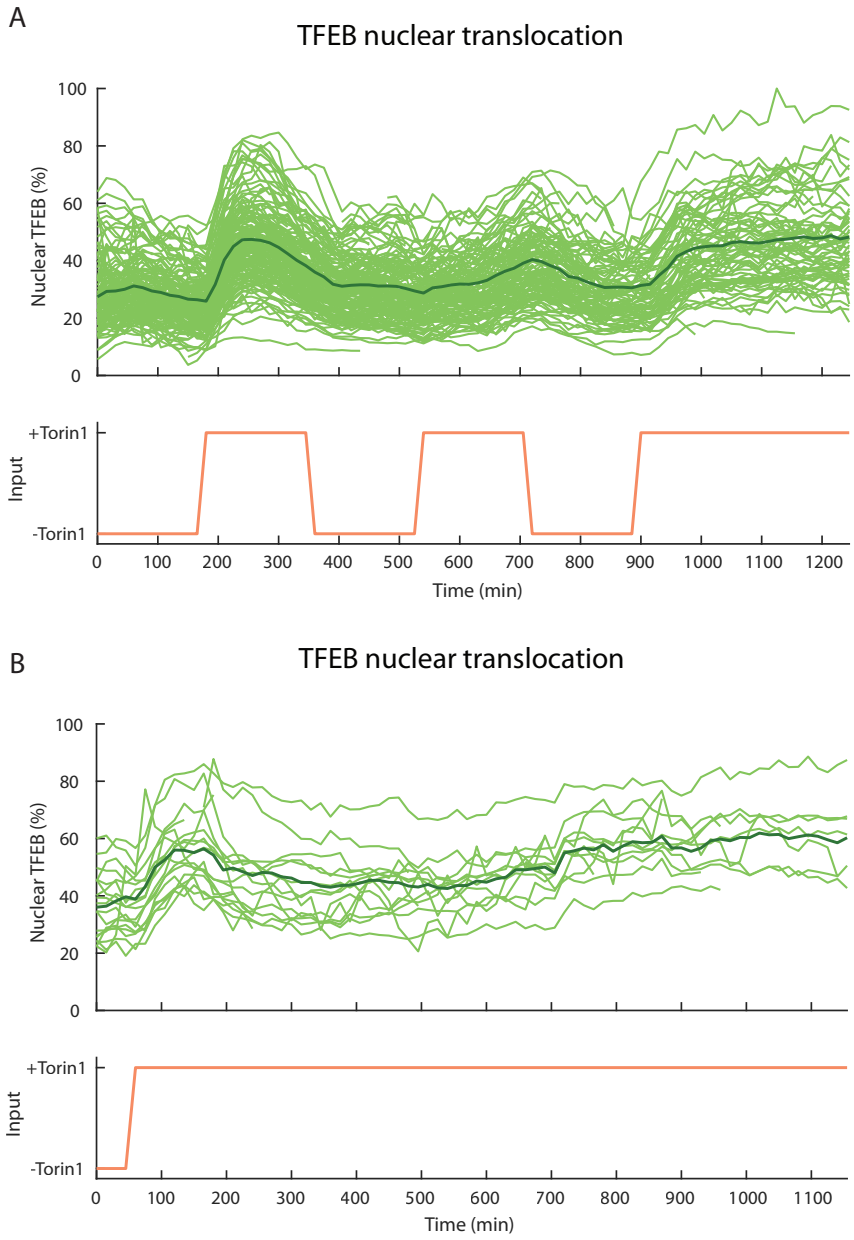

Figure A.3: **Experimental measurements of TFEB translocation in pharmaceutical mTORC1 inhibition at different concentrations.** Each figure shows single cell traces of nuclear TFEB fluorescence (shown in the upper plot) measured in the microfluidics platform following the correspondent input (shown in the lower plot): a train of Torin1 (@50 nM) pulses (**A**) or a single Torin1 (@1 μM) stimulus (**B**). The average of the single-cell traces is highlighted with a solid line in the upper plot.

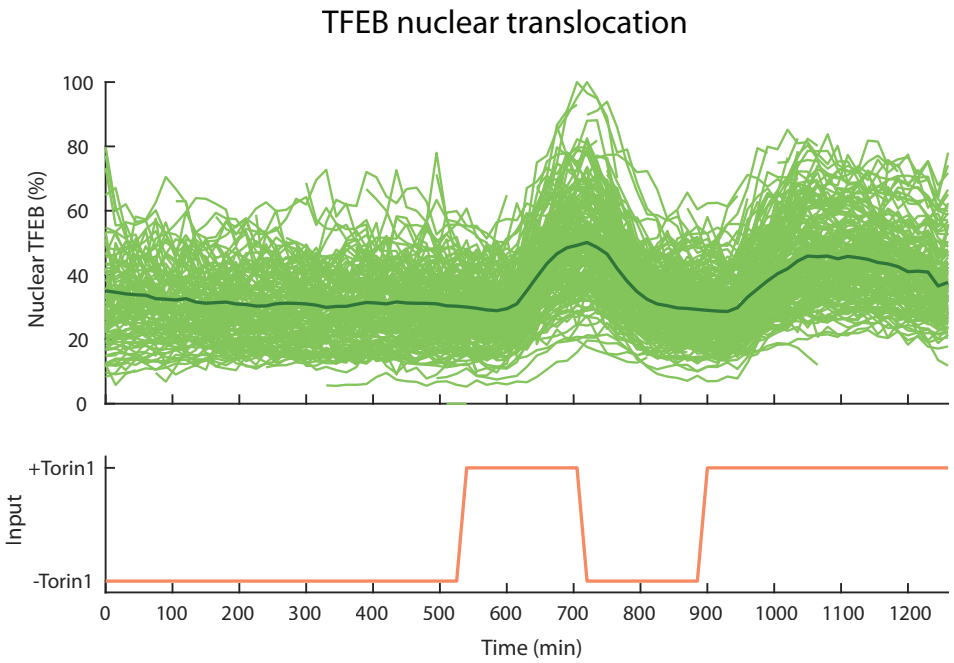

Figure A.4: **Experimental measurements of TFEB translocation in pharmaceutical mTORC1 inhibition.** The upper plot shows single cell traces of nuclear TFEB fluorescence measured in the microfluidics platform following a train of Torin1 (@300 nM) pulses (shown in the lower plot). The average of the single-cell traces is highlighted with a solid line in the upper plot.

Appendix B

Material and Methods

B.1 Microfluidics

B.1.1 Device fabrication protocol

I have used replica molding technique to obtain polydimethylsiloxane (PDMS) replicas of both devices presented in Section 2.1 [57, 59] by using a master mold of the features as blueprint. The master mold has been produced using a 4" silicon wafer as substrate (Silicon Valley Microelectronics, US) by a way of layer-by-layer photolithography [176].

Before the fabrication of the microfluidic devices the master is exposed to chlorotrimethylsilane (Sigma-Aldrich Co.) vapours for 10 min to create an anti-sticking silane layer for PDMS. PDMS is prepared by mixing Sylgard 184 Elastomer curing agent and base (DOW corning) in a 1 : 10 ratio. PDMS is poured onto the master mold, degassed for 30 minutes, cured for 2h at 80 °C, allowed to cool to room temperature and then peeled from the wafer. PDMS was then autoclaved for 30 min at 121 °C to ensure long-term viability of cells in the devices. Holes for the ports were punched using a 22-guage (for Ferry's device) and 24-gauge (for Kolnik's device) blunt needle in order to create fluidic ports for the access of cells and liquid substances. The PDMS devices

obtained are rinsed in isopropyl alcohol and distilled water to remove debris. For each PDMS piece containing microchannels a thin glass slide (0.16 mm and 25 mm, VWR) is cleaned in methanol and 70% ethyl alcohol. Finally the PDMS layers and glass slides are exposed to oxygen plasma in Plasma Cleaner machine (ZEPTO version B, Diener electronic GmbH) for 1 min and brought into contact forms a strong irreversible bond between two surfaces. As last step, all devices were checked for faults inside and outside the channels.

B.2 Yeast strain protocols

B.2.1 Yeast strain derivation

The *Saccharomyces cerevisiae* strain used in this study is congenic with W303 strain. It is the SJR14a4d strain from [82] (a kind gift from S. J. Rahi).

B.2.2 Cell culture

Unless otherwise specified, yeast cells were grown at 30 °C in either synthetic complete medium, composed of yeast nitrogen base (0.67% w/v) with all amino acids; or synthetic complete drop-out medium, composed of yeast nitrogen base (0.67% w/v) with all amino acids except methionine; both supplemented with glucose (2% w/v) as carbon source. For the carbon source perturbation experiments, synthetic complete media were supplemented with galactose (2% w/v).

B.2.3 Microfluidic device cell loading protocol

For microfluidics experiments, cells from a frozen glycerol stock (−80 °C) were resuspended in 10 mL of either methionine-free growth medium, grown overnight in a shaking incubator at 220 r.p.m. and 30 °C, and then injected in the microfluidics device as previously described [34] by pouring the batch culture in a syringe that was

temporarily connected to the loading port of the microfluidics device.

B.2.4 Microfluidic experiments protocol

The microfluidics experimental platform was initialised as previously described [34]. Briefly, a microfluidics device was filled with double distilled water for removing air bubbles. Next, two syringes filled with −MET and +MET media were first mounted on the automated actuation system and connected to the inlet ports of the microfluidics device. Afterwards, three syringes filled with double distilled water were connected to the remaining ports of the microfluidics device for balancing the flow pressure inside the device. Finally, the microfluidics device was placed in the opaque cage incubator of the microscope that was preheated to either 30 °C (nominal condition) or 27 °C (temperature perturbed condition). Unless otherwise specified, after loading, cells were left to settle in the chamber for 15 min fed with either methionine-depleted growth medium. After that, the operator run the image acquisition and the custom MATLAB software. At the beginning of the experiment, a region of interest (ROI) was selected on the first acquired phase contrast image. Specifically, the ROI defines the area containing the *S. cerevisiae* cells that have to be segmented and tracked, and whose fluorescence signals have to be quantified.

B.2.5 Perturbed experiments protocol

For perturbed experiments, the microfluidic platform was set as described in Section B.2.4. For the carbon source perturbation experiments, cells were treated as in the nominal conditions except that galactose was the only carbon source added to the growth media. For the temperature perturbation experiments, cells were grown as in the nominal conditions except that the temperature was maintained at 27 °C in lieu of 30 °C.

B.3 Mammalian cells protocols

B.3.1 Cell line derivation

The HeLa cell line was built starting from the cell line described in the Settembre *et al.* [143], In which I stably integrated by the Tol2 transposon vector system [177] a plasmid constitutively expressing the nuclear marker H2B-mCherry, as described in [40]. In order to generate the monoclonal cell population mCherry/eGFP double positive cells were sorted at single cell level by using a BD FACS Aria III (Becton Dickinson) and subsequently they were expanded.

B.3.2 Cell culture

HeLa cells are cultured in RPMI (EuroClone) supplemented with 10% FBS (EuroClone), 1% Penicillin/Streptomycin (EuroClone), 2 mM Glutamine (EuroClone) and 1 mg/ml G418 (Sigma-Aldrich Co.) and are kept in a standard tissue culture incubator at 37 °C, 5% CO_2 and 98% of humidity.

Cells are splitted twice per week using PBS (Gibco) and trypsin (Gibco) and seeded at 2000 cells/cm^2.

The day before the loading of the microfluidic device cells were splitted 1 : 3 and placed back into the incubator.

B.3.3 Microfluidic device cell loading protocol

For device loading, cells are washed with sterile Phosphate-Buffered Saline (PBS, Gibco), detached from the culture dishes by exposing to 0.25% Trypsin EDTA for 1 minute and centrifuged to form a pellet. Then, to obtain a seeding density of about 10 cells per chamber, the cells pellet is re-suspended in complete media.

The channel of the device are then completely filled with fluid (except for the culture chambers) by applying complete media first through port 5 and then through port 2 once

it is filled with fluid. The cell suspension is loaded into the main channel of the device from port 2 and a vacuum is applied in the channel adjacent to the culture chambers (ports 3 and 4) to evacuate air and replace the chamber volume with fluid containing cells. Remaining untrapped cells in the main channel are washed away at a high flow rate without disturbing cells inside the traps. Fluidic connections from the ports of the device to syringes containing growth medium are then established using 24 gauge PTFE tubing (Cole-Parmer Inc.) interfaced via 22 gauge stainless steel luer stub pins.

Once cells are loaded in the microfluidc device, they are allowed in a cell culture incubator for 24 h in perfusion conditions providing that the cells in chambers receive fresh medium from syringe connected to port 5 and the waste medium is washed trough port 1, while all the other ports (2, 6 and 7) are plugged.

B.3.4 Experimental protocol

The microfluidics experimental platform was initialised as previously described [40]. The device is secured on the microscope stage within an environmental chamber maintained at 37 °C with humidified 5% CO_2 and 60 mL syringes are connected to its ports and hanged at different heights, in order to regulate the flow from the inlets (ports 6 and 7) to the outlets (ports 5, 1 and 2) according to hydrostatic pressure. The syringes connected to the outlets port contain 10 mL of standard complete culture medium and they serve as a waste tanks. The syringes connected to the inlets port are filled as indicated in each experiment, i.e. with the drugs indicated in Table B.1, and secured on the linear actuator. Specifically, the not inducer syringe was filled with standard growth medium eventually enriched with the indicated inhibitor (Bafilomycin A1, Bortezomib or Cycloheximide), whereas the inducer syringe was filled with either HBSS (Gibco) or medium with Torin1 at the indicated concentration, both eventually enriched with the indicated inhibitor (Bafilomycin A1, Bortezomib or Cycloheximide).

Table B.1: Compounds used for microfluidic experiments in mammalian cells

Drug	Concentration	Company
Torin1	50 nM, 300 nM or 1 μM	Selleck Chemicals
AZD8055	300 nM	Selleck Chemicals
Bafilomycin A1	100 nM	Selleck Chemicals
Bortezomib	100 nM	Selleck Chemicals
Cycloheximide	50 μg/ml	Sigma

B.4 Code availability

The source code used for the cell cycle synchronisation is available on GitHub at `https://github.com/dibbelab/Cycloop49`.

The source code used for the study of mTORC1 inhibition dynamics is available from GitHub at `https://github.com/dibbelab/s.napolitanoPhd/tree/main/TFEB_QuantitativeAnalysis`.

Bibliography

[1] A. S. Hansen and E. K. O'Shea, "Limits on information transduction through amplitude and frequency regulation of transcription factor activity," *Elife*, vol. 4, p. e06559, 2015.

[2] A. Isomura and R. Kageyama, "Ultradian oscillations and pulses: coordinating cellular responses and cell fate decisions," *Development*, vol. 141, no. 19, pp. 3627–3636, 2014.

[3] J. E. Toettcher, O. D. Weiner, and W. A. Lim, "Using optogenetics to interrogate the dynamic control of signal transmission by the ras/erk module," *Cell*, vol. 155, no. 6, pp. 1422–1434, 2013.

[4] Y. E. Antebi, N. Nandagopal, and M. B. Elowitz, "An operational view of intercellular signaling pathways," *Current opinion in systems biology*, vol. 1, pp. 16–24, 2017.

[5] J. H. Levine, Y. Lin, and M. B. Elowitz, "Functional roles of pulsing in genetic circuits," *Science*, vol. 342, no. 6163, pp. 1193–1200, 2013.

[6] A. L. Paek, J. C. Liu, A. Loewer, W. C. Forrester, and G. Lahav, "Cell-to-cell variation in p53 dynamics leads to fractional killing," *Cell*, vol. 165, no. 3, pp. 631–642, 2016.

[7] A. S. Hansen, N. Hao, and E. K. O'shea, "High-throughput microfluidics to control and measure signaling dynamics in single yeast cells," *Nature protocols*, vol. 10, no. 8, pp. 1181–1197, 2015.

[8] J. Stewart-Ornstein and G. Lahav, "p53 dynamics in response to dna damage vary across cell lines and are shaped by efficiency of dna repair and activity of the kinase atm," *Science signaling*, vol. 10, no. 476, 2017.

[9] K. Lane, D. Van Valen, M. M. DeFelice, D. N. Macklin, T. Kudo, A. Jaimovich, A. Carr, T. Meyer, D. Pe'er, S. C. Boutet *et al.*, "Measuring signaling and rna-seq in the same cell links gene expression to dynamic patterns of nf-κb activation," *Cell systems*, vol. 4, no. 4, pp. 458–469, 2017.

[10] S. Zambrano, I. De Toma, A. Piffer, M. E. Bianchi, and A. Agresti, "Nf-κb oscillations translate into functionally related patterns of gene expression," *Elife*, vol. 5, p. e09100, 2016.

[11] M. Junkin, A. J. Kaestli, Z. Cheng, C. Jordi, C. Albayrak, A. Hoffmann, and S. Tay, "High-content quantification of single-cell immune dynamics," *Cell reports*, vol. 15, no. 2, pp. 411–422, 2016.

[12] R. A. Kellogg, R. Gómez-Sjöberg, A. A. Leyrat, and S. Tay, "High-throughput microfluidic single-cell analysis pipeline for studies of signaling dynamics," *Nature protocols*, vol. 9, no. 7, pp. 1713–1726, 2014.

[13] R. A. Kellogg and S. Tay, "Noise facilitates transcriptional control under dynamic inputs," *Cell*, vol. 160, no. 3, pp. 381–392, 2015.

[14] S. Tay, J. J. Hughey, T. K. Lee, T. Lipniacki, S. R. Quake, and M. W. Covert, "Single-cell nf-κb dynamics reveal digital activation and analogue information processing," *Nature*, vol. 466, no. 7303, pp. 267–271, 2010.

[15] M. Santorelli, D. Perna, A. Isomura, I. Garzilli, F. Annunziata, L. Postiglione, B. Tumaini, R. Kageyama, and D. di Bernardo, "Reconstitution of an ultradian oscillator in mammalian cells by a synthetic biology approach," *ACS synthetic biology*, vol. 7, no. 5, pp. 1447–1455, 2018.

[16] S. Yoshiura, T. Ohtsuka, Y. Takenaka, H. Nagahara, K. Yoshikawa, and R. Kageyama, "Ultradian oscillations of stat, smad, and hes1 expression in response to serum," *Proceedings of the National Academy of Sciences*, vol. 104, no. 27, pp. 11 292–11 297, 2007.

[17] H. Hirata, S. Yoshiura, T. Ohtsuka, Y. Bessho, T. Harada, K. Yoshikawa, and R. Kageyama, "Oscillatory expression of the bhlh factor hes1 regulated by a negative feedback loop," *Science*, vol. 298, no. 5594, pp. 840–843, 2002.

[18] I. Imayoshi, A. Isomura, Y. Harima, K. Kawaguchi, H. Kori, H. Miyachi, T. Fujiwara, F. Ishidate, and R. Kageyama, "Oscillatory control of factors determining multipotency and fate in mouse neural progenitors," *Science*, vol. 342, no. 6163, pp. 1203–1208, 2013.

[19] M. Khammash, M. Di Bernardo, and D. Di Bernardo, "Cybergenetics: Theory and methods for genetic control system," in *2019 IEEE 58th Conference on Decision and Control (CDC)*. IEEE, 2019, pp. 916–926.

[20] K. J. Åström and P. R. Kumar, "Control: A perspective." *Autom.*, vol. 50, no. 1, pp. 3–43, 2014.

[21] D. Del Vecchio, A. J. Dy, and Y. Qian, "Control theory meets synthetic biology," *Journal of The Royal Society Interface*, vol. 13, no. 120, p. 20160380, 2016.

[22] G. Perrino, A. Hadjimitsis, R. Ledesma-Amaro, and G.-B. Stan, "Control engineering and synthetic biology: working in synergy for the analysis and control of microbial systems," *Current Opinion in Microbiology*, vol. 62, pp. 68–75, 2021.

[23] V. Hsiao, A. Swaminathan, and R. M. Murray, "Control theory for synthetic biology: recent advances in system characterization, control design, and controller implementation for synthetic biology," *IEEE Control Systems Magazine*, vol. 38, no. 3, pp. 32–62, 2018.

[24] F. Ceroni, A. Boo, S. Furini, T. E. Gorochowski, O. Borkowski, Y. N. Ladak, A. R. Awan, C. Gilbert, G.-B. Stan, and T. Ellis, "Burden-driven feedback control of gene expression," *Nature methods*, vol. 15, no. 5, pp. 387–393, 2018.

[25] T. Frei, F. Cella, F. Tedeschi, J. Gutiérrez, G.-B. Stan, M. Khammash, and V. Siciliano, "Characterization and mitigation of gene expression burden in mammalian cells," *Nature communications*, vol. 11, no. 1, pp. 1–14, 2020.

[26] R. D. Jones, Y. Qian, V. Siciliano, B. DiAndreth, J. Huh, R. Weiss, and D. Del Vecchio, "An endoribonuclease-based feedforward controller for decoupling resource-limited genetic modules in mammalian cells," *Nature communications*, vol. 11, no. 1, pp. 1–16, 2020.

[27] G. Lillacci, Y. Benenson, and M. Khammash, "Synthetic control systems for high performance gene expression in mammalian cells," *Nucleic acids research*, vol. 46, no. 18, pp. 9855–9863, 2018.

[28] H.-H. Huang, M. Bellato, Y. Qian, P. Cárdenas, L. Pasotti, P. Magni, and D. Del Vecchio, "dcas9 regulator to neutralize competition in crispri circuits," *Nature communications*, vol. 12, no. 1, pp. 1–7, 2021.

[29] G. Fiore, A. Matyjaszkiewicz, F. Annunziata, C. Grierson, N. J. Savery, L. Marucci, and M. di Bernardo, "In-silico analysis and implementation of a multicellular feedback control strategy in a synthetic bacterial consortium," *ACS Synthetic Biology*, vol. 6, no. 3, pp. 507–517, 2017.

[30] F. Annunziata, A. Matyjaszkiewicz, G. Fiore, C. S. Grierson, L. Marucci, M. di Bernardo, and N. J. Savery, "An orthogonal multi-input integration system to control gene expression in escherichia coli," *ACS synthetic biology*, vol. 6, no. 10, pp. 1816–1824, 2017.

[31] L. Pasotti, M. Bellato, N. Politi, M. Casanova, S. Zucca, M. G. C. De Angelis, and P. Magni, "A synthetic close-loop controller circuit for the regulation of an extracellular molecule by engineered bacteria," *IEEE transactions on biomedical circuits and systems*, vol. 13, no. 1, pp. 248–258, 2018.

[32] B. Shannon, C. G. Zamora-Chimal, L. Postiglione, D. Salzano, C. S. Grierson, L. Marucci, N. J. Savery, and M. di Bernardo, "In vivo feedback control of an antithetic molecular-titration motif in escherichia coli using microfluidics," *ACS Synthetic Biology*, vol. 9, no. 10, pp. 2617–2624, 2020, * An in-vivo study in microfluidics showing that it is possible to finely regulate gene expression in a population embedding an integral feedback control.

[33] M. Whiteley, S. P. Diggle, E. P. Greenberg, and E. O. Wilson, "Bacterial quorum sensing: the progress and promise of an emerging research area," *Nature*, vol. 551, no. 7680, pp. 313–320, 2017.

[34] G. Fiore, G. Perrino, M. Di Bernardo, and D. Di Bernardo, "In vivo real-time control of gene expression: a comparative analysis of feedback control strategies in yeast," *ACS synthetic biology*, vol. 5, no. 2, pp. 154–162, 2016.

[35] C. Fracassi, L. Postiglione, G. Fiore, and D. Di Bernardo, "Automatic control of gene expression in mammalian cells," *ACS synthetic biology*, vol. 5, no. 4, pp. 296–302, 2016.

[36] A. Milias-Argeitis, M. Rullan, S. K. Aoki, P. Buchmann, and M. Khammash, "Automated optogenetic feedback control for precise and robust regulation of

gene expression and cell growth," *Nature communications*, vol. 7, no. 1, pp. 1–11, 2016.

[37] J.-B. Lugagne, S. S. Carrillo, M. Kirch, A. Köhler, G. Batt, and P. Hersen, "Balancing a genetic toggle switch by real-time feedback control and periodic forcing," *Nature communications*, vol. 8, no. 1, pp. 1–8, 2017.

[38] R. Chait, J. Ruess, T. Bergmiller, G. Tkačik, and C. C. Guet, "Shaping bacterial population behavior through computer-interfaced control of individual cells," *Nature communications*, vol. 8, no. 1, pp. 1–11, 2017.

[39] M. Rullan, D. Benzinger, G. W. Schmidt, A. Milias-Argeitis, and M. Khammash, "An optogenetic platform for real-time, single-cell interrogation of stochastic transcriptional regulation," *Molecular cell*, vol. 70, no. 4, pp. 745–756, 2018.

[40] L. Postiglione, S. Napolitano, E. Pedone, D. L. Rocca, F. Aulicino, M. Santorelli, B. Tumaini, L. Marucci, and D. di Bernardo, "Regulation of gene expression and signaling pathway activity in mammalian cells by automated microfluidics feedback control," *ACS synthetic biology*, vol. 7, no. 11, pp. 2558–2565, 2018.

[41] M. O. Din, A. Martin, I. Razinkov, N. Csicsery, and J. Hasty, "Interfacing gene circuits with microelectronics through engineered population dynamics," *Science advances*, vol. 6, no. 21, p. eaaz8344, 2020.

[42] A. G. Goglia and J. E. Toettcher, "A bright future: optogenetics to dissect the spatiotemporal control of cell behavior," *Current opinion in chemical biology*, vol. 48, pp. 106–113, 2019.

[43] A. Banderas, M. Le Bec, C. Cordier, and P. Hersen, "Autonomous and assisted control for synthetic microbiology," *International Journal of Molecular Sciences*, vol. 21, no. 23, p. 9223, 2020.

[44] J. P. Newman, M.-f. Fong, D. C. Millard, C. J. Whitmire, G. B. Stanley, and S. M. Potter, "Optogenetic feedback control of neural activity," *Elife*, vol. 4, p. e07192, 2015.

[45] E. Pedone, L. Postiglione, F. Aulicino, D. L. Rocca, S. Montes-Olivas, M. Khazim, D. di Bernardo, M. P. Cosma, and L. Marucci, "A tunable dual-input system for on-demand dynamic gene expression regulation," *Nature communications*, vol. 10, no. 1, pp. 1–13, 2019.

[46] A. Guarino, D. Fiore, D. Salzano, and M. di Bernardo, "Balancing cell populations endowed with a synthetic toggle switch via adaptive pulsatile feedback control," *ACS synthetic biology*, vol. 9, no. 4, pp. 793–803, 2020.

[47] J. Uhlendorf, A. Miermont, T. Delaveau, G. Charvin, F. Fages, S. Bottani, G. Batt, and P. Hersen, "Long-term model predictive control of gene expression at the population and single-cell levels," *Proceedings of the National Academy of Sciences*, vol. 109, no. 35, pp. 14 271–14 276, 2012.

[48] P. Harrigan, H. D. Madhani, and H. El-Samad, "Real-time genetic compensation defines the dynamic demands of feedback control," *Cell*, vol. 175, no. 3, pp. 877–886, 2018.

[49] N. J. Treloar, A. J. Fedorec, B. Ingalls, and C. P. Barnes, "Deep reinforcement learning for the control of microbial co-cultures in bioreactors," *PLoS computational biology*, vol. 16, no. 4, p. e1007783, 2020.

[50] F. Menolascina, G. Fiore, E. Orabona, L. De Stefano, M. Ferry, J. Hasty, M. di Bernardo, and D. di Bernardo, "In-vivo real-time control of protein expression from endogenous and synthetic gene networks," *PLoS Comput Biol*, vol. 10, no. 5, p. e1003625, 2014.

[51] J. E. Toettcher, D. Gong, W. A. Lim, and O. D. Weiner, "Light-based feedback for controlling intracellular signaling dynamics," *Nature methods*, vol. 8, no. 10, pp. 837–839, 2011.

[52] D. Fiore, A. Guarino, and M. di Bernardo, "Analysis and control of genetic toggle switches subject to periodic multi-input stimulation," *IEEE control systems letters*, vol. 3, no. 2, pp. 278–283, 2018.

[53] A. Sootla, N. Strelkowa, D. Ernst, M. Barahona, and G.-B. Stan, "Toggling a genetic switch using reinforcement learning," *arXiv preprint arXiv:1303.3183*, 2013.

[54] M. L. Perkins, D. Benzinger, M. Arcak, and M. Khammash, "Cell-in-the-loop pattern formation with optogenetically emulated cell-to-cell signaling," *Nature communications*, vol. 11, no. 1, pp. 1–10, 2020, ** External control was used to simulate cell-to-cell signaling demonstrating the feasibility of multicellular control through quorum sensing mechanism.

[55] G. Perrino, D. Fiore, S. Napolitano, F. Galdi, A. La Regina, M. di Bernardo, and D. di Bernardo, "Feedback control promotes synchronisation of the cell-cycle across a population of yeast cells," in *2019 IEEE 58th Conference on Decision and Control (CDC)*. IEEE, 2019, pp. 933–938.

[56] G. Perrino, C. Wilson, M. Santorelli, and D. di Bernardo, "Quantitative characterization of α-synuclein aggregation in living cells through automated microfluidics feedback control," *Cell reports*, vol. 27, no. 3, pp. 916–927, 2019.

[57] M. S. Ferry, I. A. Razinkov, and J. Hasty, "Microfluidics for synthetic biology: from design to execution," *Methods in enzymology*, vol. 497, pp. 295–372, 2011.

[58] A. D. Stroock, S. K. Dertinger, A. Ajdari, I. Mezić, H. A. Stone, and G. M. Whitesides, "Chaotic mixer for microchannels," *Science*, vol. 295, no. 5555, pp. 647–651, 2002.

[59] M. Kolnik, L. S. Tsimring, and J. Hasty, "Vacuum-assisted cell loading enables shear-free mammalian microfluidic culture," *Lab on a chip*, vol. 12, no. 22, pp. 4732–4737, 2012.

[60] F. Menolascina, "Synthetic gene networks identification and control by means of microfluidic devices," Ph.D. dissertation, Computational biology and Bioinformatics, 2011.

[61] G. Fiore, "Identification and control of gene networs in living cells," Ph.D. dissertation, Computational biology and Bioinformatics, 2015.

[62] D. Bradley and G. Roth, "Adaptive thresholding using the integral image," *Journal of graphics tools*, vol. 12, no. 2, pp. 13–21, 2007.

[63] H. Li, M. A. Lavin, and R. J. Le Master, "Fast hough transform: A hierarchical approach," *Computer Vision, Graphics, and Image Processing*, vol. 36, no. 2-3, pp. 139–161, 1986.

[64] Pangyuteng. Convert voronoi cells to region mask. MATLAB Central File Exchange. [Online]. Available: https://www.mathworks.com/matlabcentral/fileexchange/43032-convert-voronoi-cells-to-region-mask

[65] W. Niblack, *An introduction to digital image processing*. Prentice-Hall, Inc., 1990.

[66] J. Motl. Niblack local thresholding. MATLAB Central File Exchange. [Online]. Available: https://www.mathworks.com/matlabcentral/fileexchange/40849-niblack-local-thresholding

[67] O. Hilsenbeck, M. Schwarzfischer, D. Loeffler, S. Dimopoulos, S. Hastreiter, C. Marr, F. J. Theis, and T. Schroeder, "faster: a user-friendly tool for ultrafast and robust cell segmentation in large-scale microscopy," *Bioinformatics*, vol. 33, no. 13, pp. 2020–2028, 2017.

[68] N. Otsu, "A threshold selection method from gray-level histograms," *IEEE transactions on systems, man, and cybernetics*, vol. 9, no. 1, pp. 62–66, 1979.

[69] M. Winter, W. Mankowski, E. Wait, E. C. De La Hoz, A. Aguinaldo, and A. R. Cohen, "Separating touching cells using pixel replicated elliptical shape models," *IEEE transactions on medical imaging*, vol. 38, no. 4, pp. 883–893, 2018.

[70] M. Acar, J. T. Mettetal, and A. Van Oudenaarden, "Stochastic switching as a survival strategy in fluctuating environments," *Nature genetics*, vol. 40, no. 4, pp. 471–475, 2008.

[71] T. C. Neymann, S. Wegerhoff, and S. Engell, "Synchronization of budding yeast cultures," *IFAC Proceedings Volumes*, vol. 44, no. 1, pp. 8384–8390, 2011.

[72] A. P. Rosebrock, "Methods for synchronization and analysis of the budding yeast cell cycle," *Cold Spring Harbor Protocols*, vol. 2017, no. 1, pp. pdb–top080 630, 2017.

[73] G. Perrino, S. Napolitano, F. Galdi, A. La Regina, D. Fiore, T. Giuliano, M. di Bernardo, and D. di Bernardo, "Automatic synchronisation of the cell cycle in budding yeast through closed-loop feedback control," *Nature communications*, vol. 12, no. 1, pp. 1–12, 2021.

[74] D. O. Morgan, *The cell cycle: principles of control*. New science press, 2007.

[75] K. Roberts, B. Alberts, A. Johnson, P. Walter, and T. Hunt, *Molecular biology of the cell*. New York: Garland Science, 2002.

[76] F. R. Cross, "Starting the cell cycle: what's the point?" *Current opinion in cell biology*, vol. 7, no. 6, pp. 790–797, 1995.

[77] B. J. Brewer, E. Chlebowicz-Sledziewska, and W. L. Fangman, "Cell cycle phases in the unequal mother/daughter cell cycles of saccharomyces cerevisiae." *Molecular and cellular biology*, vol. 4, no. 11, p. 2529, 1984.

[78] L. Dirick, T. Böhm, and K. Nasmyth, "Roles and regulation of cln-cdc28 kinases at the start of the cell cycle of saccharomyces cerevisiae." *The EMBO journal*, vol. 14, no. 19, pp. 4803–4813, 1995.

[79] H. C. Vodermaier, "Apc/c and scf: controlling each other and the cell cycle," *Current Biology*, vol. 14, no. 18, pp. R787–R796, 2004.

[80] J.-M. Peters, "Scf and apc: the yin and yang of cell cycle regulated proteolysis," *Current opinion in cell biology*, vol. 10, no. 6, pp. 759–768, 1998.

[81] B. Schneider, Q.-H. Yang, and A. Futcher, "Linkage of replication to start by the cdk inhibitor sic1," *Science*, vol. 272, no. 5261, pp. 560–562, 1996.

[82] S. J. Rahi, K. Pecani, A. Ondracka, C. Oikonomou, and F. R. Cross, "The cdk-apc/c oscillator predominantly entrains periodic cell-cycle transcription," *Cell*, vol. 165, no. 2, pp. 475–487, 2016.

[83] J. A. Perry and S. Kornbluth, "Cdc25 and wee1: analogous opposites?" *Cell division*, vol. 2, no. 1, pp. 1–12, 2007.

[84] J. B. Moseley, "Wee1 and cdc25: tools, pathways, mechanisms, questions," *Cell cycle*, vol. 16, no. 7, p. 599, 2017.

[85] S. J. Rahi, J. Larsch, K. Pecani, A. Y. Katsov, N. Mansouri, K. Tsaneva-Atanasova, E. D. Sontag, and F. R. Cross, "Oscillatory stimuli differentiate adapting circuit topologies," *Nature methods*, vol. 14, no. 10, p. 1010, 2017.

[86] F. R. Cross, "Daf1, a mutant gene affecting size control, pheromone arrest, and cell cycle kinetics of saccharomyces cerevisiae." *Molecular and cellular biology*, vol. 8, no. 11, p. 4675, 1988.

[87] R. Nash, G. Tokiwa, S. Anand, K. Erickson, and A. Futcher, "The whi1+ gene of saccharomyces cerevisiae tethers cell division to cell size and is a cyclin homolog." *The EMBO journal*, vol. 7, no. 13, pp. 4335–4346, 1988.

[88] C. Wittenberg, K. Sugimoto, and S. I. Reed, "G1-specific cyclins of s. cerevisiae: cell cycle periodicity, regulation by mating pheromone, and association with the p34cdc28 protein kinase," *Cell*, vol. 62, no. 2, pp. 225–237, 1990.

[89] M. Tyers, G. Tokiwa, and B. Futcher, "Comparison of the saccharomyces cerevisiae g1 cyclins: Cln3 may be an upstream activator of cln1, cln2 and other cyclins." *The EMBO journal*, vol. 12, no. 5, pp. 1955–1968, 1993.

[90] G. Charvin, F. Cross, and E. Siggia, "Forced periodic expression of g1 cyclins phase-locks the budding yeast cell cycle," *Proceedings of the National Academy of Sciences*, vol. 106, no. 16, pp. 6632–6637, 2009.

[91] D. Williamson and A. Scopes, "A rapid method for synchronizing division in the yeast, saccharomyces cerevisiae," *Nature*, vol. 193, no. 4812, pp. 256–257, 1962.

[92] D. Johnson and C. Walker, "Cyclins and cell cycle checkpoints," *Annual review of pharmacology and toxicology*, vol. 39, 1999.

[93] P. K. Davis, A. Ho, and S. F. Dowdy, "Biological methods for cell-cycle synchronization of mammalian cells," *Biotechniques*, vol. 30, no. 6, pp. 1322–1331, 2001.

[94] J. Y. Hur, M. C. Park, K.-Y. Suh, and S.-H. Park, "Synchronization of cell cycle of saccharomyces cerevisiae by using a cell chip platform," *Molecules and cells*, vol. 32, no. 5, pp. 483–488, 2011.

[95] M. A. Juanes, "Methods of synchronization of yeast cells for the analysis of cell cycle progression," *The Mitotic Exit Network*, pp. 19–34, 2017.

[96] S. Di Talia, J. M. Skotheim, J. M. Bean, E. D. Siggia, and F. R. Cross, "The effects of molecular noise and size control on variability in the budding yeast cell cycle," *Nature*, vol. 448, no. 7156, pp. 947–951, 2007.

[97] L. H. Hartwell and M. W. Unger, "Unequal division in saccharomyces cerevisiae and its implications for the control of cell division." *The Journal of cell biology*, vol. 75, no. 2, pp. 422–435, 1977.

[98] J. D. Sheppard and P. S. Dawson, "Cell synchrony and periodic behaviour in yeast populations," *The Canadian Journal of Chemical Engineering*, vol. 77, no. 5, pp. 893–902, 1999.

[99] A. Amon, S. Irniger, and K. Nasmyth, "Closing the cell cycle circle in yeast: G2 cyclin proteolysis initiated at mitosis persists until the activation of g1 cyclins in the next cycle," *Cell*, vol. 77, no. 7, pp. 1037–1050, 1994.

[100] J. M. Skotheim, S. Di Talia, E. D. Siggia, and F. R. Cross, "Positive feedback of g1 cyclins ensures coherent cell cycle entry," *Nature*, vol. 454, no. 7202, pp. 291–296, 2008.

[101] C. Garmendia-Torres, O. Tassy, A. Matifas, N. Molina, and G. Charvin, "Multiple inputs ensure yeast cell size homeostasis during cell cycle progression," *Elife*, vol. 7, p. e34025, 2018.

[102] D. Gilbert, "The nature of the cell cycle and the control of cell proliferation," *BioSystems*, vol. 5, no. 4, pp. 197–206, 1974.

[103] G. Charvin, C. Oikonomou, E. D. Siggia, and F. R. Cross, "Origin of irreversibility of cell cycle start in budding yeast," *PLoS Biol*, vol. 8, no. 1, p. e1000284, 2010.

[104] K. C. Chen, L. Calzone, A. Csikasz-Nagy, F. R. Cross, B. Novak, and J. J. Tyson, "Integrative analysis of cell cycle control in budding yeast," *Molecular biology of the cell*, vol. 15, no. 8, pp. 3841–3862, 2004.

[105] A. Ciliberto, B. Novak, and J. J. Tyson, "Mathematical model of the morphogenesis checkpoint in budding yeast," *The Journal of cell biology*, vol. 163, no. 6, pp. 1243–1254, 2003.

[106] J. E. Ferrell Jr, T. Y.-C. Tsai, and Q. Yang, "Modeling the cell cycle: why do certain circuits oscillate?" *Cell*, vol. 144, no. 6, pp. 874–885, 2011.

[107] F. Li, T. Long, Y. Lu, Q. Ouyang, and C. Tang, "The yeast cell-cycle network is robustly designed," *Proceedings of the National Academy of Sciences*, vol. 101, no. 14, pp. 4781–4786, 2004.

[108] K. Mangla, D. L. Dill, and M. A. Horowitz, "Timing robustness in the budding and fission yeast cell cycles," *PLoS One*, vol. 5, no. 2, p. e8906, 2010.

[109] Y. Zhang, M. Qian, Q. Ouyang, M. Deng, F. Li, and C. Tang, "Stochastic model of yeast cell-cycle network," *Physica D: Nonlinear Phenomena*, vol. 219, no. 1, pp. 35–39, 2006.

[110] C. Oguz, A. Palmisano, T. Laomettachit, L. T. Watson, W. T. Baumann, and J. J. Tyson, "A stochastic model correctly predicts changes in budding yeast cell cycle dynamics upon periodic expression of cln2," *PloS one*, vol. 9, no. 5, p. e96726, 2014.

[111] J. J. Tyson. Modeling the budding yeast cell cycle. [Online]. Available: http://mpf.biol.vt.edu/research/budding_yeast_model/pp/index.php

[112] Y. Kuramoto, *Chemical Oscillations, Waves, and Turbulence*. Springer-Verlag, 1984.

[113] A. T. Winfree, *The geometry of biological time*. Springer Science & Business Media, 2001, vol. 12.

[114] G. Perrino, D. Fiore, S. Napolitano, M. di Bernardo, and D. di Bernardo, "Towards feedback control of the cell-cycle across a population of yeast cells," in *2019 18th European Control Conference (ECC)*. IEEE, 2019, pp. 2644–2650.

[115] G. Perrino and D. di Bernardo, "Synchronisation of yeast cell cycle through quorum sensing coupling," *bioRxiv*, 2020.

[116] M. Vanoni, M. Vai, and G. Frascotti, "Effects of temperature on the yeast cell cycle analyzed by flow cytometry," *Cytometry: The Journal of the International Society for Analytical Cytology*, vol. 5, no. 5, pp. 530–533, 1984.

[117] T. D. Nguyen-Huu, C. Gupta, B. Ma, W. Ott, K. Josić, and M. R. Bennett, "Timing and variability of galactose metabolic gene activation depend on the rate of environmental change," *PLoS computational biology*, vol. 11, no. 7, p. e1004399, 2015.

[118] M. Laplante and D. M. Sabatini, "mtor signaling at a glance," *Journal of cell science*, vol. 122, no. 20, pp. 3589–3594, 2009.

[119] K. J. Condon and D. M. Sabatini, "Nutrient regulation of mtorc1 at a glance," *Journal of cell science*, vol. 132, no. 21, 2019.

[120] G. Y. Liu and D. M. Sabatini, "mtor at the nexus of nutrition, growth, ageing and disease," *Nature Reviews Molecular Cell Biology*, vol. 21, no. 4, pp. 183–203, 2020.

[121] Y. Zheng and Y. Jiang, "mtor inhibitors at a glance," *Molecular and cellular pharmacology*, vol. 7, no. 2, p. 15, 2015.

[122] L. Li, H. J. Friedrichsen, S. Andrews, S. Picaud, L. Volpon, K. Ngeow, G. Berridge, R. Fischer, K. L. Borden, P. Filippakopoulos *et al.*, "A tfeb nuclear export signal integrates amino acid supply and glucose availability," *Nature communications*, vol. 9, no. 1, pp. 1–15, 2018.

[123] X. Long, Y. Lin, S. Ortiz-Vega, K. Yonezawa, and J. Avruch, "Rheb binds and regulates the mtor kinase," *Current biology*, vol. 15, no. 8, pp. 702–713, 2005.

[124] E. Kim, P. Goraksha-Hicks, L. Li, T. P. Neufeld, and K.-L. Guan, "Regulation of torc1 by rag gtpases in nutrient response," *Nature cell biology*, vol. 10, no. 8, pp. 935–945, 2008.

[125] Y. Sancak, T. R. Peterson, Y. D. Shaul, R. A. Lindquist, C. C. Thoreen, L. Bar-Peled, and D. M. Sabatini, "The rag gtpases bind raptor and mediate amino acid signaling to mtorc1," *Science*, vol. 320, no. 5882, pp. 1496–1501, 2008.

[126] K. Inoki, Y. Li, T. Xu, and K.-L. Guan, "Rheb gtpase is a direct target of tsc2 gap activity and regulates mtor signaling," *Genes & development*, vol. 17, no. 15, pp. 1829–1834, 2003.

[127] A. Garami, F. J. Zwartkruis, T. Nobukuni, M. Joaquin, M. Roccio, H. Stocker, S. C. Kozma, E. Hafen, J. L. Bos, and G. Thomas, "Insulin activation of rheb, a mediator of mtor/s6k/4e-bp signaling, is inhibited by tsc1 and 2," *Molecular cell*, vol. 11, no. 6, pp. 1457–1466, 2003.

[128] L. S. Harrington, G. M. Findlay, A. Gray, T. Tolkacheva, S. Wigfield, H. Rebholz, J. Barnett, N. R. Leslie, S. Cheng, P. R. Shepherd *et al.*, "The tsc1-2 tumor suppressor controls insulin–pi3k signaling via regulation of irs proteins," *The Journal of cell biology*, vol. 166, no. 2, pp. 213–223, 2004.

[129] L. Ma, Z. Chen, H. Erdjument-Bromage, P. Tempst, and P. P. Pandolfi, "Phosphorylation and functional inactivation of tsc2 by erk: implications for tuberous sclerosisand cancer pathogenesis," *Cell*, vol. 121, no. 2, pp. 179–193, 2005.

[130] R. J. Shaw, N. Bardeesy, B. D. Manning, L. Lopez, M. Kosmatka, R. A. DePinho, and L. C. Cantley, "The lkb1 tumor suppressor negatively regulates mtor signaling," *Cancer cell*, vol. 6, no. 1, pp. 91–99, 2004.

[131] D. M. Gwinn, D. B. Shackelford, D. F. Egan, M. M. Mihaylova, A. Mery, D. S. Vasquez, B. E. Turk, and R. J. Shaw, "Ampk phosphorylation of raptor mediates a metabolic checkpoint," *Molecular cell*, vol. 30, no. 2, pp. 214–226, 2008.

[132] C. Lipina and H. S. Hundal, "Is redd1 a metabolic eminence grise?" *Trends in Endocrinology & Metabolism*, vol. 27, no. 12, pp. 868–880, 2016.

[133] S. R. Kimball, A. D. Do, L. Kutzler, D. R. Cavener, and L. S. Jefferson, "Rapid turnover of the mtor complex 1 (mtorc1) repressor redd1 and activation of mtorc1 signaling following inhibition of protein synthesis," *Journal of Biological Chemistry*, vol. 283, no. 6, pp. 3465–3475, 2008.

[134] K. Shen, A. Choe, and D. M. Sabatini, "Intersubunit crosstalk in the rag gtpase heterodimer enables mtorc1 to respond rapidly to amino acid availability," *Molecular cell*, vol. 68, no. 3, pp. 552–565, 2017.

[135] L. Bar-Peled, L. D. Schweitzer, R. Zoncu, and D. M. Sabatini, "Ragulator is a gef for the rag gtpases that signal amino acid levels to mtorc1," *Cell*, vol. 150, no. 6, pp. 1196–1208, 2012.

[136] L. Bar-Peled, L. Chantranupong, A. D. Cherniack, W. W. Chen, K. A. Ottina, B. C. Grabiner, E. D. Spear, S. L. Carter, M. Meyerson, and D. M. Sabatini, "A tumor suppressor complex with gap activity for the rag gtpases that signal amino acid sufficiency to mtorc1," *Science*, vol. 340, no. 6136, pp. 1100–1106, 2013.

[137] R. L. Wolfson, L. Chantranupong, G. A. Wyant, X. Gu, J. M. Orozco, K. Shen, K. J. Condon, S. Petri, J. Kedir, S. M. Scaria *et al.*, "Kicstor recruits gator1 to the lysosome and is necessary for nutrients to regulate mtorc1," *Nature*, vol. 543, no. 7645, pp. 438–442, 2017.

[138] C. S. Petit, A. Roczniak-Ferguson, and S. M. Ferguson, "Recruitment of folliculin to lysosomes supports the amino acid–dependent activation of rag gtpases," *Journal of Cell Biology*, vol. 202, no. 7, pp. 1107–1122, 2013.

[139] G. A. Wyant, M. Abu-Remaileh, R. L. Wolfson, W. W. Chen, E. Freinkman, L. V. Danai, M. G. Vander Heiden, and D. M. Sabatini, "mtorc1 activator slc38a9 is required to efflux essential amino acids from lysosomes and use protein as a nutrient," *Cell*, vol. 171, no. 3, pp. 642–654, 2017.

[140] K. Hara, K. Yonezawa, M. T. Kozlowski, T. Sugimoto, K. Andrabi, Q.-P. Weng, M. Kasuga, I. Nishimoto, and J. Avruch, "Regulation of eif-4e bp1 phosphorylation by mtor," *Journal of Biological Chemistry*, vol. 272, no. 42, pp. 26 457–26 463, 1997.

[141] K. M. Hannan, Y. Brandenburger, A. Jenkins, K. Sharkey, A. Cavanaugh, L. Rothblum, T. Moss, G. Poortinga, G. A. McArthur, R. B. Pearson *et al.*, "mtor-dependent regulation of ribosomal gene transcription requires s6k1 and is mediated by phosphorylation of the carboxy-terminal activation domain of the nucleolar transcription factor ubf," *Molecular and cellular biology*, vol. 23, no. 23, pp. 8862–8877, 2003.

[142] N. Hosokawa, T. Hara, T. Kaizuka, C. Kishi, A. Takamura, Y. Miura, S.-i. Iemura, T. Natsume, K. Takehana, N. Yamada *et al.*, "Nutrient-dependent mtorc1 association with the ulk1–atg13–fip200 complex required for autophagy," *Molecular biology of the cell*, vol. 20, no. 7, pp. 1981–1991, 2009.

[143] C. Settembre, R. Zoncu, D. L. Medina, F. Vetrini, S. Erdin, S. Erdin, T. Huynh, M. Ferron, G. Karsenty, M. C. Vellard *et al.*, "A lysosome-to-nucleus signalling mechanism senses and regulates the lysosome via mtor and tfeb," *The EMBO journal*, vol. 31, no. 5, pp. 1095–1108, 2012.

[144] G. Napolitano and A. Ballabio, "Tfeb at a glance," *Journal of cell science*, vol. 129, no. 13, pp. 2475–2481, 2016.

[145] D. L. Medina, S. Di Paola, I. Peluso, A. Armani, D. De Stefani, R. Venditti, S. Montefusco, A. Scotto-Rosato, C. Prezioso, A. Forrester *et al.*, "Lysosomal calcium signalling regulates autophagy through calcineurin and tfeb," *Nature cell biology*, vol. 17, no. 3, pp. 288–299, 2015.

[146] N. Dephoure, C. Zhou, J. Villén, S. A. Beausoleil, C. E. Bakalarski, S. J. Elledge, and S. P. Gygi, "A quantitative atlas of mitotic phosphorylation," *Proceedings of the National Academy of Sciences*, vol. 105, no. 31, pp. 10 762–10 767, 2008.

[147] G. Napolitano, A. Esposito, H. Choi, M. Matarese, V. Benedetti, C. Di Malta, J. Monfregola, D. L. Medina, J. Lippincott-Schwartz, and A. Ballabio, "mtor-dependent phosphorylation controls tfeb nuclear export," *Nature communications*, vol. 9, no. 1, pp. 1–10, 2018.

[148] C. Di Malta, D. Siciliano, A. Calcagni, J. Monfregola, S. Punzi, N. Pastore, A. N. Eastes, O. Davis, R. De Cegli, A. Zampelli *et al.*, "Transcriptional activation of ragd gtpase controls mtorc1 and promotes cancer growth," *Science*, vol. 356, no. 6343, pp. 1188–1192, 2017.

[149] G. Napolitano, C. Di Malta, A. Esposito, M. E. de Araujo, S. Pece, G. Bertalot, M. Matarese, V. Benedetti, A. Zampelli, T. Stasyk *et al.*, "A substrate-specific mtorc1 pathway underlies birt-hogg-dubé syndrome," *Nature*, vol. 585, no. 7826, pp. 597–602, 2020.

[150] M. Sardiello, M. Palmieri, A. Di Ronza, D. L. Medina, M. Valenza, V. A. Gennarino, C. Di Malta, F. Donaudy, V. Embrione, R. S. Polishchuk *et al.*, "A gene network regulating lysosomal biogenesis and function," *Science*, vol. 325, no. 5939, pp. 473–477, 2009.

[151] C. Settembre, C. Di Malta, V. A. Polito, M. G. Arencibia, F. Vetrini, S. Erdin, S. U. Erdin, T. Huynh, D. Medina, P. Colella *et al.*, "Tfeb links autophagy to lysosomal biogenesis," *science*, vol. 332, no. 6036, pp. 1429–1433, 2011.

[152] D. L. Medina, A. Fraldi, V. Bouche, F. Annunziata, G. Mansueto, C. Spampanato, C. Puri, A. Pignata, J. A. Martina, M. Sardiello *et al.*, "Transcriptional activation of lysosomal exocytosis promotes cellular clearance," *Developmental cell*, vol. 21, no. 3, pp. 421–430, 2011.

[153] C. Settembre, R. De Cegli, G. Mansueto, P. K. Saha, F. Vetrini, O. Visvikis, T. Huynh, A. Carissimo, D. Palmer, T. J. Klisch *et al.*, "Tfeb controls cellular lipid metabolism through a starvation-induced autoregulatory loop," *Nature cell biology*, vol. 15, no. 6, pp. 647–658, 2013.

[154] G. Gambardella, L. Staiano, M. N. Moretti, R. De Cegli, L. Fagnocchi, G. Di Tullio, S. Polletti, C. Braccia, A. Armirotti, A. Zippo *et al.*, "Gadd34 is a modulator of autophagy during starvation," *Science advances*, vol. 6, no. 39, p. eabb0205, 2020.

[155] S. Schenone, C. Brullo, F. Musumeci, M. Radi, and M. Botta, "Atp-competitive inhibitors of mtor: an update," *Current medicinal chemistry*, vol. 18, no. 20, pp. 2995–3014, 2011.

[156] T. Xu, D. Sun, Y. Chen, and L. Ouyang, "Targeting mtor for fighting diseases: A revisited review of mtor inhibitors," *European journal of medicinal chemistry*, vol. 199, p. 112391, 2020.

[157] S. L. Schreiber, "The rise of molecular glues," *Cell*, vol. 184, no. 1, pp. 3–9, 2021.

[158] D. A. Foster and A. Toschi, "Targeting mtor with rapamycin: one dose does not fit all," *Cell Cycle*, vol. 8, no. 7, pp. 1026–1029, 2009.

[159] Q. Fan, O. Aksoy, R. A. Wong, S. Ilkhanizadeh, C. J. Novotny, W. C. Gustafson, A. Y.-Q. Truong, G. Cayanan, E. F. Simonds, D. Haas-Kogan *et al.*, "A kinase inhibitor targeted to mtorc1 drives regression in glioblastoma," *Cancer cell*, vol. 31, no. 3, pp. 424–435, 2017.

[160] C. García-Echeverría, "Allosteric and atp-competitive kinase inhibitors of mtor for cancer treatment," *Bioorganic & medicinal chemistry letters*, vol. 20, no. 15, pp. 4308–4312, 2010.

[161] C. C. Thoreen, S. A. Kang, J. W. Chang, Q. Liu, J. Zhang, Y. Gao, L. J. Reichling, T. Sim, D. M. Sabatini, and N. S. Gray, "An atp-competitive mammalian target of rapamycin inhibitor reveals rapamycin-resistant functions of mtorc1," *Journal of Biological Chemistry*, vol. 284, no. 12, pp. 8023–8032, 2009.

[162] A. Zask, J. C. Verheijen, and D. J. Richard, "Recent advances in the discovery of small-molecule atp competitive mtor inhibitors: a patent review," *Expert opinion on therapeutic patents*, vol. 21, no. 7, pp. 1109–1127, 2011.

[163] C. M. Chresta, B. R. Davies, I. Hickson, T. Harding, S. Cosulich, S. E. Critchlow, J. P. Vincent, R. Ellston, D. Jones, P. Sini *et al.*, "Azd8055 is a potent, selective, and orally bioavailable atp-competitive mammalian target of rapamycin kinase inhibitor with in vitro and in vivo antitumor activity," *Cancer research*, vol. 70, no. 1, pp. 288–298, 2010.

[164] P. A. M. Zapata, C. J. Beese, A. Jünger, G. Dalmasso, N. R. Brady, and A. Hamacher-Brady, "Time course decomposition of cell heterogeneity in tfeb

signaling states reveals homeostatic mechanisms restricting the magnitude and duration of tfeb responses to mtor activity modulation," *BMC cancer*, vol. 16, no. 1, pp. 1–19, 2016.

[165] S. Napolitano, I. Ruolo, G. Perrino, and D. di Bernardo, "Tfeb dynamical model reveals a novel feedback loop biological mechanism," *IFAC-PapersOnLine*, vol. 52, no. 26, pp. 213–218, 2019.

[166] C. Salazar and T. Höfer, "Allosteric regulation of the transcription factor nfat1 by multiple phosphorylation sites: a mathematical analysis," *Journal of molecular biology*, vol. 327, no. 1, pp. 31–45, 2003.

[167] M. di Bernardo, C. Budd, A. R. Champneys, and P. Kowalczyk, *Piecewise-smooth dynamical systems: theory and applications*. Springer Science & Business Media, 2008, vol. 163.

[168] Y. C. Wu, W. K. K. Wu, Y. Li, L. Yu, Z. J. Li, C. C. M. Wong, H. T. Li, J. J. Y. Sung, and C. H. Cho, "Inhibition of macroautophagy by bafilomycin a1 lowers proliferation and induces apoptosis in colon cancer cells," *Biochemical and biophysical research communications*, vol. 382, no. 2, pp. 451–456, 2009.

[169] S. Pestka, "Inhibitors of ribosome functions," *Annual Review of Biochemistry*, vol. 40, no. 1, pp. 697–710, 1971.

[170] E. Wong and A. M. Cuervo, "Integration of clearance mechanisms: the proteasome and autophagy," *Cold Spring Harbor perspectives in biology*, vol. 2, no. 12, p. a006734, 2010.

[171] Y. Wang and W.-D. Le, "Autophagy and ubiquitin-proteasome system," *Autophagy: Biology and Diseases*, pp. 527–550, 2019.

[172] J. Adams, V. J. Palombella, E. A. Sausville, J. Johnson, A. Destree, D. D. Lazarus, J. Maas, C. S. Pien, S. Prakash, and P. J. Elliott, "Proteasome inhibitors:

a novel class of potent and effective antitumor agents," *Cancer research*, vol. 59, no. 11, pp. 2615–2622, 1999.

[173] P. Baumann, S. Mandl-Weber, F. Oduncu, and R. Schmidmaier, "The novel orally bioavailable inhibitor of phosphoinositol-3-kinase and mammalian target of rapamycin, nvp-bez235, inhibits growth and proliferation in multiple myeloma," *Experimental cell research*, vol. 315, no. 3, pp. 485–497, 2009.

[174] L. Ljung, "System identification," in *Signal analysis and prediction*. Springer, 1998, pp. 163–173.

[175] G. Perrino and D. di Bernardo, "Synchronisation of yeast cell cycle through quorum sensing coupling," *IFAC-PapersOnLine*, vol. 53, no. 2, pp. 16 779–16 784, 2020, 21th IFAC World Congress.

[176] G. M. Whitesides, "The origins and the future of microfluidics," *nature*, vol. 442, no. 7101, pp. 368–373, 2006.

[177] K. Kawakami, "Tol2: a versatile gene transfer vector in vertebrates," *Genome biology*, vol. 8, no. 1, pp. 1–10, 2007.